MICROSTRUCTURAL PROPERTIES OF SEMICONDUCTOR NANOSTRUCTURES

FANG LI

LINACRE COLLEGE



A THESIS SUBMITTED

FOR THE DEGREE OF DOCTOR OF PHILOSOPHY

DEPARTMENT OF MATERIALS

UNIVERSITY OF OXFORD

2010

ABSTRACT

Semiconductor nanostructures have attracted great interest owing to their unique physical properties and potential applications in nanoscale functional devices. The enhancement of the physical properties of semiconductor nanostructures and their performance in devices requires a deeper understanding of their fundamental microstructural properties. Thus this thesis is focused on the experimental and theoretical studies of the microstructural properties of two important semiconductor nanostructures: axial heterostructured silicon nanowires with varying doping and indium nitride colloidal nanoparticles.

In this thesis, axial heterostructured silicon nanowires with varying doping were synthesized on an oxide-removed Si{111} substrate using a vapour-liquid-solid approach. Their fundamental microstructural properties, including the crystalline structure, wire growth direction and morphologies, were studied using various characterization techniques. It is found that a very small fraction of the silicon nanowires crystallize in a hexagonal (wurtzite) phase, which is thermodynamically unstable in bulk silicon under ambient conditions, while a large majority of the synthesized silicon nanowires exhibit the expected diamond cubic crystalline structure. About 75% of the diamond cubic silicon nanowires synthesized grow in a single <111> direction, while the rest contain growth-related kinks, where the nanowire switches to another direction during the growth. The ~109° silicon nanowire kinks are the most commonly observed, and the growth direction before and after such ~109° kink are both <111>. The sidewalls of silicon nanowires do not change abruptly at the ~109° kink, but exhibit an elbow-shaped structure. It is also found that the nanowire sidewalls exhibit periodic nanofaceting, which is strongly doping-dependent. The nanofaceting is found to occur during the enhanced sidewall growth that arises when the diborane dopant gas is introduced. A thermodynamic model predicting the dependence of nanofacet period on the wire diameter is developed.

Another semiconductor nanostructure studied in this thesis is indium nitride colloidal nanoparticles, which were grown using a solution-phase chemical method. The formation of such indium nitride colloidal nanoparticles is confirmed by studying their compositions, crystalline structures and shape using various electron microscopy techniques. The size of the indium nitride colloidal nanoparticles was controlled by varying the time of solution-phase reactions. The most probable size of the colloidal nanoparticles increases and the size distribution broadens with the increase of reaction time. The crystalline structures of the indium nitride colloidal nanoparticles are found to be particle size dependent. The observed dependence of the band gap blueshift of the indium nitride colloidal nanoparticles on the reaction time (hence the particle size) is explained by the quantum-size effect.

PREFACE

This thesis is an account of work carried out by the author in the Department of Materials, University of Oxford from October 2007 to June 2010, under the supervision of Professor David J. H. Cockayne FRS, Dr Peter D. Nellist and Dr Christian Lang.

This research project is in part sponsored by an industrial collaborator (the name of the company is kept confidential according to the agreement made between the university and the company). The materials studied in this thesis are provided by the industrial collaborator. No commercially sensitive background intellectual property belonging solely to the company is included in the thesis.

No part of this thesis has ever been submitted for a degree at this or any other university. All of the work is original, and when the work of others is included, it has been clearly referenced and duly acknowledged.

Some of the work described in this thesis has been published in the scientific literature and presented at conferences (see details below). All publications/presentations have been reviewed and permitted by the company before submission for publication or before presentation.

JOURNAL ARTICLES

1. "Dependence of Surface Facet Period on the Diameter of Nanowires"
   Fang Li, Peter D. Nellist, Christian Lang and David J. H. Cockayne, ***ACS Nano***, 4, 632 (2010). (The study is largely described in Chapter 5.)

2. "Imaging and Analysis of Axial Heterostructured Silicon Nanowires"
   Fang Li, Peter D. Nellist, Christian Lang and David J. H. Cockayne, ***Journal of Physics: Conference Series***, 241, 012088 (2010). (The study is largely described in Chapter 4.)

3. "Doping-dependent Nanofaceting on Silicon Nanowire Surfaces"
   Fang Li, Peter D. Nellist and David J. H. Cockayne, ***Applied Physics Letters***, 94, 263111 (2009). (The study is largely described in Chapter 5.)

CONFERENCE TALKS

1. The 4th International Nanowire Growth Workshop 2009 (NWG 2009), October 2009, France.

2. The 2nd Semiconductor Materials, Nanostructures and Devices Workshop (SMND), October 2009, UK.

3. Electron Microscopy and Analysis Group Conference 2009 – Microscopy at the nanoscale and beyond (EMAG 2009), September 2009, UK.

4. The 16th International Conference on Microscopy of Semiconducting Materials (MSM XVI), March 2009, UK.

ACKNOWLEDGEMENTS

I would like to express my heartfelt appreciation and gratitude to my three supervisors, Professor David J. H. Cockayne FRS, Dr Peter D. Nellist and Dr Christian Lang, for their invaluable guidance and full support throughout the entire course of my D.Phil study. A special word of gratitude goes to the industrial collaborators of my research project, for providing the specimens and sharing their expertise and insights in this project.

I would also like to thank all the members in the Oxford Materials Electron Microscopy and Microanalysis group, both past and present, especially Dr John L. Hutchison, Dr Mike L. Jenkins, Dr Crispin J. D. Hetherington, Dr Lisa S. Karlsson, Dr Rebecca J. Nicholls, Mrs Gabriella Chapman and Mr Ron Doole, who have trained me and given me guidance on the topics of electron microscopy. Thanks to Dr Valeria Nicolosi, Dr Peng Wang, Dr Gareth M. Hughes, Dr Chao Lin, Dr Sergio Lozano-Perez, Dr Shao-Ju Shi, Dr Guoqiang Li and Dr Yixin Chen for their generous help and useful advice. I would also like to acknowledge all the laboratory technicians and staff of Department of Materials for their kind assistance and support.

Last but not least, I would like to express my appreciation to University of Oxford for the opportunity to pursue this course and for the research scholarship provided.

LIST OF ABBREVIATIONS

0D	Zero-dimensional
1D	One-dimensional
2D	Two-dimensional
3D	Three-dimensional
ADF	Annular Dark-field
B_2H_6	Diborane
bcc	Body-centred Cubic
BF	Bright-field
CCD	Charge-coupled Device
CMOS	Complementary Metal-Oxide-Semiconductor
CRT	Cathode Ray Tube
CTF	Contrast Transfer Function
CVD	Chemical Vapour Deposition
DC	Direct Current
DF	Dark-field
EDP	Electron Diffraction Pattern
EDX	Energy Dispersive X-ray
EM	Electron Microscopy/Microscope
fcc	Face-centred Cubic
FEG	Field Emission Gun
FET	Field Effect Transistor
FFT	Fast Fourier Transform
FWHM	Full Width Half Maximum

HAADF	High-Angle Annular Dark-field
HRSEM	High Resolution Scanning Electron Microscopy/Microscope
HRTEM	High Resolution Transmission Electron Microscopy/Microscope
InN	Indium Nitride
LED	Light-emitting Diode
LPCVD	Low Pressure Chemical Vapour Deposition
MBE	Molecular Beam Epitaxy
MOCVD	Metalorganic Chemical Vapour Deposition
MOVPE	Metalorganic Vapour Phase Epitaxy
NW	Nanowire
PH_3	Phosphine
PL	Photoluminescence
POA	Phase Object Approximation
RF	Radio Frequency
SAED	Selected Area Electron Diffraction
SCCM	Standard Cubic Centimetres per Minute
SEM	Scanning Electron Microscopy/Microscope
SiH_4	Silane
SiNW	Silicon Nanowire
SiO_2	Silicon Dioxide
STEM	Scanning Transmission Electron Microscopy/Microscope
TA	Transverse Acoustical
TEM	Transmission Electron Microscopy/Microscope
TMB	Trimethylboron
TO	Transverse Optical

UHV	Ultra High Vacuum
VLS	Vapour-Liquid-Solid
WPOA	Weak Phase Object Approximation

LIST OF FIGURES

Figure 2.1 Schematic showing the diamond cubic Si crystal structure. ··· **7**

Figure 2.2 Schematic showing (a) the vertical nanowire FET: the gate is a complete, uniform wrap-around gate (redrawn from Reference 8); and (b) the SiNW-based detection of single virus (redrawn from Reference 19). ····· **9**

Figure 2.3 Schematic illustration showing the growth of a nanowire via the VLS mechanism (redrawn from Reference 43). ····· **11**

Figure 2.4 Different models describing the incorporation routes of source atoms into the growth interface of nanowire: (a) the classical VLS mechanism; (b) diffusion through the liquid droplet surface; and (c) diffusion through the nanowire sidewalls (redrawn from Reference 55). ····· **15**

Figure 2.5 (a) Schematic of the Au/Si-eutectic droplet on a flat surface; and (b) schematic of the initial stage of nanowire growth (redrawn from Reference 56). ····· **16**

Figure 2.6 Schematic showing the nanowire heterostructure synthesis: (a) the preferential reactant incorporation at the catalyst (growth end) leads to the 1D axial growth; (b) a change in the reactant leads to either (c) the axial heterostructure growth or (d) the radial heterostructure growth, depending on whether the reactant is preferentially incorporated (c) at the catalyst or (d) uniformly on the wire surface (redrawn from Reference 60). ····· **19**

Figure 2.7 Schematic diagram showing the formation of a diffuse interface during the VLS growth of axial heterostructured nanowires (redrawn from Reference 55). ····· **21**

Figure 2.8 Experimental examples showing the effects of boron doping on the microstructures of SiNWs: SEM images of (a) the undoped SiNWs; and (b) the cone-shaped B_2H_6-doped SiNWs from the Au-catalysed VLS process (from Reference 70); (c) STEM images showing the undoped-B doped transitional area in SiNWs (from Reference 71); HRTEM images of (d) the TMB-doped SiNW; and (e) the B_2H_6-doped SiNW (from Reference 72). ····· **23**

Figure 2.9 Schematic showing the structure of the axially doped SiNWs with varying *n*- and *p*-doping. ····· **25**

Figure 3.1 Schematics of a typical TEM consisting of five systems: illumination, specimen stage, imaging, magnification and data recording systems. ····· **35**

Figure 3.2 The two basic operations of the TEM imaging system involve (a) the diffraction mode; and (b) the image mode. The intermediate lens selects either (a) the back focal plane or (b) the image plane of the objective lens as its object (redrawn from Reference 107). ····· **36**

Figure 3.3 The Ewald sphere construction. ····· **39**

Figure 3.4 The spacing *R* between the direct beam and a scattering maximum (such as a diffracted beam or the radius of a ring of diffracted intensity) is related to the camera length *L* (redrawn from Reference 107). ····· **41**

Figure 3.5 Comparison of the use of an objective aperture in TEM to select (a) the direct or (b) the scattered electron to form (a) BF and (b) DF images, respectively (redrawn from Reference 107). ····· **42**

Figure 3.6 Schematic diagram of the image formation of HRTEM (redrawn from Reference 111). ····· **45**

Figure 3.7 Schematic showing (a) a $\frac{\pi}{2}$ phase shift in a small-amplitude scattered wave, the resultant wave has only a slight phase change but no amplitude change; an additional phase shift brings the scattered wave either exactly (b) into or (c) out of the phase with the primary wave. ····· **47**

Figure 3.8 The function $\sin \chi(u)$ for a weak phase object for a JEOL JEM-4000EX HRTEM (400 kV and C_S = 0.9 mm) for a Scherzer defocus of -44 nm. ····· **49**

Figure 3.9 Schematic showing the STEM image formation (redrawn from Reference 107). ····· **53**

Figure 3.10 Schematic drawing of the electron column, deflection system, and electron detectors in a typical SEM (redrawn from Reference 120). ····· **59**

Figure 3.11 Energy-level diagrams of Rayleigh scattering, Stokes Raman scattering, and anti-Stokes Raman scattering. The line thickness is roughly proportional to the signal strength from the different transitions. ····· **61**

Figure 4.1 Comparison of the stacking of the tetrahedral in (a) the diamond cubic (<110> projected) and (b) the hexagonal ($<0\bar{1}10>$ projected) structures. ····· **65**

Figure 4.2 HRTEM of a VLS-grown axial heterostructured SiNW, insets: the Fourier transform of the image and the TEM image of the same SiNW taken at low magnification. ····· **68**

Figure 4.3 (a) TEM image of a SiNW, numbers 'I' and 'II' are assigned to label different positions; (b) HRTEM image of part I in (a); and (c) HRTEM image of part II in (a). Insets in (b) and (c) are their corresponding Fourier transforms. ····· **70**

Figure 4.4 (a) Diffraction rings from the Au film as a reference; (b) EDPs of a diamond cubic SiNW with the reference of Au{111} schematically highlighted; and (c) EDPs of the same SiNW in Figure 4.3 with the reference of Au{111} schematically highlighted. ····· **72**

Figure 4.5 Indexed SAED patterns for the same SiNW in Figure 4.3(a) for the (a) $[0\bar{1}1\bar{1}]$ and (b) $[\bar{1}2\bar{1}3]$ beam direction. ····· **73**

Figure 4.6 (a) TEM image of a ~150° kinked SiNW, numbers 'I~III' are assigned to label different positions; HRTEM image of (b) part I, (c) part II and (d) part III in (a), insets in (b)~(d) are their corresponding Fourier transforms. ····· **74**

Figure 4.7 Indexed SAED patterns for the same kinked SiNW in Figure 4.6 for the (a) $[\bar{2}4\bar{2}3]$ and (b) $[\bar{1}2\bar{1}3]$ beam direction. ····· **76**

Figure 4.8 Stokes Raman spectra of the hexagonal (Si IV) nanowires, bulk Si and diamond cubic (Si I) nanowires under the same low laser power. ····· **78**

Figure 4.9 Schematic diagram showing a single twin in (a) being intersected by a second twin in (b). Strain accommodation causes the region of intersection to transform to the hexagonal stacking. Matrix labelled M, twins labelled 1 and 2, hexagonal phase labelled H (from Reference 137). ····· **80**

Figure 4.10 Schematic showing the elements in the Schmidt's model (redrawn from Reference 148). ····· **83**

Figure 4.11 Shadow imaging technique for determining the nanowire growth direction: (a) optical diagram for shadow imaging (from Reference 156); (b) SAED patterns of a straight SiNW; (c) the corresponding shadow image of the same straight SiNW recorded in the diffraction mode; (d) TEM image of a ~109° kink in a VLS-grown SiNW, viewed along the <110> direction; (e) SAED patterns of the same kink in (d); and (f) the corresponding shadow image of the same kink in (d) recorded in the diffraction mode. ····· **87**

Figure 4.12 (a) TEM image of a ~109° kink in a VLS-grown SiNW, taken along the <110> direction, numbers 'I~IV' are assigned to label different positions; HRTEM image of (b) part I, (c) part II, (d) part III and (e) part IV in (a); insets in (b)~(d): the corresponding Fourier transforms; insets in (e): image taken at low magnification and the corresponding Fourier transform. ····· **89**

Figure 4.13 Schematic of the short facets at the ~109° kinked SiNW in Figure 4.12(a), viewed along the <110> direction. ····· **91**

Figure 4.14 (a) SEM image of a ~109° SiNW kink (image taken by Dr Gareth Hughes); and (b) a possible 3D sketch visualizing the crystallographic relationship of the ~109° SiNW kink. ····· **92**

Figure 4.15 The <110> projected atomistic representation of the kink formation mechanisms for resulting in the elbow-shaped kink structure in a ~109° kinked diamond cubic SiNW. ····· **94**

Figure 5.1 Experimental examples of (a) SEM image of the periodic instabilities for Si whiskers (from Reference 158); (b) SEM image showing the microscale faceting on the lateral surface of Si whisker (from Reference 159); (c) SEM image showing the very rough and undulating SiNW sidewalls (from Reference 160); and (d) defocused TEM image of a SiNW showing the sawtooth-like faceting on the nanowire sidewalls. The facet angles are indicated; *p* and *h* denote the sawtooth period and amplitude (from Reference 161). ····· **98**

Figure 5.2 Schematic showing the elements of the model proposed by Ross *et al*. (from Reference 161). ····· **100**

Figure 5.3 (a) Image of a ~22 μm long axial heterostructured *p*-*n*-*i* SiNW reconstructed from TEM images taken of adjacent areas along the wire growth direction. TEM image of the SiNW in (a) taken at (b) the *p*-type (B-doped) SiNW region; (c) the *n*-type (P-doped) SiNW region; and (d) the intrinsic SiNW region. ····· **103**

Figure 5.4 (a) TEM image of the sidewall nanofacets in the *p*-type (B-doped) region of an axial heterostructured *p*-*n*-*i* SiNW, viewed along the <110> direction, inset: image taken at low magnification and facet angles are indicated; and (b) HRTEM image of the facets, inset in (b): Fourier transform of the image. ····· **106**

Figure 5.5 HRSEM image of the sidewall nanofacets in the *p*-type (B-doped) region of an axial heterostructured *p*-*n*-*i* SiNW (image taken by Dr Gareth Hughes). ····· **107**

Figure 5.6 (a) Schematic of the 3D structure of the previously reported intrinsic SiNW with sidewall nanofaceting (from Reference 161); (b) schematic of the 3D structure of the axial heterostructured *p*-*n*-*i* SiNW with sidewall nanofaceting in the *p*-type (B-doped) region observed in this work; and (c) schematic of the 2D structure of the wire in (b) viewed along the $[\bar{1}10]$ direction. ····· **109**

Figure 5.7 3D atomic model of the nanowire with faceting on sidewalls. Such faceting results from the periodic alternation of twin segments (from Reference 171). ····· **110**

Figure 5.8 (a) HAADF-STEM image of single Au atoms (marked by arrows) in the near-catalyst region of an axial heterostructured *p-n-i* SiNW, as a reference for the contrast between Au and Si; (b) intensity profiles across several Si lattices through two bright spots associated with impurities 1 [along the aa' direction in (a)] and 2 [along the bb' direction in (a)]; and (c) HAADF image of the faceted *p*-type (B-doped) SiNW region in the same *p-n-i* SiNW, viewed along the <110> direction, inset: Fourier transform of the image (the HAADF-STEM images were taken by Dr Peng Wang). · **113**

Figure 5.9 (a) TEM image showing the initially-grown intrinsic region of a ~24 μm long axial heterostructured *i-p-n-i* SiNW, viewed along the <110> direction; and (b) HRSEM image of the initially-grown intrinsic region of a ~24 μm long axial heterostructured *i-p-n-i* SiNW (the HRSEM image was taken by Dr Gareth Hughes). ····· **116**

Figure 5.10 (a) Schematic showing the two growth interfaces during a VLS nanowire growth; and (b) schematic showing the side view of the ideal Si{112} surface. ····· **118**

Figure 5.11 (a) Schematic of the regular hexagonal wire cross section; and (b) schematic of the faceted nanowire viewed along the $[\bar{1}10]$ direction. ····· **120**

Figure 5.12 TEM images of <111>-oriented axial heterostructured *p-n-i* SiNWs in the faceted *p*-type (B-doped) region with wire diameters of (a) ~150 nm; (b) ~60 nm; (c) ~50 nm; (d) ~175 nm; and (e) plot of average facet period versus wire diameter. TEM images in (a)~(d) are all viewed along the <110> zone axis. ····· **122**

Figure 5.13 Schematic of the 3D structure of a <111>-oriented axial heterostructured *p-n-i* SiNW with sidewall nanofaceting in the *p*-type (B-doped) region. The edges, apexes and sidewall boundaries in the model are indicated. ····· **126**

Figure 5.14 Schematic of the 2D periodic nanofaceting occurred on a SiNW sidewall surface. Effective elastic forces due to surface stress tensor discontinuity appear at edges. ····· **127**

Figure 5.15 The dependence of average facet period on the wire diameter of the <111>-oriented axial heterostructured *p-n-i* SiNWs in the faceted *p*-type (B-doped) region. The solid line through the data points is the nonlinear least-square fit to Equation 5.9. ····· **128**

Figure 6.1 Photoluminescence spectra of the InN colloidal nanoparticles grown for 10, 20 and 30 minutes in solution, respectively (data from industrial collaborators). ····· **138**

Figure 6.2 (a) STEM image showing the InN colloidal nanoparticles with different sizes; and (b) EDX spectra obtained from the large-size nanoparticle, small-size nanoparticle agglomerates and carbon support film. ····· **142**

Figure 6.3 (a) HRTEM image of a ~4 nm InN colloidal nanoparticle; (b) Fourier transform of the localized image of the nanoparticle region marked by a red square in (a); (c) HRTEM image of a ~5 nm InN colloidal nanoparticle; and (d) Fourier transform of the image in (c). ····· **145**

Figure 6.4 HRTEM images of (a) a ~5 nm and (b) a ~7 nm InN colloidal nanoparticles, insets in (a) and (b) are the corresponding Fourier transforms of the particle images (marked by red squares); (c) HRTEM image of a ~16 nm InN colloidal nanoparticle; and (d) the Fourier transform of the image in (c). ····· **148**

Figure 6.5 (a) HRTEM image showing the defects in an InN nanoparticle, numbers 'I' and 'II' are assigned to different regions of the nanoparticle; (b) image of the same nanoparticle in (a) taken at low magnification; (c) and (d) are the corresponding Fourier transforms of the localized images of the regions I and II [marked by red squares in (a)], respectively. ····· **150**

Figure 6.6 (a) TEM image of the InN colloidal nanoparticles deposited on the holey carbon support film; and (b) schematic of the possible shapes in 3D. ····· **151**

Figure 6.7 (a) HAADF-STEM image showing an InN colloidal nanoparticle; (b) HAADF-STEM intensity profiles across two dashed lines aa' and bb' in (a) over the nanoparticle; and (c) the same image as in (a) in pseudo 3D graphics. ····· **153**

Figure 6.8 TEM images of the InN colloidal nanoparticles grown for (a) 10 minutes; (b) 20 minutes; and (c) 30 minutes in solution. Inset in (c): TEM image of an InN colloidal nanoparticle with a size larger than 50 nm observed in the specimen grown for 30 minutes. ····· **157**

Figure 6.9 Size histograms of the InN colloidal nanoparticles grown for (a) 10, (b) 20 and (c) 30 minutes in solution, respectively. Each histogram is fitted with a model of two Gaussian functions superposed together. Insets in (a)~(c): the corresponding histograms in the small nanoparticle size (< 6 nm) region. ····· **159**

Figure 6.10 Calculated (using Equation 6.4) band gap energy upshift, ΔE, as a function of InN nanoparticle diameter d using the value of the heavy hole mass of InN. The solid line is the nonlinear least squares fitting to Equation 6.9. ····· **168**

Figure 6.11 Comparison of the theoretically-predicted PL line shapes (dashed lines) with the corresponding experimental PL spectra (solid lines), for the InN colloidal nanoparticles grown for 10, 20 and 30 minutes in solution. ····· **171**

CONTENTS

ABSTRACT ..... **I**

PREFACE ..... **II**

ACKNOWLEDGEMENTS ..... **IV**

LIST OF ABBREVIATIONS ..... **V**

LIST OF FIGURES ..... **VIII**

CONTENTS ..... **XVI**

CHAPTER 1
INTRODUCTION **1**
1.1 Introduction **1**
1.2 Overview **3**

CHAPTER 2
RESEARCH BACKGROUND AND OBJECTIVES **6**
2.1 Introduction **6**
2.2 One-dimensional Silicon Nanowires **7**
2.2.1 General Introduction 7
2.2.2 Silicon Nanowire Growth 9
2.2.3 Silicon Nanowire Heterostructures 17
2.2.4 Doping of Silicon Nanowires 21
2.2.5 Growth of Axially Doped Silicon Nanowire Heterostructures 24
2.3 Zero-dimensional Indium Nitride Colloidal Nanoparticles **25**
2.3.1 General Introduction 25
2.3.2 Growth of Indium Nitride Colloidal Nanoparticles 26
2.4 Research Objectives **29**
2.5 Chapter Summary **32**

CHAPTER 3
CHARACTERIZATION METHODS 33
3.1 Introduction 33
3.2 Transmission Electron Microscopy 34
3.2.1 Introduction 34
3.2.2 Electron Diffraction 37
3.2.3 Imaging 41
3.3 High Resolution Transmission Electron Microscopy 42
3.3.1 Phase Contrast 43
3.3.2 Weak Phase Object Approximation 46
3.4 Scanning Transmission Electron Microscopy 51
3.5 Energy Dispersive X-ray Spectroscopy 54
3.5.1 Qualitative Analysis 55
3.5.2 Quantitative Analysis 56
3.6 Scanning Electron Microscopy 58
3.7 Raman Spectroscopy 60
3.8 Chapter Summary 62

CHAPTER 4
CRYSTALLINE STRUCTURE AND GROWTH DIRECTION OF SILICON NANOWIRES 63
4.1 Introduction 63
4.2 Crystalline Structure 64
4.2.1 Background of Research 64
4.2.2 Results and Discussion 67
4.3 Growth Direction 81
4.3.1 Background of Research 81
4.3.2 Results and Discussion 85
4.3.2.1 Determination of the Nanowire Growth Direction 85
4.3.2.2 Elbow-shaped Kink Structure 90
4.4 Chapter Summary 94

CHAPTER 5
DOPING-DEPENDENT NANOFACETING ON SILICON NANOWIRE SIDEWALLS 96
5.1 Introduction 96
5.2 Observation of the Doping-dependent Nanofaceting 101
5.3 The Cause of the Doping-dependent Nanofaceting 109
5.3.1 Discussion on the Previously Suggested Mechanisms 109
5.3.2 Impurity-induced Faceting Mechanism 117
5.4 Nanofaceting Model of 1D Nanowires 119
5.5 Chapter Summary 131

CHAPTER 6
INDIUM NITRIDE COLLOIDAL NANOPARTICLES 133
6.1 Introduction 133
6.1.1 Crystalline Structures 134
6.1.2 Chemical Compositions 135
6.1.3 Optical Properties 136
6.2 Results and Discussion 139
6.2.1 Confirmation of the Formation of Indium Nitride Colloidal Nanoparticles 139
6.2.1.1 Compositions 140
6.2.1.2 Crystalline Structures 143
6.2.1.3 Shape 150
6.2.2 Size-dependent Optical Properties 154
6.2.2.1 Particle Size and Size Distribution 154
6.2.2.2 Possible Growth Mechanisms 160
6.2.2.3 Optical Properties 162
6.3 Chapter Summary 172

CHAPTER 7
OVERALL CONCLUSIONS AND FUTURE WORK 173
7.1 Introduction 173
7.2 Axially Doped Silicon Nanowire Heterostructures 174
7.2.1 Conclusions 174
7.2.2 Future Work 176
7.3 Indium Nitride Colloidal Nanoparticles 179
7.3.1 Conclusions 179
7.3.2 Future Work 181
7.4 Chapter Summary 184

REFERENCES 185

Chapter 1

Introduction

1.1 Introduction

Driven by the inevitable size-reduction of microelectronics, the development of semiconductor technology is quickly being driven towards the nanoscale dimensions,[1] where "smaller" has meant a greater performance, *e.g.*, higher density of integration, faster response and less power consumption.[2] Nanoscale structures represent an exciting, intellectually challenging and rapidly expanding area of research that crosses the borders between many areas of the physical science and engineering.[3]

Nanostructures are defined as having at least one dimension $\leq$ 100 nm. Based on their dimensionalities, nanostructures can be divided into zero-dimensional (0D), one-dimensional (1D), two-dimensional (2D) and three-dimensional (3D) systems.[4]

Among them, 1D and 0D nanostructures of semiconducting materials have attracted great interest due to their novel physical properties dependent on dimensionality and size-reduction, as well as their potential applications as the building blocks for nanoscale functional devices.[5,6]

Over the last few years, research has been carried out to explore the fascinating properties of various 1D and 0D semiconductor nanostructures and their potential applications. The "bottom-up" approach has become a powerful alternative to the conventional "top-down" methods in synthesizing various semiconductor nanostructures.[7] Despite the significant progress in these research areas, a number of problems, such as precisely-controlled synthesis, doping, integration and interfacing problems, still need to be resolved before semiconductor nanostructures can be integrated in technologically reliable devices. For example, the microstructural properties of semiconductor nanostructures have to be investigated and understood before the device optimization, because the physical properties of semiconductors and the ultimate device performance depend strongly on their microstructures.[8] Therefore, to desirably tune the physical properties of semiconductor nanostructures through growth manipulation, it is important to understand their fundamental microstructural properties and the growth mechanisms for the formation of microstructures.

This thesis is focused on the experimental and theoretical studies of the microstructural properties of some important 1D and 0D semiconductor

nanostructures. As one of the most powerful tools in nanotechnology, the electron microscope has played an important role in revealing the microstructures of nanomaterials. Thus in this thesis, the microstructural properties of semiconductor nanostructures, such as the morphology, crystalline structures and compositions, were characterized using various electron microscopy (EM) techniques. To have a deeper understanding of the nanostructure growth mechanisms and the structure-property relationships, theoretical models were developed based on experimental evidence.

1.2 Overview

This thesis consists of seven chapters:

(i) The first chapter gives a brief introduction to the background of research and outlines the structure of the thesis.

(ii) The second chapter reviews the recent research and development associated with two important semiconductor nanostructures studied in this thesis, 1D axial heterostructured silicon nanowires (SiNWs) with varying doping and 0D indium nitride (InN) colloidal nanoparticles, with the emphases on the nanostructure growth and growth mechanisms. Experimental details for the syntheses of these two semiconductor nanostructures are also described. Here 1D axial heterostructured SiNWs with varying doping were synthesized using a vapour-liquid-solid (VLS) approach, and 0D InN colloidal nanoparticles were prepared using a

solution-phase chemical method. Existing scientific challenges in these research areas are discussed and the research objectives of this thesis are proposed.

(iii) Chapter 3 introduces the working principles and instrument setups of the characterization techniques used in this thesis to study the microstructural properties of semiconductor nanostructures, including transmission electron microscopy (TEM), high resolution transmission electron microscopy (HRTEM), scanning transmission electron microscopy (STEM), energy dispersive X-ray spectroscopy (EDX), scanning electron microscopy (SEM) and Raman spectroscopy.

(iv) Chapter 4 presents the experimental results on the two fundamental microstructural properties of the axial heterostructured SiNWs, the crystalline structure and the wire growth direction. Methods for the determination of these microstructural properties are discussed. Experimental evidence show that the crystalline structure of SiNWs can be quite different from that of bulk Si, and the nanowire exhibits an elbow-shaped structure at the nanowire kink, where the initial wire growth direction changes. Possible growth mechanisms for resulting in such microstructural properties are discussed.

(v) Chapter 5 focuses on the study of the surface properties of the synthesized axial heterostructured SiNWs with varying doping. In this thesis, doping-dependent surface nanofaceting is observed on the sidewalls of the axial

heterostructured SiNWs. A thermodynamic model of periodic surface nanofaceting is developed for a nanowire structure. The dependence of the nanofacet period on the nanowire diameter is predicted from the model and tested with experiments.

(vi) In Chapter 6, we move to the InN colloidal nanoparticles which were grown from solution-phase reactions. The formation of such InN colloidal nanoparticles is checked by examining their compositions, shape and crystalline structures. The fundamental microstructural and optical properties of the InN colloidal nanoparticles depend strongly on the particle size. Possible colloidal nanoparticle growth mechanisms are proposed to explain the observed size-dependent phenomena. Theoretical analyses on the effects of particle size distribution on the photoluminescence (PL) spectra are also discussed.

(vii) The overall conclusions of the thesis are presented in Chapter 7, and some possible future work is also proposed.

Chapter 2

Research Background and Objectives

2.1 Introduction

Semiconductor nanostructures represent an exciting yet challenging area of research. In the last few decades, a significant amount of research has been carried out on various semiconductor nanostructures. This thesis discusses the microstructural properties of two important semiconductor nanostructures: 1D axial heterostructured silicon nanowires (SiNWs) with varying doping and 0D indium nitride (InN) colloidal nanoparticles. To propose the research objectives of this thesis, it is necessary to summarize the recent progress and to identify the outstanding challenges associated with these two semiconductor nanostructures. Thus the purpose of this chapter is to present the general background of research and to formulate the research aims of this thesis [literature directly relating to the experimental results is reviewed in the relevant chapters (Chapters 4~6)].

2.2 One-dimensional Silicon Nanowires

2.2.1 General Introduction

Si is the principal component and the most widely used material of semiconductor devices, integrated circuits or microchips in today's microelectronic industry. It is a group IV element in the periodic table and the Si crystal under ambient conditions has a diamond cubic structure with a lattice constant of 5.43 Å. It consists of two face-centred cubic (fcc) lattices, one of which is displaced by one fourth in the body diagonal direction. Each Si atom is tetrahedrally bonded to the four nearest neighbours (see Figure 2.1).[9] Bulk single-crystalline Si is an indirect band gap semiconductor with an energy gap of 1.12 eV (at 300 K). Importantly, Si can be doped with other elements to tune its conductivity. Such control is necessary for transistors, solar cells, integrated circuits and other semiconductor devices.[10]

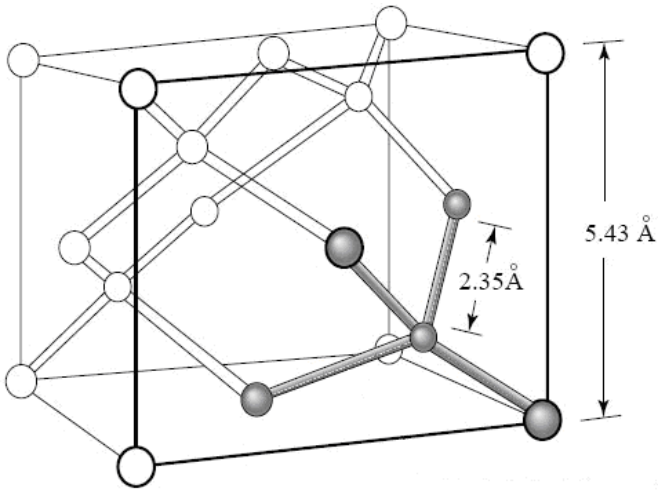


Figure 2.1 Schematic showing the diamond cubic Si crystal structure.

In particular, silicon nanostructures (*e.g.*, 1D SiNWs) are expected to exhibit different physical properties compared to bulk Si, as certain physical phenomena may only be manifested at a nanoscale. Therefore, they have received considerable attention in the last few decades.[11] For example, 1D SiNWs and their heterostructures have been reported to exhibit novel electrical, optical, mechanical and thermal properties.[12,13,14,15,16] Thus they are promising candidate materials for the building blocks of nanoscale electronic and photonic devices and sensors, such as field effect transistors (FETs),[12] logic gates,[13] decoders,[14] chemical/biological detectors,[15] and nanoelectromechanical systems.[16] Figure 2.2(a) and (b) schematically show two examples of nanowire (NW)-based devices. The operating principles and performance of these devices are controlled by the functional interfaces and/or heterostructures within the devices,[17] and are strongly influenced by the microstructural properties of SiNWs, such as the dimensions, morphology, phase purity and chemical compositions. Therefore, precise control over nanowire microstructures through the syntheses of 1D SiNWs and heterostructures is required for the successful fabrication of high-performance devices.[18] Understanding the growth mechanisms of SiNWs offers important information for the growth optimization. In addition, complementary doping within a single nanowire versus assembly of two distinctly doped nanowires represents an alternative strategy for preparing nanoscale devices, and moreover, might lead to better defined junctions. Therefore, axial heterostructured SiNWs with varying doping were chosen to study in this thesis. Here, recent progress in SiNW growth and heterostructure formation is reviewed, and the technical issues relevant to

the SiNW growth and doping are discussed.

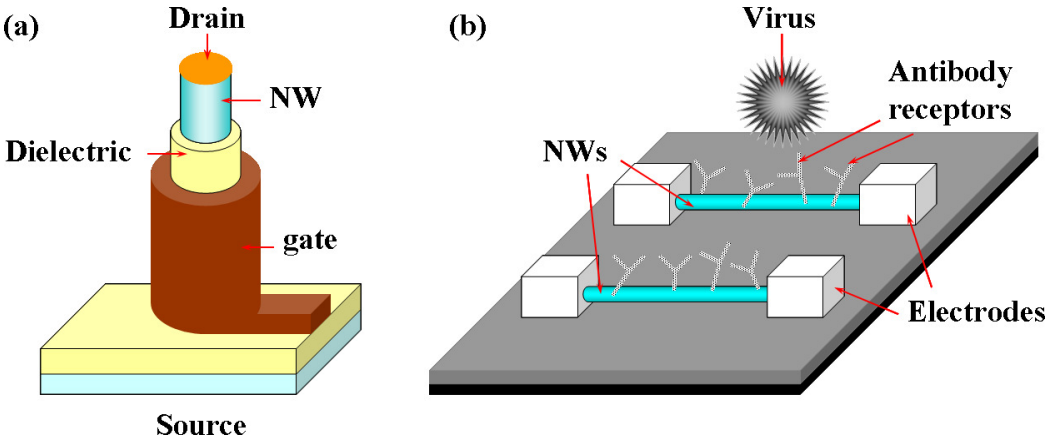


Figure 2.2 Schematic showing (a) the vertical nanowire FET: the gate is a complete, uniform wrap-around gate (redrawn from Reference 8); and (b) the SiNW-based detection of single virus (redrawn from Reference 19).

2.2.2 Silicon Nanowire Growth

SiNWs can be synthesized using many techniques, including thermal evaporation,[20,21] laser ablation,[22] electron-beam evaporation,[23] a carbon-assisted method,[24] oxide-assisted growth,[25,26,27] a scanning tunnelling microscopy-assisted method,[28] and a template-directed method.[29] However, the most extensively used method to grow SiNWs is a process described as the vapour-liquid-solid (VLS) growth mechanism. It has been demonstrated to be the most successful approach for generating various single-crystalline semiconductor nanowires in relatively large quantities.[30,31,32,33] A chemical vapour deposition (CVD) system is usually used in the VLS growth of SiNWs. In a typical CVD process, SiNWs are synthesized using a metal catalyst (usually gold) to dissolve gaseous reactants [*e.g.*, silane (SiH_4) as the Si source] at

elevated temperatures, followed by the nucleation and growth of single-crystalline nanowires. CVD has the advantage that the catalyst can be deposited in the same chamber as the Si, minimizing the contamination of the catalyst and the substrate by the intermediate air exposure.[34] In particular, low pressure CVD (LPCVD), where the growth is carried out at subatmospheric pressures, enables the reduction of unwanted gas-phase reactions, resulting in an improvement of the uniformity.[35]

Although the VLS process is the most versatile method for generating single-crystalline SiNWs with controllable sizes and compositions in terms of feasibility, it also has some drawbacks. For example, the selection of an appropriate catalyst is one of the challenges, and the necessary use of metal catalyst may also contaminate semiconductor nanowires.[36] Today, gold is the most common metal catalyst used for the VLS growth of SiNWs;[37] however, due to the cross-contamination issues, the utilization of gold is incompatible with the conventional complementary metal-oxide-semiconductor (CMOS) technology. This is because gold creates deep trap levels in the Si band gap and thus causes undesirable changes to the electrical properties of Si.[38] However, to date the role of gold in the VLS nanowire growth has not been replaced and the search for alternative metal catalysts is still underway. Although some metals exhibit the potential to catalyse the VLS growth,[39,40] they suffer from the problems such as instability and degradation of nanowire quality.[41]

The VLS growth mechanism for forming semiconductor nanowires is as follows:

metal nanoclusters (such as gold) are heated above the eutectic temperature for the metal-semiconductor system of choice in the presence of a vapour-phase source of the semiconductor, *e.g.*, SiH_4 in the case of Si. Adsorption of the vapour-phase reactant on the metal catalyst leads to the formation of a liquid metal-semiconductor alloy. Continued adsorption of the vapour-phase semiconductor results in the supersaturation of the liquid alloy, leading to the nucleation of solid semiconductor. The liquid/solid interface thus formed is the growth interface, as the semiconductor in solution condenses here to form the solid nanowire. Continuous vapour delivery provides the driving force for the diffusion of semiconductor from the liquid-catalyst particle surface to the growth interface.[42] All major steps involved in a VLS process are schematically illustrated in Figure 2.3.

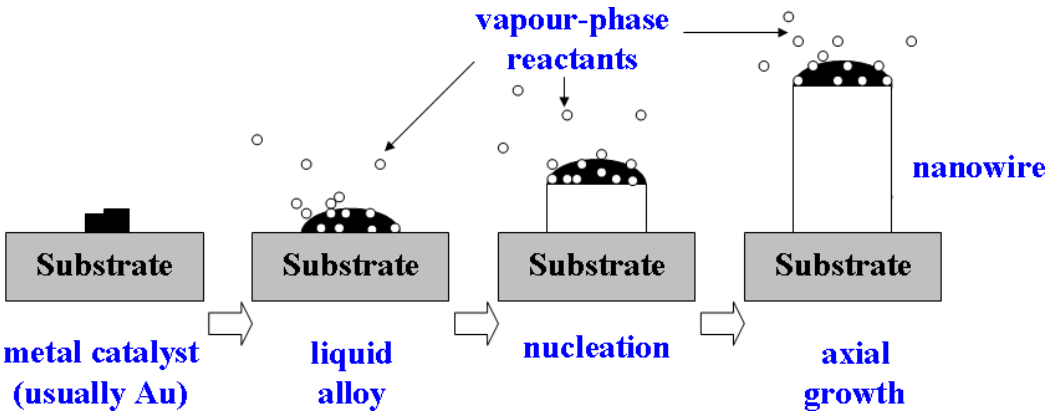


Figure 2.3 Schematic illustration showing the growth of a nanowire via the VLS mechanism (redrawn from Reference 43).

The VLS growth mechanism was first proposed by Wagner and Ellis[44] to explain the growth of Si whiskers. Although it was developed based on the growth of Si whiskers with micrometer-size diameters, it is generally applicable to the syntheses of SiNWs

and many other nanowires. The two main points are

(i) The liquid droplet surface is an ideal rough surface with a much larger sticking coefficient than that of solid crystal surfaces, whereby it captures all the impinging Si source atoms and the whiskers grow only at the areas seeded by the Au-Si particles. The diameter of whiskers is mainly determined by the droplet size and the final length can be adjusted by the duration of vapour source supply.

(ii) The growth rate of Si whiskers depends on the diameter, where thin whiskers grow slower than thick ones due to the Gibbs-Thomson effect.[45] According to the Gibbs-Thomson effect, the decrease of supersaturation as a function of whisker diameter d is given as

$$\frac{\Delta\mu}{k_B T} = \frac{\Delta\mu_0}{k_B T} - \frac{4\Omega\alpha_{VS}}{k_B T d} \tag{2.1}$$

where k_B is the Boltzmann's constant, T is the absolute temperature, $\Delta\mu$ is the effective difference between the chemical potential of Si in the vapour phase and in the whisker, $\Delta\mu_0$ is the chemical potential difference for the plane boundary case ($d \to \infty$), α_{VS} is the specific free energy of the wire surface, Ω is the atomic volume of Si. The dependence of growth rate V on supersaturation can be written as

$$V = b\left(\frac{\Delta\mu}{k_B T}\right)^n \tag{2.2}$$

where b is a coefficient which is independent of the supersaturation. Combining Equations 2.1 and 2.2, one obtains

$$V = \frac{dL}{dt} = b(\frac{\Delta\mu_0}{k_B T} - \frac{4\Omega\alpha_{VS}}{dk_B T})^n \quad (2.3)$$

There exists a critical diameter d_C, under which the whiskers stop growing ($V = 0$).

$$d_C = \frac{4\Omega\alpha_{VS}}{\Delta\mu_0} \quad (2.4)$$

However, one should note that such a mechanism does not present a complete explanation of the VLS growth, because the droplet size may not be the same as that of the nanowires, and the binary alloy nature of the droplet cannot be neglected.[46] Some experimental results contradicting the classical VLS mechanism have been reported. For example, the growth behaviour of ultra-thin nanowires deviates from the predictions made by the classical VLS mechanism.[47] Also, the metal catalyst does not necessarily need to be in a liquid form during growth, in contrast to the common understanding of the classical VLS mechanism, where the growth temperature should be higher than the eutectic point of the metal-semiconductor alloy in order to form the liquid droplet. It has been demonstrated that the growth of SiNWs at a temperature below the eutectic temperature is also possible, due to the surface melting effect of nanoparticles or the interface melting effect.[48]

Therefore, different VLS-based theories have been developed to explain the deviation of growth behaviour from the classical VLS mechanism:

(i) Surface diffusion model:

Wang *et al.*[49] have shown that in some cases the whisker growth may be

controlled by surface diffusion. They suggested that the diffusion along the liquid alloy droplet surface [Figure 2.4(b)], driven by both a concentration gradient and surface energy decrease, should not be ignored. The surface diffusion provides a favourable mass transport path for whisker growth and becomes more important with decreasing whisker diameter, decreasing solubility of growth species in the liquid phase, and increasing ratio of the surface diffusion coefficient to the bulk liquid diffusion coefficient.

In this diffusion-induced VLS model,[49] the ratio of mass transport rates of surface and bulk liquid diffusion is

$$\frac{q_S}{q_B} = \frac{4D_S\nabla_S}{dD_B\nabla_B} \tag{2.5}$$

where q_S, D_S and ∇_S are the mass transport rate of surface diffusion, the surface diffusion coefficient and the surface concentration gradient, respectively, while q_B, D_B and ∇_B are the corresponding parameters describing the bulk liquid diffusion. Therefore, for ultra-thin SiNWs, surface diffusion becomes significant, especially when the growth temperature is low and the metal catalyst becomes solid (or partially solid).[50] A solid metal catalyst can also lead to the growth of ultra-thin nanowires through surface diffusion.[51,52] In addition to the direct impingement, Si source atoms may also arrive at the droplet from the substrate surface due to the diffusion along the wire sidewalls [Figure 2.4(c)]. These atoms then dissolve in the droplet, diffuse to the interface, and finally incorporate into the lattice. It is believed that the tapering shape of nanowires can be explained by this model.[53,54]

However, it is not applicable to the growth at high temperature, because atoms detach fast from solid surfaces at high temperature.

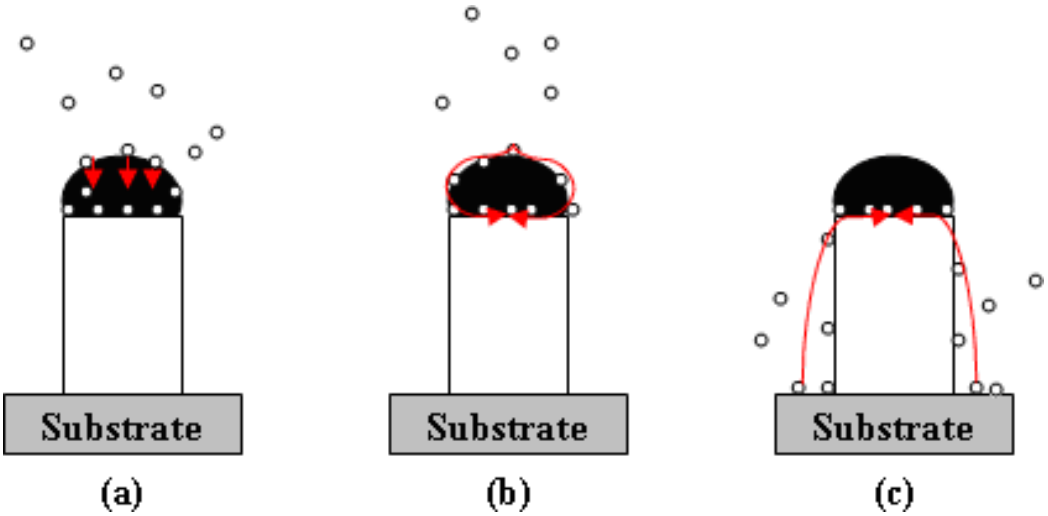


Figure 2.4 Different models describing the incorporation routes of source atoms into the growth interface of nanowire: (a) the classical VLS mechanism; (b) diffusion through the liquid droplet surface; and (c) diffusion through the nanowire sidewalls (redrawn from Reference 55).

(ii) Quasi-static model:

Schmidt *et al.*[56] derived a quasi-static model of epitaxial nanowire growth by considering the equilibrium condition for the contact angle of droplet. During the initial reaction of the catalyst on a flat surface [Figure 2.5(a)], the contact angle β_0 of the droplet is determined by the balance force of the surface tension, the liquid/solid interface tension, and the line tension (the interfacial energy at the three-phase contact zone) τ, by a modified Young's equation[57]

$$\sigma_L \cos(\beta_0) = \sigma_S - \sigma_{LS} - \frac{\tau}{r_0} \tag{2.6}$$

where σ_L is the droplet surface tension, σ_{LS} the liquid/solid interface tension, σ_S

the Si surface tension, and r_0 the radius of the catalyst contact area.

At the initial growth, when the nanowire's length increases, the nanowire diameter decreases and the radius of the contact area decreases [see Figure 2.5(b)]. The inclination angle α [shown in Figure 2.5(b)] of the nanowire flanks will increase. The inclination angle can be expressed as

$$\sigma_L \cos(\beta) = \sigma_S \cos(\alpha) - \sigma_{LS} - \frac{\tau}{r} \tag{2.7}$$

An increase in α is accompanied by an increase in β. Since the contact area decreases with an increase in the nanowire length, the final radius of the nanowire should be smaller than the initial one. The catalyst contact area is strongly influenced by the line tension. A large line tension can result in the hillock growth and thus stop the growth.[56]

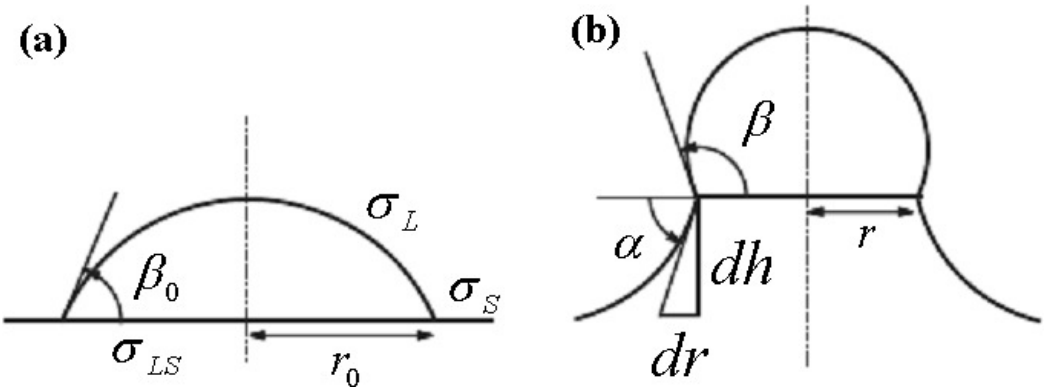


Figure 2.5 (a) Schematic of the Au/Si-eutectic droplet on a flat surface; and (b) schematic of the initial stage of nanowire growth (redrawn from Reference 56).

Based on the Schmidt's model, Li *et al.*[58] further developed the Equation 2.7 by using the minimization method of the system's Gibbs free energy:

$$\sigma_L \cos(\beta) = \sigma_S \cos(\alpha) - \sigma_{LS} - \sigma^c \tag{2.8}$$

$$\sigma^c = \sigma_{LS}^c + \frac{\tau^c}{r_0},\ \sigma_{LS}^c = -l_0 \frac{k_B T}{\Omega} \ln \eta, \text{ and } \tau^c = l_0 \sigma_S$$

where σ^c is defined as the chemical tension, σ_{LS}^c the effective surface tension, τ^c the effective line tension, l_0 the elementary thickness in the wire growth direction with an energy change for ensuring an equilibrium change to occur, k_B the Boltzmann's constant, T the absolute temperature, Ω the atomic volume of Si, and η the actual-to-equilibrium pressure ratio of the vapour source. The equilibrium condition of the VLS reaction is the balance among the various static factors in the system, the surface energies, the dynamic factors due to the growth of a crystal layer, and the chemical tension.

The quasi-static model explains the origin of the larger diameter of the nanowire base and predicts that nanowire growth can only take place within a certain range of line-tension values. However, there is no conclusive experimental evidence supporting those predictions.

2.2.3 Silicon Nanowire Heterostructures

SiNW heterostructures with modulated composition and/or doping enable passivation of interfaces and the generation of devices with diverse functions.[18] Nanowire heterostructures can be divided into two categories: axial and radial. In the axial heterostructures, sections of different materials are grown along the wire axis, while

in the radial heterostructures, core/shell(s) structures form around an existing nanowire.

Most work involving nanowire heterostructure synthesis has been performed using the VLS approach, because the VLS growth mechanism can be compatible with desired materials and offers the potential for good growth control. In VLS growth, heterostructures comprising different materials can be produced *in situ* by controlled variations in the gas flow during the growth.[59] There are two competing interfaces in a typical VLS process, the liquid/solid interface between the eutectic and the nanowire, and the vapour/solid interface between the reactants and the exposed sidewall surfaces of the growing nanowire. The precipitation through the first interface results in the axial elongation of the nanowire, while the dissociative adsorption on the second interface results in the vapour-solid growth and thickening in the radial direction. Either mechanism can dominate in an actual growth process, depending on the detailed growth conditions such as the pressure, flow rate, temperature, reactant species and background gases.[60] Therefore, once the nanowire growth has been established, a change in the reactant vapour leads to either the axial [Figure 2.6(c)] or radial heterostructure [Figure 2.6(d)].

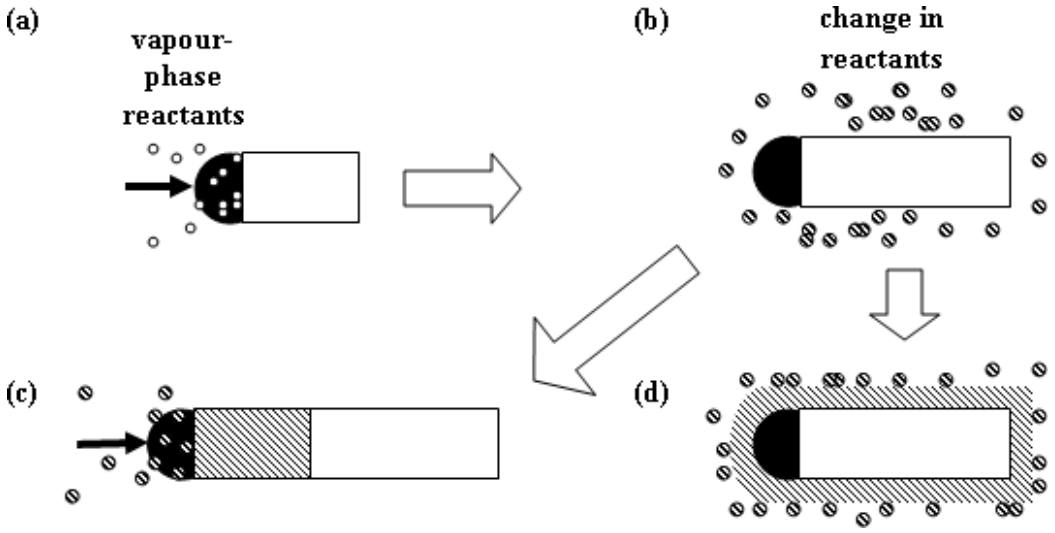


Figure 2.6 Schematic showing the nanowire heterostructure synthesis: (a) the preferential reactant incorporation at the catalyst (growth end) leads to the 1D axial growth; (b) a change in the reactant leads to either (c) the axial heterostructure growth or (d) the radial heterostructure growth, depending on whether the reactant is preferentially incorporated (c) at the catalyst or (d) uniformly on the wire surface (redrawn from Reference 60).

Controlled syntheses of both axial and radial SiNW heterostructures have been achieved. For example, Wu *et al.*[61] combined the CVD technique using silane tetrachloride with a laser ablation of a solid germanium target to produce the axial heterostructured Si-$Si_{1-x}Ge_x$ nanowires. Lauhon *et al.*[18] demonstrated the controlled growth of a radial homoepitaxial shell for the intrinsic Si/boron-doped Si core/shell nanowires via a CVD-based approach, in which the introduction of diborane (B_2H_6) during the SiH_4-based nanowire growth led to the substantial radial growth and the deposition of a boron-doped Si shell.

Despite the rapid progress demonstrated in the studies described above, much remains to be understood about the nature of heterointerface formation during the nanowire

growth. For instance, the successful fabrication of semiconductor electronic devices requires good control over the composition and perfection of interfaces;[62] however, there exist problems to form desirable interfaces for growing axial heterostructured nanowires. The main problem is the way to interrupt the process and to switch source materials. This is because the conditions for the incorporation of newly-added source into the catalyst droplet, such as the interruption time, temperature, vapour pressure, *etc*., strongly affect the quality of the axial heterostructured nanowires.[63, 64] Depending on the material systems, the abruptness of the interface is limited by the intermixing of two source elements as well as the solubility of the source materials in the catalyst droplet.[55] At any temperature above the eutectic point, there are always residual source materials in the droplet. Suppose that the heterojunction consists of materials A and B, at the beginning of growing material B on a nanowire containing only material A, the residual material A in the droplet will be mixed with the newly-added source B. Thus the chemical composition gradient will occur at the interface, resulting in a diffuse interface (see Figure 2.7).

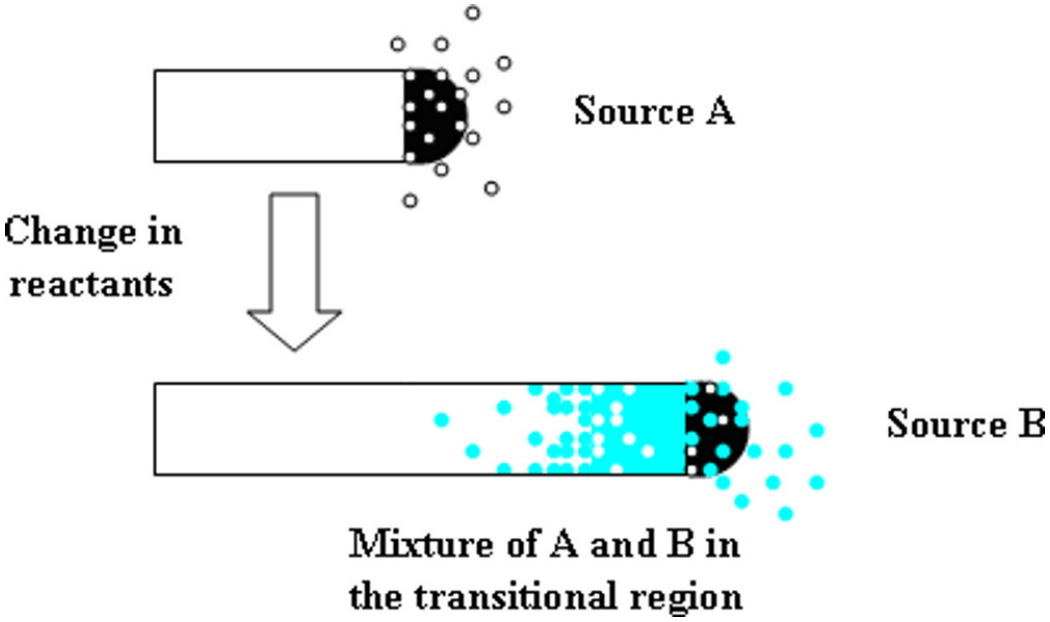


Figure 2.7 Schematic diagram showing the formation of a diffuse interface during the VLS growth of axial heterostructured nanowires (redrawn from Reference 55).

Another important factor that needs to be addressed is the relative efficacy of mass transport via sidewall surfaces versus the bulk diffusion through the catalyst droplet. If the majority of some components in the source materials are delivered to the growth interface by surface diffusion, rather than the bulk diffusion through eutectic, it could be much easier to accomplish the source depletion before switching, which could result in sharper interfaces. This question has been raised in the context of metal-catalysed carbon nanotube growth,[65] but is also interesting to consider in the case of nanowire growth.

2.2.4 Doping of Silicon Nanowires

Introducing impurities into semiconducting materials is the primary method to control

their electrical conductivity, band gap and carrier type. A semiconductor can be doped to conduct with negative electrons (*n*-type) or positive holes (*p*-type), enabling *p*-*n* junctions (diodes) and transistors to be formed.

Both *p*- and *n*-type SiNWs can be used as building blocks to assemble semiconducting nanodevices, such as FETs,[66,67] and electrodes in high-performance batteries.[68] Single-crystalline *p*-type and *n*-type SiNWs have been prepared by introducing boron or phosphorus dopants during the growth. Zheng *et al.*[69] synthesized *n*-type SiNWs with well-controlled diameters in a gold nanocluster mediated VLS process with phosphine (PH_3) as the dopant precursor. Whang *et al.*[70] studied the effects of boron-doping (or B-doping) on the structure of the VLS-grown SiNWs, and observed that the Au-catalysed SiNWs grown with B_2H_6 gas exhibited significant morphological changes, resulting in cone-shaped SiNWs [Figure 2.8(b)]. Pan *et al.*[71] reported a continuous loss of Au along the B_2H_6-doped SiNWs grown via a VLS mechanism using Au as a catalyst [Figure 2.8(c)]. Lew *et al.*[72] demonstrated the successful VLS synthesis of *p*-type SiNWs by using trimethylboron (TMB) as an alternative dopant source compared to B_2H_6, and found that the B_2H_6-doped SiNWs consist of a crystalline core with a thick amorphous Si shell while the TMB-doped SiNWs are predominantly single- or bi-crystalline even at high boron concentrations [Figure 2.8(d) and (e)].

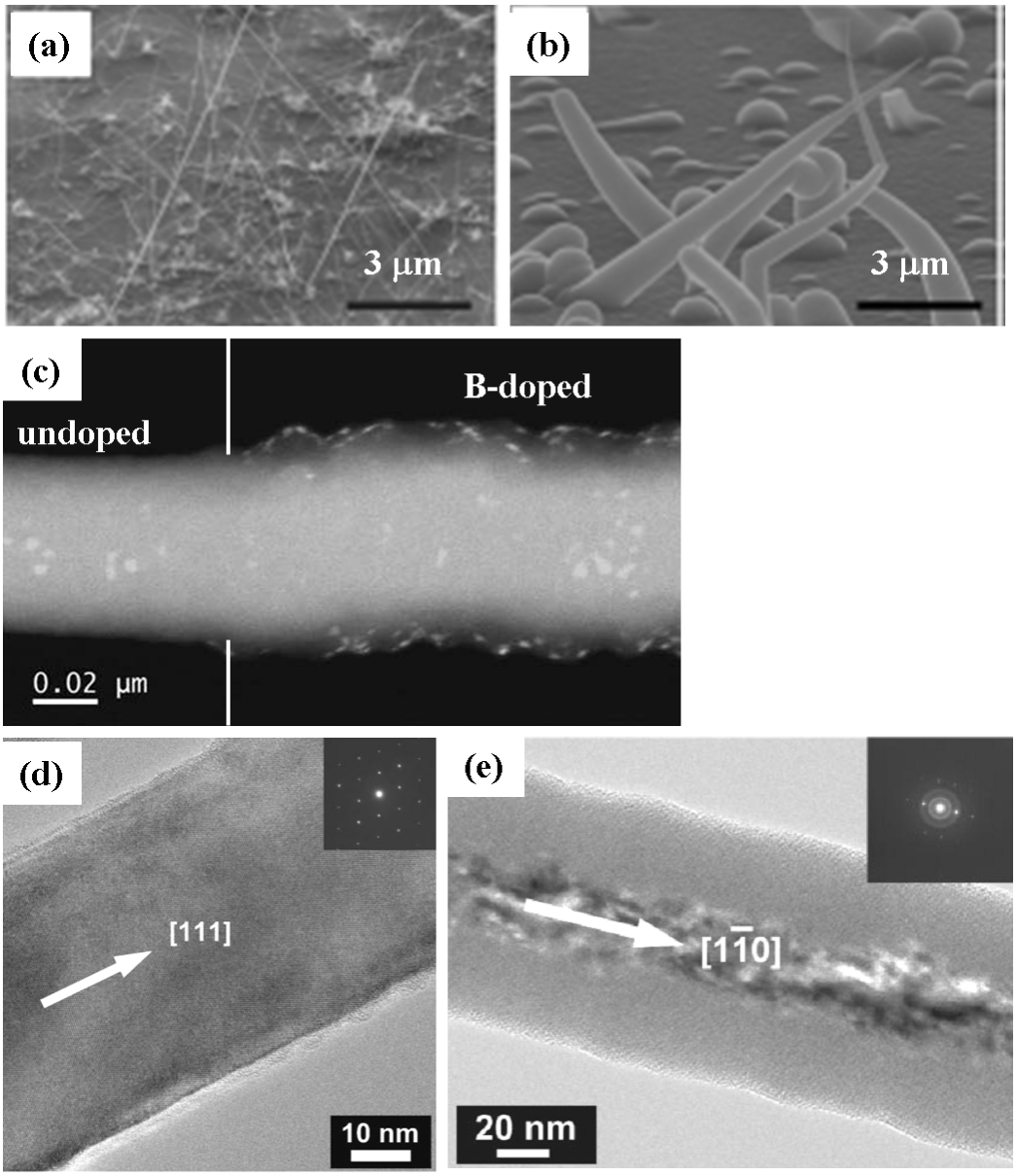


Figure 2.8 Experimental examples showing the effects of boron doping on the microstructures of SiNWs: SEM images of (a) the undoped SiNWs; and (b) the cone-shaped B_2H_6-doped SiNWs from the Au-catalysed VLS process (from Reference 70); (c) STEM images showing the undoped-B doped transitional area in SiNWs (from Reference 71); HRTEM images of (d) the TMB-doped SiNW; and (e) the B_2H_6-doped SiNW (from Reference 72).

In order to understand the physical significance of the dopant distribution and interfacial junction, as well as their implications in device operation and performance, an in-depth understanding of the effects of doping on SiNW microstructures and the

mechanisms of dopant incorporation into the SiNWs are needed. However, such information is still not thorough at present.

2.2.5 Growth of Axially Doped Silicon Nanowire Heterostructures

In this thesis, axial heterostructured SiNWs with varying *n*- and *p*-doping were grown by the industrial collaborators using the VLS approach. Two types of samples were prepared. For the first, a thin film (~1 nm) of Au was thermally evaporated on an oxide-removed Si{111} substrate. When heated the film ripened to form Au nanoclusters. For the second, Au colloids with a mean diameter of 100 nm were deposited on an oxide-removed Si{111} substrate. These two alternatives were used to check that the nanofaceting (to be discussed in Chapter 5) occurred on the sidewalls of both the thin film-derived and the colloid-derived SiNWs, indicating that the method of generating Au nanoclusters to catalyse nanowire growth has no influence on the nanofaceting. Both samples were then heated to ~600 °C in a FirstNano EasyTube™3000 LPCVD system. SiNW growth was initiated by flowing SiH_4 gas. The SiNWs were either *n*- or *p*-doped by introducing PH_3 or B_2H_6 gas, respectively, to form the axially doped nanowire heterostructure with *p*-type (boron-doped or B-doped), *n*-type (phosphorus-doped or P-doped), and intrinsic Si (*p*-*n*-*i* SiNWs) (Figure 2.9). A growth rate of 325 nm/min was used in all cases, with a gas pressure of 10 Torr and a gas flow rate of 6 standard cubic centimetres per minute (SCCM). A reference nanowire sample consisting of intrinsic, *p*-type (B-doped), *n*-type (P-doped),

and intrinsic Si (*i-p-n-i* SiNWs) was grown using the same method in order to study the effects of the doping sequence on the nanowire sidewall morphology (Figure 2.9).

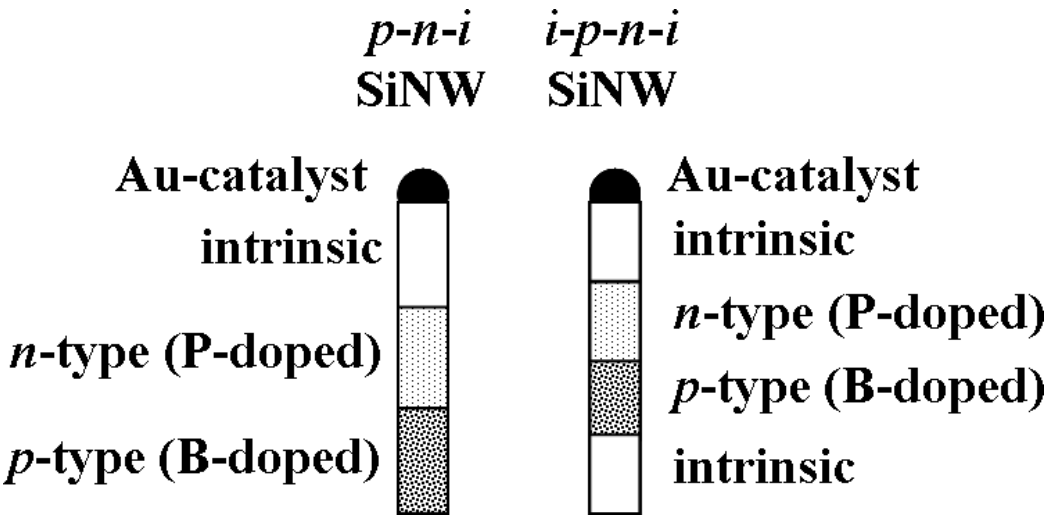


Figure 2.9 Schematic showing the structure of the axially doped SiNWs with varying *n*- and *p*-doping.

2.3 Zero-dimensional Indium Nitride Colloidal Nanoparticles

2.3.1 General Introduction

Indium nitride (InN) is a group III-V semiconductor which has potentially important applications in many functional devices, such as solar cells,[73] FETs,[74] and light-emitting diode (LED) devices.[75,76,77] In particular, 0D InN nanoparticles (also known as quantum dots) are expected to exhibit interesting size- and shape-dependent electronic and optical properties due to their size reduction.[78,79] Among various nanoparticles with different topologies, free-standing colloidal nanoparticles grown via chemical routes are of great interest, because of their potentially flexible

processing chemistry.[80] Generally, colloidal nanoparticles in solution are crystalline clusters passivated by some inert organic long chain molecules (surfactants), which are called ligands or capping groups. Such ligands ensure that the particles do not agglomerate or ripen to form larger particles. However, reports on free-standing InN colloidal nanoparticles are scarce in the literature, because their growth is the most difficult to achieve among the group III-nitrides.[81,82] Due to the lack of successful synthesis, fundamental microstructural and physical properties of InN in the form of nanoscale particles have not been well studied. Therefore, it is interesting to investigate these properties of InN colloidal nanoparticles and to understand their structure-property relationships. To uncover these size-dependent properties, it is necessary to review the research associated with the colloidal growth of InN nanoparticles, which dictates their microstructural properties.

2.3.2 Growth of Indium Nitride Colloidal Nanoparticles

The growth of InN is the most difficult among the group III-nitride semiconductors, because of its low dissociation temperature (500~550 °C)[83,84,85] and impurity incorporation problems.[86] Therefore, it is still a challenge to grow high quality InN nanostructures (*e.g.*, InN nanoparticles). Up to now, there are only a few papers that have reported the growth of InN nanoparticles. For example, self-assembled InN quantum dots have been grown on suitable substrates by molecular beam epitaxy (MBE)[87,88,89,90] or metalorganic vapour phase epitaxy (MOVPE)[91,92,93,94,95], with the

optimum V/III ratio and growth temperature. A highly ordered uniform InN nanodot array has been obtained by using radio frequency (RF) magnetron sputtering with the aid of an anodic nanohole channel alumina template.[96] However, both MBE and MOVPE processes require very strict fabrication conditions and complicated post fabrication process. The template-directed synthesis needs to selectively remove the template,[97] and such processes may damage the original nanostructures or incorporate some undesirable impurities.

In contrast, the solution-phase colloidal synthetic approach is an especially powerful process for synthesizing nanoparticles with better control in the particle size, shape and compositions at the nanoscale. In a typical synthesis process for colloidal nanoparticles, when the reaction medium is heated to a sufficiently high temperature, the precursors chemically decompose or react into active atomic or molecular species (monomers). The nucleation of an initial "seed" for nanoparticle growth occurs when the supersaturation of monomers is reached. These nuclei then grow by incorporating additional monomers still present in the reaction medium. The subsequent growth of nanoparticles is greatly affected by the presence of surfactant molecules. This is because the surfactants not only bind to the surfaces of growing nanoparticles, but also form a complex with reactive monomers upon heating. The binding energy of surfactants to the growing nanoparticle surface, as well as the stability and diffusion rate of these complexes strongly affect the growth mechanisms of nanoparticles.[98] Therefore, choosing appropriate precursor and surfactant molecules as well as suitable

temperature range is important in obtaining control over the colloidal nanoparticle growth.

However, there are also some drawbacks in the chemical synthesis for colloidal nanoparticles, such as the chemical instability, high cost, toxicity of organic precursors, and limitations in choosing appropriate ligands. Owing to these difficulties, chemically synthesized InN colloidal nanoparticles have not been widely reported in the literature. Bai *et al.*[99] synthesized InN nanoparticles from the solvo-thermal reaction of $InCl_3$ and Li_3N at 250 °C with xylene as the solvent. Sardar *et al.*[100] reported the formation of the InN colloidal nanoparticles by the solvo-thermal reaction of tris(N-nitroso-phenylhydroxylaminato)indium and 1,1,1,3,3,3,-hexamethyldisilazane in toluene at 265 °C. Dingman *et al.*[101] obtained the InN colloidal nanoparticles by thermolysis of tBu$_2$InN$_3$ in refluxing 1,3-diisopropylbenzene at a low temperature of 203 °C. By reacting indium acetate with tris(trimethylsilyl)amine using octadecene as solvent and myristic acid as ligands, Greenberg *et al.*[102] synthesized the InN colloidal nanoparticles of ~60 nm in diameter. A benzene thermal conversion route was developed by Xiao *et al.*[103] to prepare the nanocrystalline InN at 180~200 °C by reacting $NaNH_2$ with In_2S_3. Schofield *et al.*[104] synthesized InN nanoparticles by decomposing $InN_3(CH_2CH_2CH_2NMe_2)_2$ in trioctylphosphine oxide and toluene.

In this work, an innovative wet-chemistry method was designed by the industrial

collaborators to synthesize the InN colloidal nanoparticles. Zinc-containing organic ligands were used to passivate the surface of nanoparticles. To obtain the InN colloidal nanoparticles with different sizes and size distributions, the solution-phase reactions were carried out for 10, 20 and 30 minutes, respectively. Detailed preparation procedures are not described here, as they are commercially sensitive background intellectual property belonging solely to the industrial collaborators.

2.4 Research Objectives

1D and 0D semiconductor nanostructures have become a focus of research, owing to their unique properties in mesoscopic physics and potential applications in nanoscale functional devices. However, some scientific and technological challenges still exist in these research areas.

First of all, the enhancement of physical properties of semiconductor nanostructures and their performance in devices requires a deeper understanding of their fundamental microstructural properties, which are correlated to nanostructure growth mechanisms. Understanding the growth mechanisms is important for growth optimization to achieve semiconductor nanostructures with tuneable chemical compositions, morphology and crystalline structures, since these characteristics determine the physical properties and ultimately the functionality of the devices based on semiconductor nanostructures.

Secondly, one of the main advantages of the use of semiconductor nanostructures in nanodevices, as opposed to carbon nanotubes, stems from their inherent semiconducting character which allows conductance to be controlled by using doping processes similar to those used in conventional CMOS processes. However, it is still not fully understood how dopants are incorporated during the growth and how the presence of dopants affects the microstructures of semiconductor nanostructures. Therefore, it is necessary to understand how, and under which conditions, dopants incorporate into the nanostructures, and then to study the effects of doping on their microstructural properties.

Thirdly, due to the high surface area to volume ratio of 1D and 0D nanostructures, the surface plays an important role in controlling nanostructure properties, and an important issue for functional devices based on these nanostructures is the good control of their surface morphology. For example, in a nanowire-based FET geometry [as shown in Figure 2.2(a)], the nanowire is surrounded by a gate dielectric. It is thus necessary to achieve a uniform cross section of the gate dielectric and to minimize the carrier scattering at rough interfaces. Therefore, it is important to study the surface properties of nanowires and to understand the factors that influence the nanowire morphology.

Fourthly, the phase purity and growth-related defects of semiconductor nanostructures strongly influence the quality and the ultimate performance of the nanostructure-based

devices. An understanding of the fundamentals of phase and defects formation is of great importance to optimize the nanostructure growth. This will require further knowledge of the conditions under which 1D nanowires or 0D nanoparticles preferentially form, and how the various growth mechanisms differ from each other.

Last but not least, the dimensionality of 1D and 0D semiconductor nanostructures plays an important role in determining their microstructural and physical properties. Understanding these size-dependent properties of semiconductor nanostructures is necessary to tune their properties through size and shape control.

Considering these challenges, the research carried out in this thesis is focused on the experimental and theoretical studies of the microstructural properties of two important semiconductor nanostructures, 1D axial heterostructured SiNWs with varying doping and 0D InN colloidal nanoparticles, with emphases on the following aspects:

(i) to study the structural properties of 1D axially doped SiNWs, such as the dimension, growth direction, morphology, phase purity and growth defects, using advanced characterization tools such as electron microscopy (EM);

(ii) to understand the dependence of doping on the morphology of SiNWs;

(iii) to understand the growth mechanisms that explain how the 1D growth occurs and determines the microstructures;

(iv) to check the formation of 0D InN colloidal nanoparticles grown from solution-phase reactions by examining their compositions, crystalline

structures and shape.

(v) to understand the dependence of microstructural and optical properties on the size of 0D InN colloidal nanoparticles.

2.5 Chapter Summary

This chapter reviews the literature relating to two important semiconductor nanostructures studied in this thesis, *i.e.*, 1D axial heterostructured SiNWs with varying doping and 0D InN colloidal nanoparticles. In the interest of relating their microstructural properties to the 1D and 0D nanostructure growth, the growth mechanisms are discussed. In particular, to be able to fully tune the microstructural properties (and then the physical behaviour) of these semiconductor nanostructures through synthesis, it is necessary to have a deeper understanding on their fundamental microstructural properties and the mechanisms that dictate the microstructural formation during the growth. These are the main objectives of this thesis.

Chapter 3

Characterization Methods

3.1 Introduction

As proposed in Chapter 2, the objective of this thesis is to investigate and to understand the microstructural properties of two important semiconductor nanostructures, *i.e.*, 1D axially doped SiNW heterostructures and 0D InN colloidal nanoparticles. To study this, advanced characterization tools, such as electron microscopy (EM) and Raman spectroscopy, play an important role in revealing the microstructures of nanoscale materials. In this thesis, 1D axially doped SiNW heterostructures were synthesized on Si{111} substrates using a gold-catalysed VLS method, and 0D InN colloidal nanoparticles were grown using a solution-phase chemical method by the industrial collaborators (growth methods are described in Chapter 2). Before discussing the microstructural properties of these two semiconductor nanostructures, this chapter will introduce the characterization

techniques used in this thesis, including TEM, HRTEM, STEM, EDX, SEM and Raman Spectroscopy.

3.2 Transmission Electron Microscopy

3.2.1 Introduction

The first TEM was built by Knoll and Ruska[105] in 1931. TEM is a technique whereby a beam of electrons is transmitted through an ultra-thin specimen, interacting with the specimen as it passes through it. An image is formed from the electrons transmitted through the specimen, magnified and focused by an objective lens and projector lenses, and appears on an imaging screen, or on a layer of photographic film, or to be detected by a sensor such as a charge-coupled device (CCD) camera.

A typical TEM is comprised of five systems, including illumination, specimen stage, imaging, magnification and data recording systems. The structure of a TEM is illustrated in Figure 3.1.

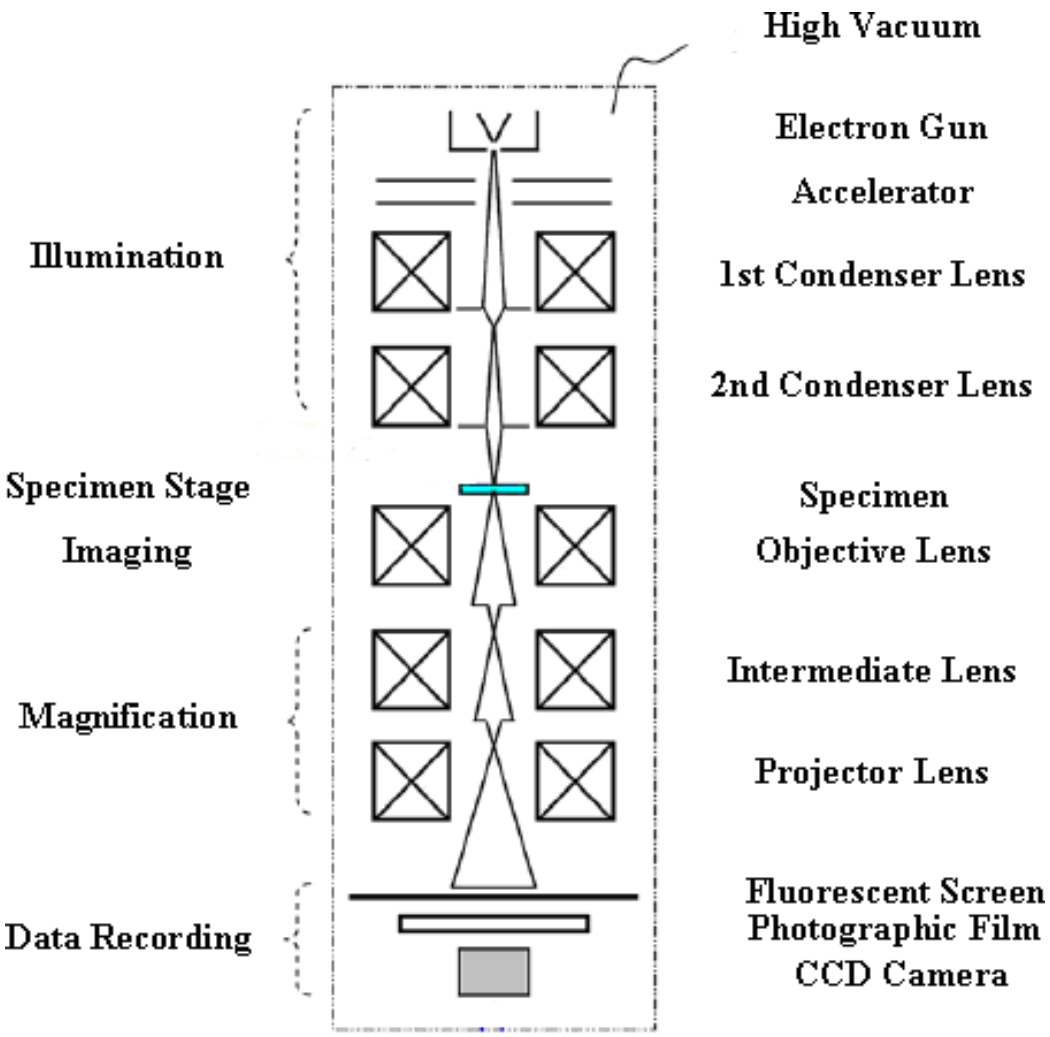


Figure 3.1 Schematics of a typical TEM consisting of five systems: illumination, specimen stage, imaging, magnification and data recording systems.

In a TEM, the electron gun produces a stream of high-energy electrons, which is then focused towards the specimen by a set of the condenser lenses and apertures. The beam is restricted by the condenser aperture, which removes high-angle electrons to increase the resolution, then it strikes the specimen and parts of it are transmitted. The objective lens forms an initial image in an intermediate image plane and a diffraction pattern in the back focal plane. Optional objective and selected area apertures can restrict the beam. The objective aperture enhances the contrast by blocking out high-

angle diffracted electrons, while the selected area aperture can be used to select an area of the specimen from which a diffraction pattern is formed. The diffraction pattern or the image is enlarged and passed down the column through the intermediate and projector lenses, followed by being observed in image screen or detected by camera. The former is called the diffraction mode [Figure 3.2(a)] and the latter the image mode [Figure 3.2(b)].[106]

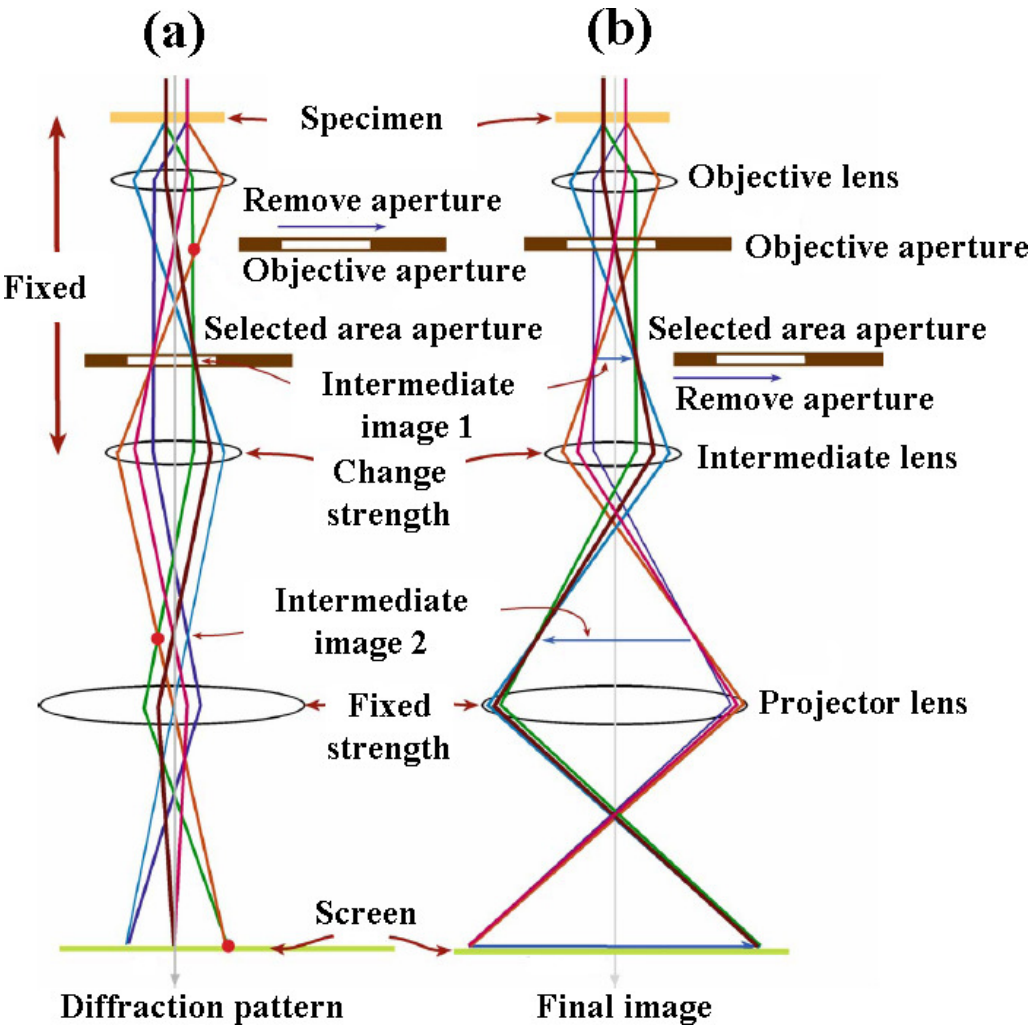


Figure 3.2 The two basic operations of the TEM imaging system involve (a) the diffraction mode; and (b) the image mode. The intermediate lens selects either (a) the back focal plane or (b) the image plane of the objective lens as its object (redrawn from Reference 107).

3.2.2 Electron Diffraction

Electron diffraction provides important information of crystal structures of materials. For example, diffraction can be used to determine the spacing of planes in crystals, and the interplanar spacings in different crystal structures are characteristic of that structure. A crystalline specimen will diffract the electron beam strongly at a certain incident angle (the Bragg angle θ_B) with respect to the diffracting planes. The Bragg angle is dependent on electron wavelength λ and crystal lattice spacing d:[108]

$$2d \sin \theta_B = n\lambda \tag{3.1}$$

This is Bragg's law (Equation 3.1), where n is an integer representing the number of wavelengths required for constructive interference to occur.

In 1913, Ewald[109] demonstrated the use of the Ewald sphere together with the reciprocal lattice to understand diffraction. The reciprocal lattice vectors lie in "reciprocal space", an imaginary space where planes of atoms are represented by reciprocal points. The reciprocal vector g_{hkl} is the inverse in magnitude of the real vector and is normal to the planes separating the original vector:

$$\left|g_{hkl}\right| = \frac{1}{d_{hkl}} \tag{3.2}$$

where $\left|g_{hkl}\right|$ represents the length of the reciprocal vector.

Electron diffraction can be described in reciprocal space by the Ewald sphere construction. The Ewald sphere is usually represented by a circle with a radius of $\frac{1}{\lambda}$ in 2D, as shown in Figure 3.3. If any point in the reciprocal lattice intersects the surface of the sphere, the set of planes corresponding to that point must satisfy the Bragg equation and hence the planes will diffract strongly. As shown in Figure 3.3, point O is the origin of the reciprocal lattice. Vectors k_0 and k_D represent the wave vectors of the incident and diffracted waves, respectively, and $|k_0| = |k_D| = \frac{1}{\lambda}$. The vector K is the change due to diffraction, and the magnitude of K is

$$|\mathrm{K}| = \frac{2\sin\theta_B}{\lambda} = \frac{n}{d_{hkl}} = n\left|g_{hkl}\right| \tag{3.3}$$

However, one should note that electron diffraction has unique characteristics when compared to X-rays. For example, due to the small wavelength of electrons (*e.g.*, $\lambda = 1.97$ pm for 300 kV electrons), the radius of the Ewald sphere $\frac{1}{\lambda}$ is quite large, therefore the surface of the Ewald sphere is almost planar relative to reciprocal lattice vector lengths. In addition, the lattice points in the reciprocal lattice of a thin specimen are elongated so that the Ewald sphere intersects several of the reciprocal-lattice rods (see Figure 3.3, the rod shape is due to the fact that TEM specimens are very thin in real space, leading to an elongation of the reflections in reciprocal space). Because of that, diffraction occurs even if the Bragg condition is not exactly satisfied, and many reflections appear simultaneously.

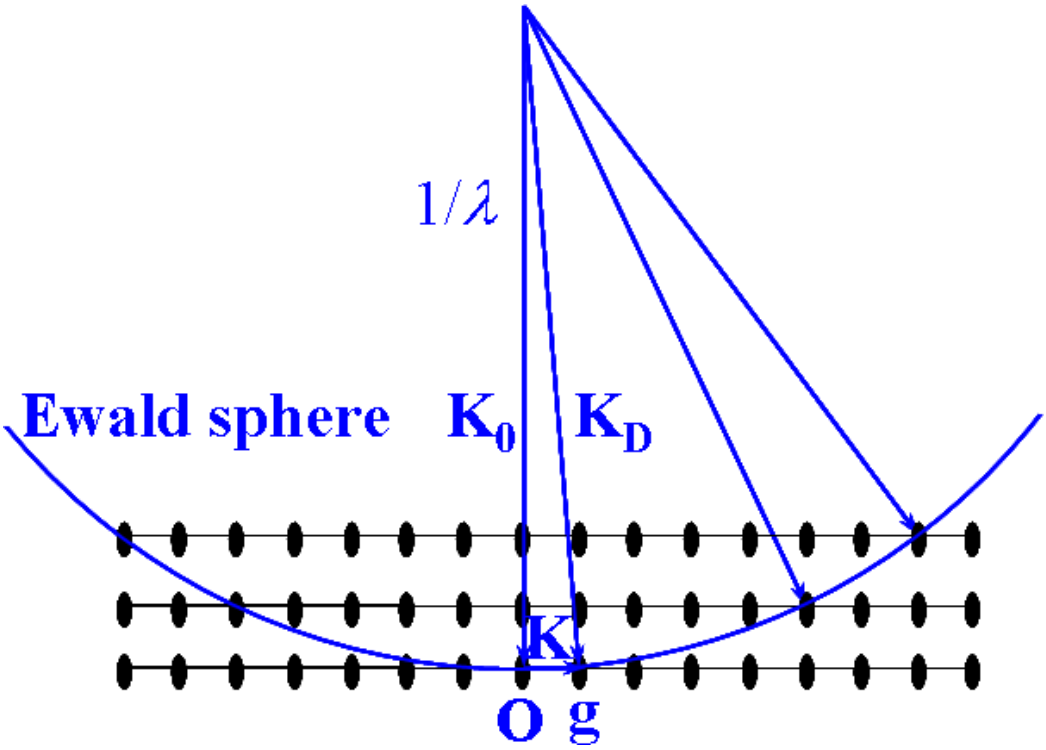


Figure 3.3 The Ewald sphere construction.

Single-crystalline electron diffraction patterns (EDPs) are normally obtained by orienting the specimen such that the beam is incident almost parallel to a low-index zone axis. The observed zone-axis pattern can be compared with standard ones, if the crystalline structure of the specimen is known. Lattice parameters can be obtained from the diffraction patterns if the camera length of the TEM is calibrated with known reference materials. In addition, the orientation of a crystalline specimen can be determined by indexing its EDPs.

As shown in Figure 3.4, if electrons are scattered through an angle $2\theta_B$ at the specimen, then the distance between the direct and diffracted beams as measured on the screen R, is determined by L, since

$$\frac{R}{L} = \tan 2\theta_B \sim 2\theta_B, \text{ assuming small scattering angles} \quad (3.4)$$

From the Bragg equation (Equation 3.1), $\frac{\lambda}{d} = 2\sin\theta_B \sim 2\theta_B$, thus Equation 3.4 can be written as

$$Rd = \lambda L \quad (3.5)$$

The diffraction pattern is a projection of the reciprocal lattice, the angle between the lines joining spots $h_1k_1l_1$ and $h_2k_2l_2$ to spot 000 is the same as the angle between the $(h_1k_1l_1)$ and $(h_2k_2l_2)$ planes. Using these two relations between the diffraction pattern and the reciprocal lattice, one is able to index the EDPs from a specimen of known crystalline structure.

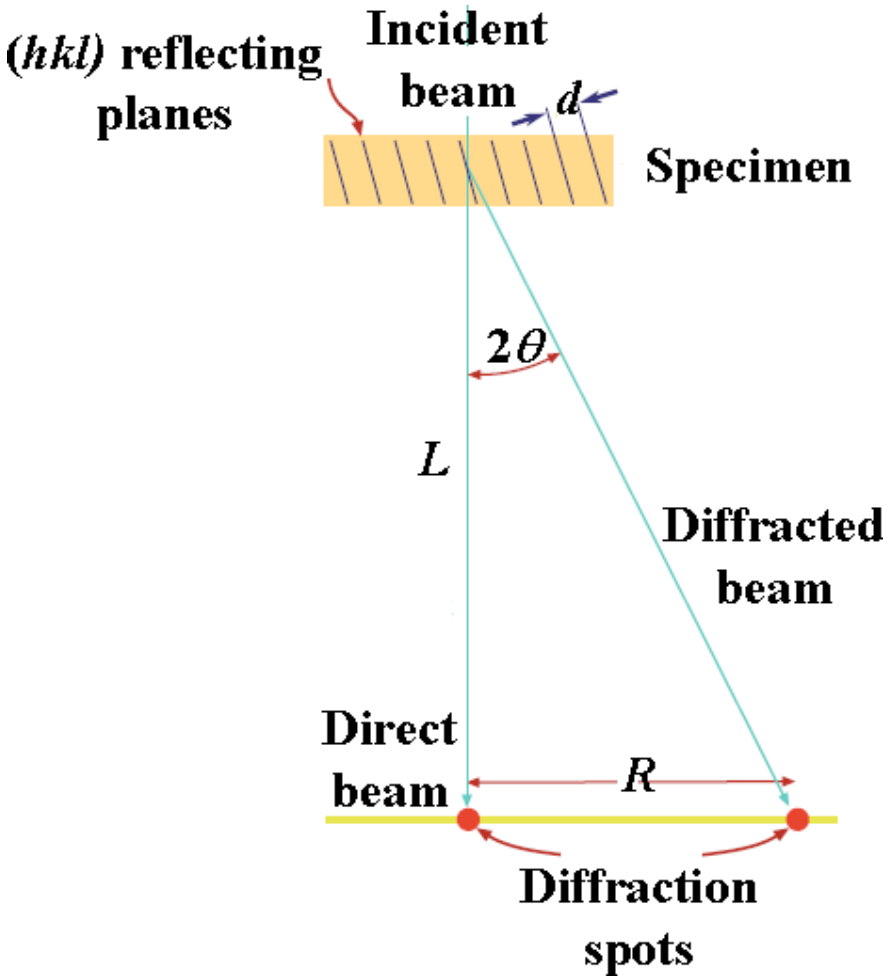


Figure 3.4 The spacing *R* between the direct beam and a scattering maximum (such as a diffracted beam or the radius of a ring of diffracted intensity) is related to the camera length *L* (redrawn from Reference 107).

3.2.3 Imaging

Diffraction contrast can be achieved by placing an objective aperture at the back focal plane. A bright-field (BF) image is formed by placing the objective aperture around the direct beam [Figure 3.5(a)] and a dark-field (DF) image comes from any of the diffracted beams [Figure 3.5(b)].

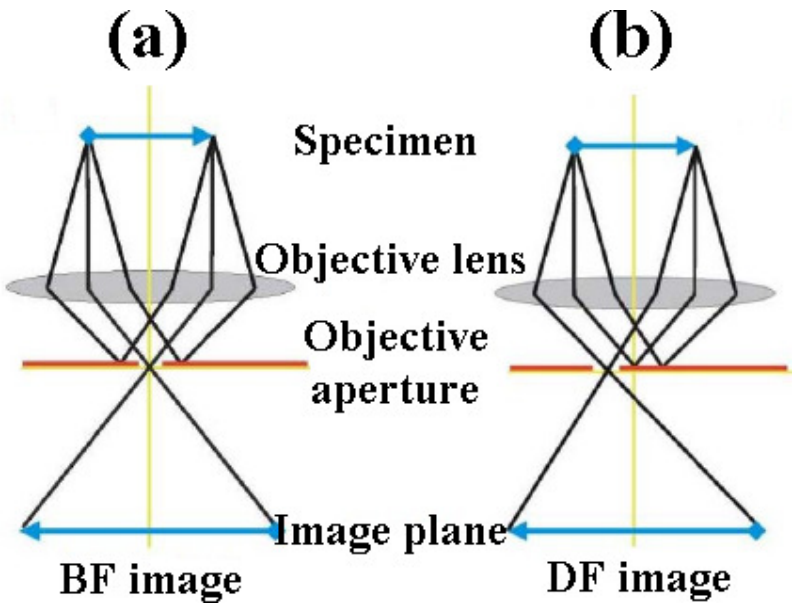


Figure 3.5 Comparison of the use of an objective aperture in TEM to select (a) the direct or (b) the scattered electron to form (a) BF and (b) DF images, respectively (redrawn from Reference 107).

In this thesis, EDPs and TEM imaging of axial heterostructured SiNWs were obtained using a JEOL JEM-2000FX TEM operating at 200 kV. A double tilt specimen holder was used, with maximum tilt angles of +/–45° along both axes. The TEM specimen of SiNWs was prepared by sonicating the as-grown SiNWs in acetone after growth to remove the nanowires from the growth substrate. The suspension was then drop-cast onto a TEM finder grid with a nominally 20 nm thick holey carbon support film (thickness as given by the product information from manufacturers).

3.3 High Resolution Transmission Electron Microscopy

High resolution transmission electron microscopy (HRTEM) is an imaging mode of TEM that allows the imaging of the crystallographic structure of a sample at an

atomic scale. Because of its high resolution, it is an invaluable tool to study nanoscale properties of crystalline materials such as semiconductor nanostructures.

3.3.1 Phase Contrast

The imaging mechanism of HRTEM is phase contrast. When the electron wave interacts with a sufficiently thin specimen, the amplitude changes caused by inelastic scattering will be small. It is thus assumed that the electron wave only suffers a phase change that depends on the projection of the potential along a straight-line path through the thin specimen. The phase change between the wave traversing the specimen and the wave transmitted through a vacuum is given by

$$\alpha \approx \sigma \varphi_P(r) \tag{3.6}$$

where $\varphi_P(r)$ is the projected potential along the electron beam incident direction, and σ ($\sigma = \frac{\pi}{\lambda E}$) is an interaction constant. The wave of the incident electrons can be approximated as a plane wave, so the transmission function can be expressed as

$$\psi_e(r) = \exp[-i\sigma\varphi_P(r)] \tag{3.7}$$

Equation 3.7 is called the phase object approximation (POA). The phase of the electron wave carries the information about the thin specimen and generates contrast in the image, thus the name phase contrast imaging.

In the back focal plane, interference of the waves generated at the specimen gives the diffraction pattern. Mathematically, the diffraction function in the back focal plane

can be written as

$$\phi(u) = F[\psi_e(r)] \tag{3.8}$$

where u is a vector in the diffraction plane (reciprocal space), the spatial frequency for a particular direction, and F is the Fourier transform operation. Afterwards, interference of the waves from the back focal plane recreates the specimen wave function in the image plane. The formation of the image is then described by two successive Fourier transform operations. The image function in the image plane is

$$\psi(r) = F[\phi(u)] = F\{F[\psi_e(r)]\} \tag{3.9}$$

For an ideally perfect lens, all rays leaving the specimen would be recovered with exactly the correct phase relationship to form the image, thus the image gives an exact reproduction of the transmission function of the thin specimen. However, in practice no perfect lens exists, *e.g.*, some of the scattered rays are lost because they fall outside the lens aperture (this affects amplitudes in the image plane), and phase relationships are affected by lens aberrations. In 1936, Scherzer[110] proved that the spherical and chromatic aberrations of a rotationally symmetric, static, space-charge-free, dioptric lens for electron beams cannot be eliminated. Spherical aberration is due to a lens being stronger at its edge than closer to its axis, and chromatic aberration is due to variations in energy (wavelength) of the electron waves reaching the image plane. As a result of these lens aberrations, a point in the specimen is imaged in the image plane as a disc. Therefore, the image function in the image plane is modified by a contrast transfer function (CTF), $H(u)$. $H(u)$ is the Fourier transform of the spread function

$h(r)$, which describes how a point spreads into a disc. Therefore, the modified image function is:

$$\psi'(r) = F\{F[\psi_e(r)]H(u)\} \tag{3.10}$$

The electron path through an objective lens is schematically shown in Figure 3.6.

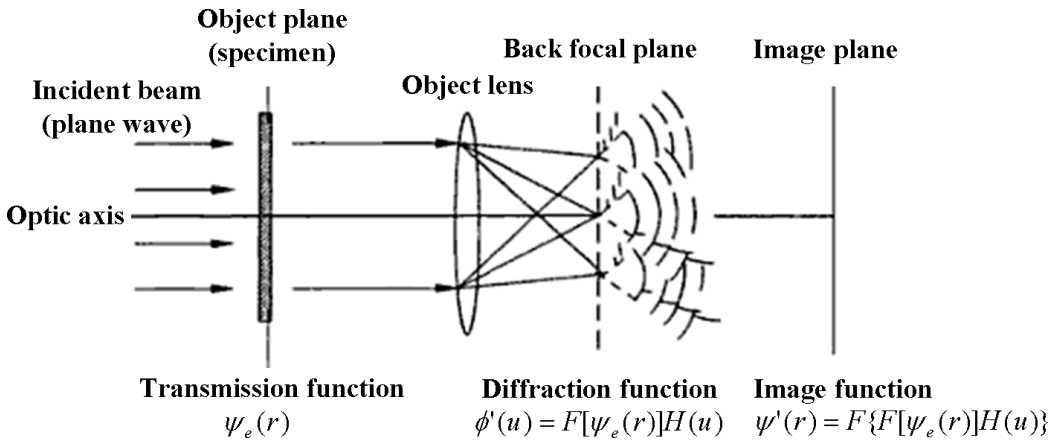


Figure 3.6 Schematic diagram of the image formation of HRTEM (redrawn from Reference 111).

Three factors including apertures, the attenuation of the wave and the aberration of the lens, contribute to the CTF, thus $H(u)$ is expressed as the product of these three terms

$$H(u) = A(u)E(u)\exp[i\chi(u)] \tag{3.11}$$

where $A(u)$ is the aperture function which can be expressed as a step function and represents the information cut off by the objective aperture, $E(u)$ is the envelope function, which describes the attenuation of the wave by the spatial coherence of the source and by chromatic effects, and the term $\chi(u)$ in Equation 3.11 is a function of the aberrations of the electron optical system, which is given by

$$\chi(u) = \pi\Delta f\lambda u^2 + \frac{\pi}{2}C_S\lambda^3 u^4 \tag{3.12}$$

where C_S is the spherical aberration coefficient, λ is the electron wavelength, and Δf

is the defocus.

3.3.2 Weak Phase Object Approximation

The correlation between the specimen structure and the image contrast can not be simply found from Equation 3.10. However, the discussion of phase contrast imaging for thin specimens becomes simpler if it is possible to make the further assumption that the phase changes of the electron wave are also small [the so-called weak phase object approximation (WPOA)].[107] Then Equation 3.7 can be approximated as

$$\psi_e(r) = \exp[-i\sigma\varphi_P(r)] \approx 1 - i\sigma\varphi_P(r) \tag{3.13}$$

The constant 1 in Equation 3.13 then represents the directly transmitted wave unaffected by the specimen, the $i\sigma\varphi_P(r)$ is the scattering function, and the i indicates a phase change of $\frac{\pi}{2}$. For a $\frac{\pi}{2}$ phase shift in a small-amplitude scattered wave, the resultant wave has only a slight phase modulation but no amplitude modulation, so it means that the image contrast is zero [Figure 3.7(a)]. To derive some information from the image concerning the specimen structure, an additional phase shift is needed to bring the scattered wave either exactly into [Figure 3.7(b)] or out of phase [Figure 3.7(c)] with the primary wave.

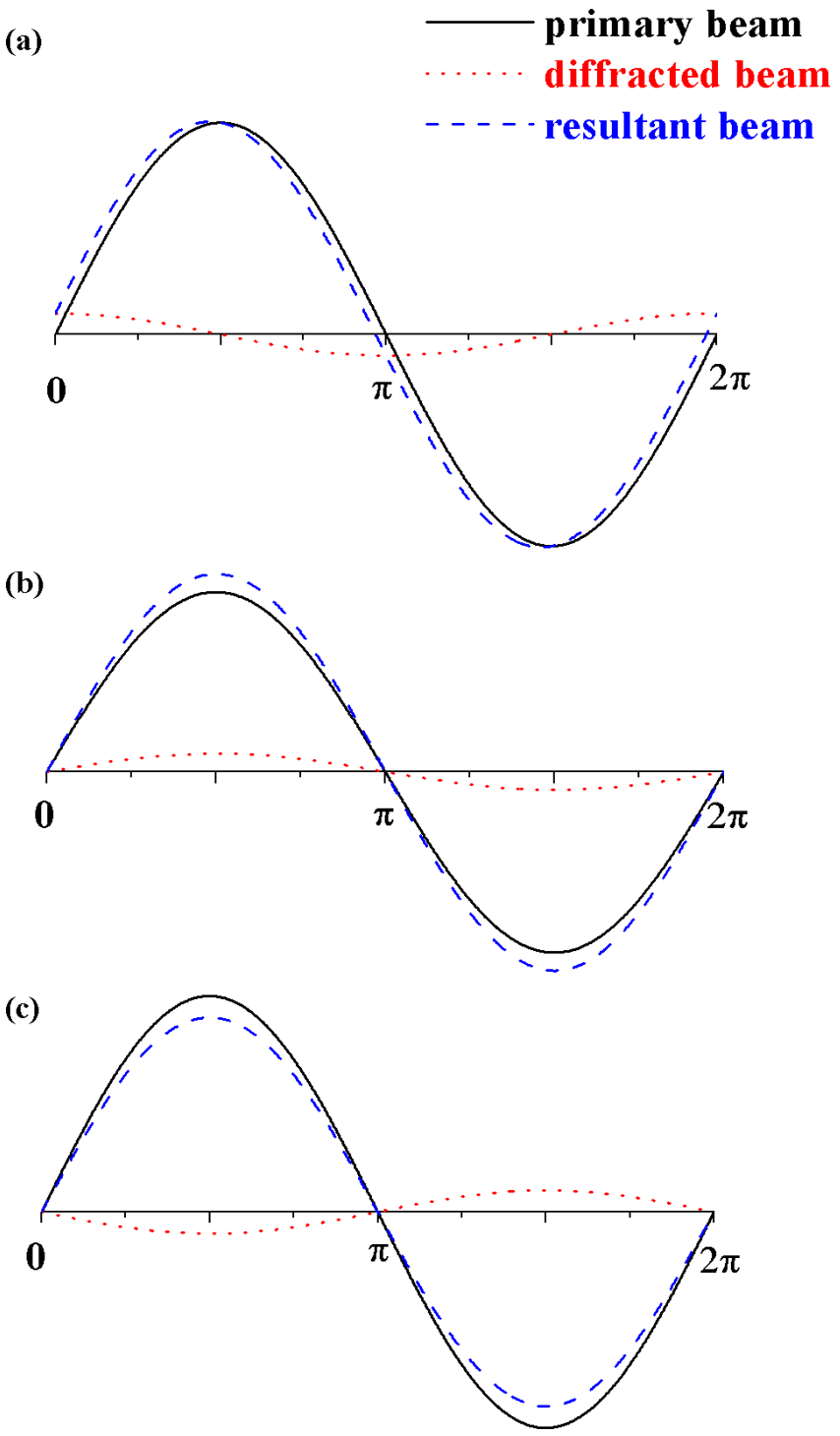


Figure 3.7 Schematic showing (a) a $\frac{\pi}{2}$ phase shift in a small-amplitude scattered wave, the resultant wave has only a slight phase change but no amplitude change; an additional phase shift brings the scattered wave either exactly (b) into or (c) out of the phase with the primary wave.

In practice, the effects of an imperfect lens will give some image contrast. When the WPOA holds, Equation 3.10 becomes

$$\psi'(r) = [1 - i\sigma\varphi_P(r)] \otimes F[H(u)] \tag{3.14}$$

where ⊗ sign in Equation 3.14 represents the convolution process. The image intensity is found by multiplying $\psi'(r)$ by its complex conjugate:

$$I = \left|\psi'(r)\right|^2 \tag{3.15}$$

It is noted that in the WPOA, only the imaginary part of the term $\exp[i\chi(u)]$ in Equation 3.11 contributes to the intensity in Equation 3.15 (because it gives the imaginary part of $F[H(u)]$). Thus, the term $\exp[i\chi(u)]$ in the CTF [$H(u)$, Equation 3.11] can be replace by $2\sin\chi(u)$. As seen from Equation 3.12, clearly $\sin\chi(u)$ will be a complicated curve which depends on the values of C_S (the lens quality), λ (the accelerating voltage), Δf (the defocus value chosen to form the image) and u (the spatial frequency). For an HRTEM working at a fixed high tension, C_S and λ are fixed. The function $\sin\chi(u)$ depends on the defocus Δf only, with u being determined by the specimen's lattice spacing. Therefore, choosing the optimum defocus for observing particular spatial frequencies is important to fully exploit the capabilities of a TEM in the HRTEM mode. In 1949, Scherzer[112] found that the optimum defocus depends on C_S and λ in the following way:

$$\Delta f_{Sch} = -\left(\frac{4}{3} C_S \lambda\right)^{\frac{1}{2}} \tag{3.16}$$

At this defocus all the beams will have nearly constant phase out to the "first crossover" of the zero axis. This crossover point is defined as the instrumental

resolution limit:

$$r_{Sch} = 0.66 C_S^{\frac{1}{4}} \lambda^{\frac{3}{4}} \tag{3.17}$$

For example, in a JEOL JEM-4000EX HRTEM (C_S = 0.9 mm) operating at 400 kV (λ = 0.0016 nm) used in this thesis, the optimum Scherzer defocus can be calculated using Equation 3.16 and $\Delta f_{Sch} = -44$ nm. Figure 3.8 shows the $\sin\chi(u)$ function of the JEOL JEM-4000EX HRTEM at the optimum Scherzer defocus. The $\sin\chi(u)$ function was calculated using the ctfExplorer software written by Sidorov.[113]

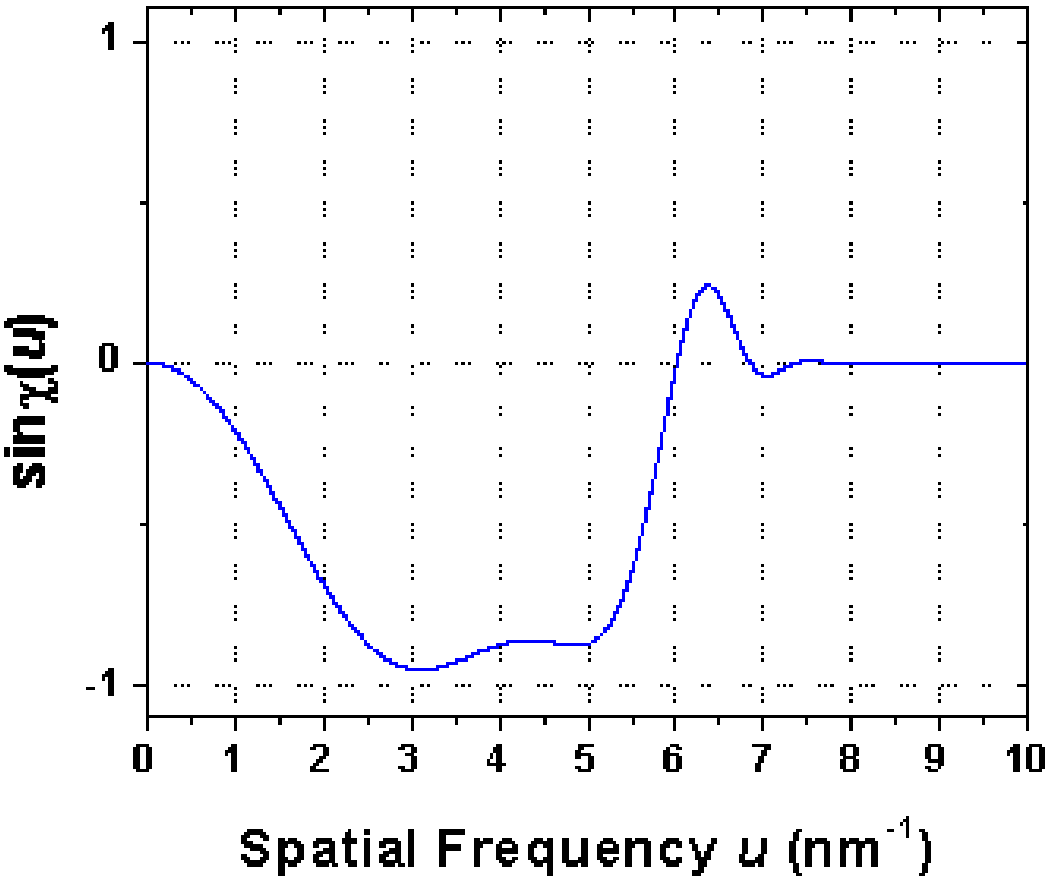


Figure 3.8 The function $\sin\chi(u)$ for a weak phase object for a JEOL JEM-4000EX HRTEM (400 kV and C_S = 0.9 mm) for a Scherzer defocus of -44 nm.

It should be noted that the above discussion is true only when the WPOA holds, and the WPOA is valid only for specimens which are very thin (0.5~2 nm thick). Generally, the signal/noise ratio from such a thin area is very low. Therefore, experimentally WPOA theory does not work well for most inorganic materials. In addition, unlike X-rays, the interaction of electrons is very strong, and such strong interaction indicates that the WPOA theory does not hold in most cases, and dynamical effect must be taken into consideration in a general HRTEM imaging theory. In that case, the multislice method can be used. In the multislice method, the specimen is divided into many thin slices normal to the incident beam and each slice obeys the WPOA.[114] In this thesis, HRTEM was used to characterize the crystalline structures of the axial heterostructured SiNWs and the InN colloidal nanoparticles by measuring the lattice spacings of low-index planes with a careful calibration of the HRTEM magnification. Although the thickness of the semiconductor nanostructures studied in this work is larger than the critical value to use the WPOA, the multislice method is not necessary for the work in this thesis. This is because (i) the crystalline structures of the semiconductor nanostructures are already well known; and (ii) although contrast reversal will occur in the image in very thick specimens, it has no influence on the determination of the lattice spacings.

The TEM specimen of SiNWs was prepared as stated above, and the TEM specimen of the InN colloidal nanoparticles was prepared by transferring the purified suspension containing the harvested nanoparticles to a TEM finder grid with a 20 nm

thick holey carbon film in a nitrogen-protected glove box. HRTEM imaging was made using either a JEOL JEM-4000EX HRTEM (with a point resolution of 0.16 nm, C_S = 0.9 mm) operating at 400 kV (λ = 0.0016 nm) or a JEOL JEM-3000F FEG TEM (with a point resolution of 0.16 nm, C_S = 1.2 mm) operating at 297 kV (λ = 0.0020 nm). In both microscopes, double tilt specimen holders were used, with maximum tilt angles of +/−25° along both axes. HRTEM imaging was carried out by tilting the specimen of interest so that a low-index direction is exactly perpendicular to the electron beam. Images were acquired digitally on a Gatan model 794 (1k × 1k) CCD camera, and the magnification was calibrated accurately using the lattice fringes of single-crystalline Si in the <110> zone axis (the Si{111} lattice spacing of 3.14 Å). Measurements were obtained directly from HRTEM images and also fast Fourier transforms (FFT) obtained from selected areas of lattice images with the program DigitalMicrograph (Gatan, version 3.6.5). The FFT of the HRTEM image provides information about the periodicity of the atomic structure and can be correlated to the EDPs.

3.4 Scanning Transmission Electron Microscopy

In a scanning transmission electron microscopy (STEM), the electrons pass through the specimen, but the electron optics focus the beam into a narrow spot which is scanned over a region of interest. STEM is an important tool for the characterization of nanostructures, providing a range of different imaging modes with the ability to

provide information on elemental composition concurrently.

In a typical STEM, electrons are accelerated from a source and focused into a point on the specimen by a set of condenser lenses and an objective lens. An objective aperture limits the maximum angle of illumination included in the incident probe, which is scanned across the sample by a set of scan coils. The output of a variety of possible detectors can then be used to form an image (Figure 3.9). The usual detectors include a BF detector that intercepts the transmitted beam and an annular dark-field (ADF) detector that surrounds the transmitted beam to collect scattered electrons. Another annular detector which is placed around the ADF and picks up the electrons scattered out to even higher angles is used to form the high-angle annular dark-field (HAADF) images where Bragg scattering is usually negligible. Such HAADF image is highly sensitive to variations in the atomic number of atoms in the sample (*Z*-contrast images).[115]

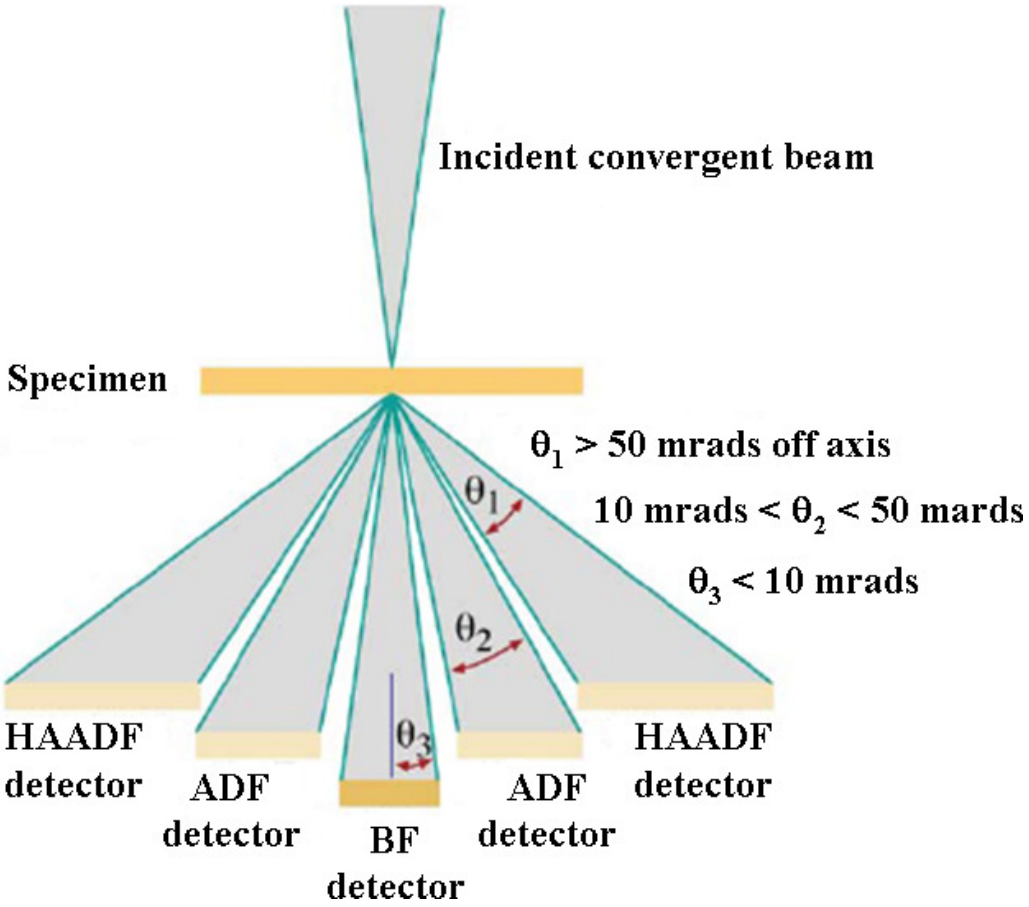


Figure 3.9 Schematic showing the STEM image formation (redrawn from Reference 107).

In this thesis, STEM imaging was carried out using either a JEOL JEM-2200MCO TEM/STEM with two aberration correctors operating at 200 kV or a JEOL JEM-3000F TEM/STEM operating at 297 kV. In both instruments, the alignment for STEM was done using a Ronchigram to correct the low order aberrations.[116] In the JEOL 2200 TEM/STEM, the higher order aberrations were further corrected by the automated aberration correction software.

3.5 Energy Dispersive X-ray Spectroscopy

Combining within a single instrument the complementary capabilities of imaging, diffraction and spectroscopy, all at exceptionally high spatial resolution, TEM provides a wealth of morphological, structural and compositional information. Compositional information of the nanostructures can be obtained using energy dispersive X-ray spectroscopy (EDX).

The fundamental principle of EDX is based on the unique spectral lines of each element in the periodic table. An atom within the sample contains ground state electrons situated in concentric shells around the nucleus. When a high-energy electron beam ejects a core electron in the inner shell of the atom, an electron hole within the atom's electronic structure is formed. Another electron at an outer and higher energy shell fills the hole and releases the excess amount of energy in the form of X-rays. The release of X-rays creates spectral lines characteristic of the element and the X-ray emission data can be used to characterize the chemical composition of the examined region of the sample. If an electron is ejected from the atom's K shell and this is filled by an electron from the L shell, a K_α X-ray is emitted; if it is filled by an electron from the M shell, a K_β X-ray is emitted. Similarly, if an electron is ejected from the atom's L shell and an electron fills it from the M shell, an L_α X-ray is emitted; if it is filled from the N shell, an L_β X-ray is emitted.[117]

An energy dispersive X-ray spectrometer consists of a solid state detector, X-ray processing circuits and data management system. The EDX characterization process generally includes:

(i) X-ray generation: an electron beam passes through the specimen in an interaction region, and generates related X-rays;

(ii) X-ray collection: a collimator accumulates X-rays and produces a spectrum;

(iii) Spectrum analysis: analytical software quantifies the spectrum.

3.5.1 Qualitative Analysis

Qualitative EDX analysis gives a good idea of which elements in the specimen are detectable. The first step in qualitative analysis is to acquire a spectrum across the complete X-ray energy range, then start at the high-energy end of the spectrum and identify all the major peaks and any associated family lines and artefacts by using the computer-generated X-ray line marker on the multi channel analyser screen or by consulting an appropriate source. Therefore, to identify the elements in the specimen, the artefacts introduced by the EDX system have to be understood. For example, illumination system artefacts arise when stray electrons around the aperture and high-energy X-rays generated at the aperture can interact with and generate X-rays from areas of the specimen not illuminated by the beam. An instrument can be checked for illumination system artefacts by carrying out a hole count, positioning the incident

beam in a hole in the specimen and checking if any specimen characteristic X-rays are generated. In addition, extra signals other than emitted characteristic X-rays (*e.g.*, back-scattered electrons and transmitted electrons) can generate X-rays from another part of specimen, specimen holder or pole pieces, giving rise to the specimen/specimen region artefacts. The EDX detector (usually made from single crystal of silicon) can also introduce some artefacts. For example, if the incoming photon of energy fluoresces a Si K_α X-ray (energy 1.74 keV) which escapes from the intrinsic region of the detector, Si "escape peaks" appear in the spectrum 1.74 keV below the true characteristic peak position. The internal-fluorescence peak is a characteristic peak from the Si in the detector dead layer. Incoming photons fluoresce atoms in the dead layer and the resulting Si K_α X-ray enters the intrinsic region of the detector, so the detector registers a small Si K_α peak in the spectrum.

3.5.2 Quantitative Analysis

The basic quantitative equation for EDX has been developed by Castaing,[118] who suggested that the concentration C_i of an element i in the specimen relative to a known standard composition $C_{(i)}$ can be approximated as

$$\frac{C_i}{C_{(i)}} = K \frac{I_i}{I_{(i)}} \tag{3.18}$$

where I_i is the measured intensity emerging from the specimen, $I_{(i)}$ is the measured intensity energy from the standard, and K is a sensitivity factor that takes into account the difference between the generated and measured X-ray intensities for both the

standard and the unknown specimen. The contributions to *K* come from three effects: (i) the atomic number *Z*; (ii) the absorption of X-rays within the specimen *A*; and (iii) the fluorescence of X-rays within the specimen *F*.[107]

Using a simplification of Castaing's original ratio equation, Cliff and Lorimer[119] showed that the quantification was possible by using the ratio of the intensities gathered from two elements A and B in the specimen simultaneously in the EDX. The weight percents of each element C_A and C_B can be related to the measured intensities by the so-called Cliff-Lorimer equation:

$$\frac{C_A}{C_B} = k_{AB} \frac{I_A}{I_B} \tag{3.19}$$

where I_A and I_B are the measured intensities of elements A and B, respectively, and the term k_{AB} is often termed the Cliff-Lorimer factor, which is actually not a constant and related to the atomic number correction factor (*Z*) in Castaing's original ratio equation (the specimen is assumed to be thin enough so that any absorption or fluorescence can be ignored).

In this thesis, EDX was used to qualitatively check the chemical elements in the InN colloidal nanoparticles, in order to confirm that the nanoparticle grown from solution-phase reactions is InN and not other materials. Quantitative EDX analysis was not carried out in this work. The chemical elements in the harvested colloidal nanoparticles were examined using an Oxford Instruments EDX spectrometer in the JEOL JEM-3000F FEG TEM with a super atmospheric thin window detector. A low

background beryllium double tilt specimen holder (+/−25° tilt angles) was used for EDX measurements, and the EDX spectra were obtained under the STEM mode using a fine electron beam spot of 0.5 nm and an acquiring time of 120 s.

3.6 Scanning Electron Microscopy

Scanning electron microscopy (SEM) is a type of electron microscopy that images the sample surface by scanning it with a high-energy beam of electrons in a raster scan pattern. The electrons interact with the atoms that make up the sample producing signals that contain information about the sample's microstructural properties such as the surface morphology.

In a typical SEM, the electron gun produces a source of accelerated electrons. Electron lenses are used to reduce the diameter of this source of electrons and place a small, focused electron beam on the specimen, as shown schematically in Figure 3.10. The deflection system is to scan the beam along a line and then displace the line position for the next scan so that a rectangular raster is generated on both the specimen and the viewing screen. The interactions of the electron beam with the specimen surfaces generate several types of signals, including secondary electrons, back-scattered electron, characteristic X-rays, light (cathode-luminescence), specimen current and transmitted electron. The most common or standard detection mode is secondary electron imaging: when the non-energetic secondary electrons strike the

scintillator material, the light produced is converted to an amplified electrical signal by the photomultiplier tube, the variation of which provides the intensity changes as an image.[120]

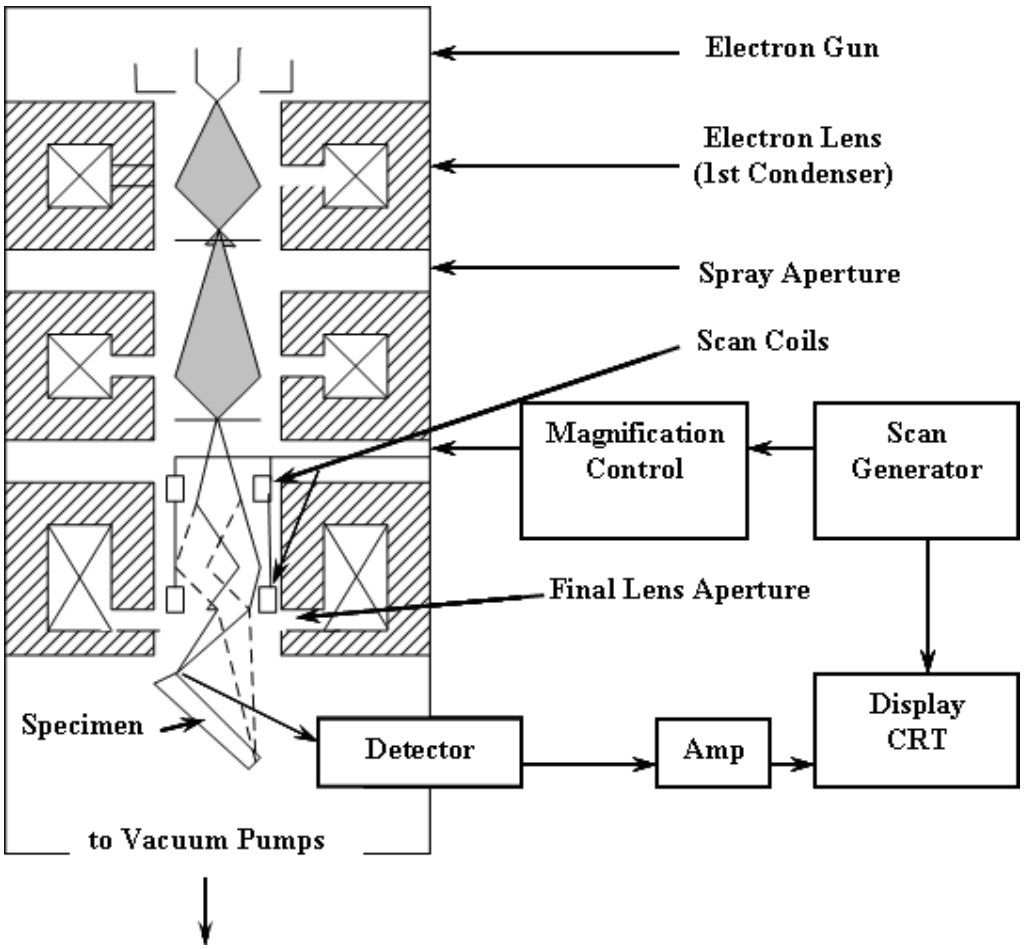


Figure 3.10 Schematic drawing of the electron column, deflection system, and electron detectors in a typical SEM (redrawn from Reference 120).

SEM is widely used in revealing the surface properties of nanoscale materials, as it can produce very high resolution images of a sample surface. In addition, SEM micrographs have a large depth of field yielding a characteristic 3D appearance useful for understanding the surface structure of a sample. Therefore, in this thesis, as a

supplementary tool, SEM was employed to study the surface morphology of the axial heterostructured SiNWs, since TEM characterizations only provide 2D projection images. Assisted by Dr Gareth Hughes, SEM imaging was carried out using a Zeiss NVision40 SEM at the accelerating voltages in the range of 0.5~2 kV.

3.7 Raman Spectroscopy

Raman spectroscopy plays an increasingly important role in the non-destructive characterization of nanostructures. Phonon frequencies and scattering intensities determined by Raman spectroscopy can lead to conclusions concerning microscopic parameters such as bonding and structure as well as deviations from the ideal crystalline counterpart.

Raman scattering is named after Indian physicist C. V. Raman who discovered it in 1928, though predictions had been made as far back as 1922.[121] When a beam of light is impinged upon a sample, photons are absorbed by the material and scattered. The vast majorities of these scattered photons have exactly the same wavelength as the incident photons and are known as Rayleigh scatter, but the Raman effect is the inelastic scattering of light. It occurs when light impinges upon a molecule, interacts with the electron cloud of the bonds of that molecule, and raises it to a virtual energy state. For the spontaneous Raman effect, the molecule will relax into a vibrational excited state, which generates Stokes Raman scattering. If the molecule was already

in an elevated vibration energy state, the Raman scattering is then called anti-Stokes Raman scattering.[122] Figure 3.11 shows a diagram of Rayleigh scattering, Stokes Raman scattering, and anti-Stokes Raman scattering. A molecular polarizability change or amount of deformation of the electron cloud, with respect to the vibrational coordinate is required for the molecule to exhibit the Raman effect. The amount of the polarizability change will determine the Raman scattering intensity, whereas the Raman shift is equal to the vibrational level that is involved.

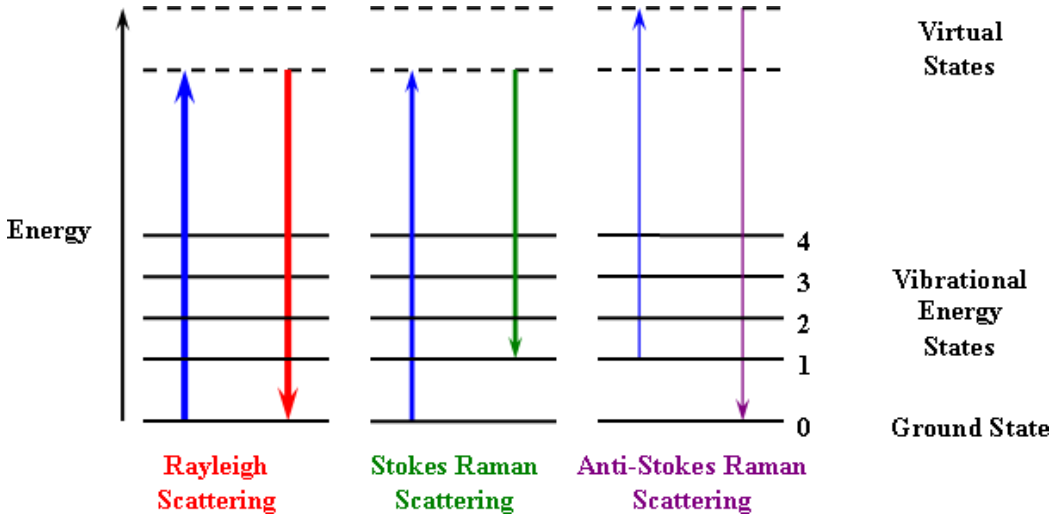


Figure 3.11 Energy-level diagrams of Rayleigh scattering, Stokes Raman scattering, and anti-Stokes Raman scattering. The line thickness is roughly proportional to the signal strength from the different transitions.

A typical Raman spectrometer is made up of three basic parts: the laser, the collection device, and the spectrograph. A laser is used to excite Raman spectra because it gives a coherent beam of monochromatic light. Lasers used for Raman spectroscopy must exhibit good wavelength stability and low background emission. A collection device collects the scattered photons, filters out the Rayleigh scatter and any background

signal and sends the Raman scatter to the spectrograph. When Raman scattered photons enter the spectrograph, they are passed through a transmission grating to separate them by wavelength of the Raman signal at each wavelength and passed to a detector, which records the intensity of the Raman signal at each wavelength. This data is plotted as the Raman spectrum.

Raman spectroscopy is a powerful, non-destructive characterization tool that can be used to study the structure of individual nanostructures. In this thesis, Raman spectroscopy was used as a supplementary tool to characterize the crystalline structure of SiNWs. The Raman spectra were measured using a JY Horiba Labram Aramis imaging confocal Raman microscope and a coherent 532 nm laser. The beam was focused with a 100× objective to a spot with diameter ~1 μm.

3.8 Chapter Summary

The basic principles and working mechanisms of the characterization tools used in this thesis to characterize the microstructural properties of 1D axially doped SiNWs and 0D InN colloidal nanoparticles, including TEM, HRTEM, STEM, EDX, SEM and Raman spectroscopy, are introduced in this chapter.

Chapter 4

Crystalline Structure and Growth Direction of Silicon Nanowires

4.1 Introduction

Silicon nanowires (SiNWs) are potential candidate materials for a wide range of novel electronic, optical and chemical/biological devices.[12-16] In developing these applications, it is essential to control the physical properties of SiNWs, which depend strongly on their growth direction, crystalline structure and defects.[18] For example, high phase purity of SiNWs is essential for their functional device applications, because their physical properties are highly sensitive to the crystal structures. Bulk Si has a stable diamond cubic crystalline structure under ambient conditions; however, the crystalline structure of nanowires may be quite different from that of the bulk.[8] A uniform nanowire growth direction is required for hierarchical assembly of functional nanoscale electronic and photonic structures, because nanowire kinks (where

nanowire changes its growth direction) are undesirable for device processing. For example, kinks cause problems when fluidic alignment methods[123,124] are used to align the nanowires between two electrodes.

Therefore, investigation of these fundamental microstructural properties is important to achieve SiNWs with desirable properties for reliable device applications. The purpose of this chapter is (i) to check the uniformities of the crystalline structure and the growth direction of the axial heterostructured SiNWs grown on an oxide-removed Si{111} substrate; and (ii) to understand the formation mechanisms of the kink morphology and the hexagonal (wurtzite) crystalline structures in SiNWs.

4.2 Crystalline Structure

4.2.1 Background of Research

The stable crystalline form of bulk Si under ambient conditions is a diamond cubic structure (Si I), while under different pressures, diamond Si can transform into various metastable high pressure phases, *e.g.*, a hexagonal crystalline structure (sometimes referred to as wurtzite Si, Si IV) under ~8 GPa.[125] Both diamond cubic and hexagonal (wurtzite) Si have a tetrahedral coordination, but the stacking of the tetrahedra is different. A comparison between the two crystal geometries is presented schematically in Figure 4.1. Here the stacking of atoms in the diamond cubic structure

along the [111] direction is compared to the [0001] of the hexagonal (wurtzite) structure. The stacking in the diamond cubic structure is in the ···ABCABC··· sequence, while is only ···ABABAB··· in the hexagonal (wurtzite) structure.

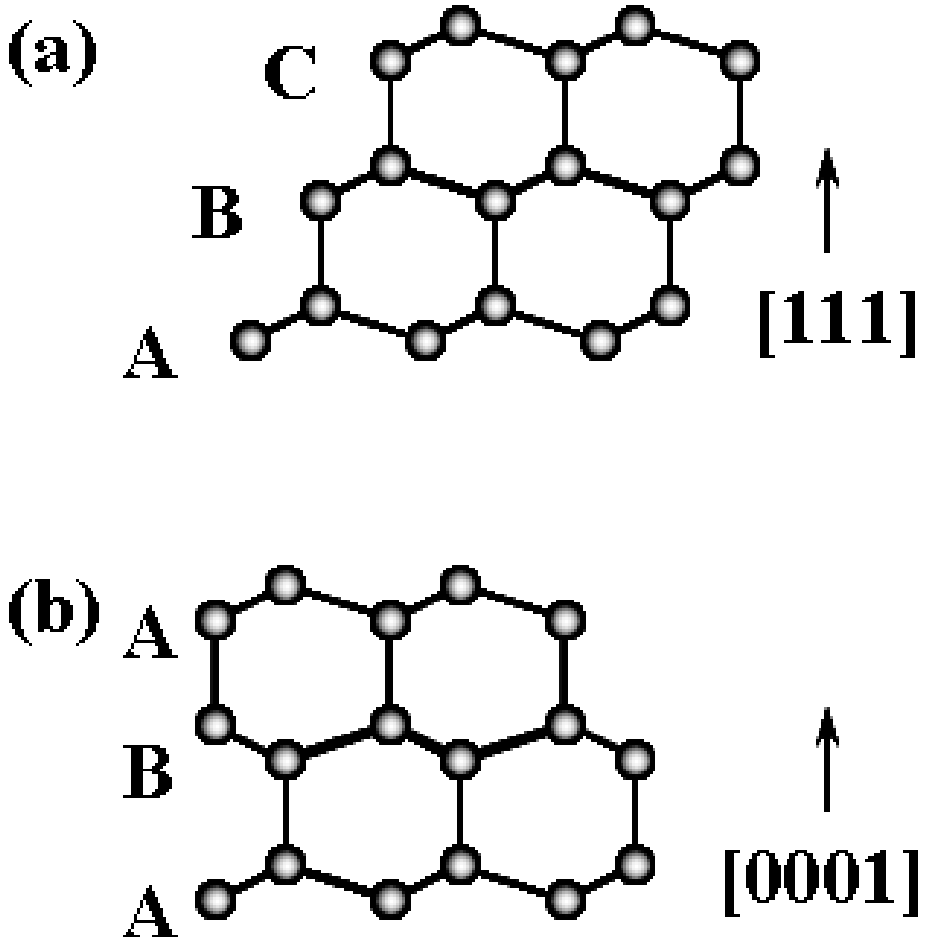


Figure 4.1 Comparison of the stacking of the tetrahedra in (a) the diamond cubic (<110> projected) and (b) the hexagonal (<$01\bar{1}0$> projected) structures.

Reports of stable hexagonal (wurtzite) Si under ambient conditions are scarce in the literature.[126,127,128] Two slightly different Si hexagonal (wurtzite) structures have been reported: Si IV_A ($a = b = 3.80$ Å, $c = 6.27$ Å, $c/a = 1.65$)[129] and Si IV_B ($a = b =$

4.04 Å, c = 6.60 Å, c/a = 1.63).[130] Despite the rareness of hexagonal (wurtzite) Si, recently the observation of hexagonal (wurtzite) SiNWs has been reported. For example, Fontcuberta i Morral *et al.*[131] demonstrated the formation of hexagonal (wurtzite) SiNWs by a standard CVD approach on oxidized Si substrates. Arbiol *et al.*[132] reported the switching of the Si structure from diamond to hexagonal (wurtzite) along the wire growth direction in SiNWs synthesized via a Cu-catalysed vapour-solid-solid mechanism. However, in both studies, SiNWs were grown on oxidized substrates with an oxide thickness of 1 μm and the crystallographic alignment with the substrate was lost. Also, the key experimental evidence in identifying crystal structures, electron diffraction patterns (EDPs), was missing.

In this thesis, axial heterostructured SiNWs with varying doping were not grown on oxidized Si substrates, but an oxide-removed Si{111} substrate using a VLS approach. Considering the excellent symmetry and lattice match between the wire and substrate crystal structures, it is expected that the VLS-grown SiNWs on an oxide-removed Si{111} substrate should have the diamond cubic crystalline structure and grow epitaxially in the <111> direction. However, it is not known if other crystalline structures can be formed in the SiNWs synthesized in this work. Therefore, it is necessary to check the phase purity of the harvested axial heterostructured SiNWs. Here HRTEM (with calibrated magnification) and Raman spectroscopy are powerful tools to study the crystalline structures of individual SiNWs. A low-density TEM specimen (the synthesized SiNWs are well separated from each other) was prepared

by dispersing the SiNWs on the holey carbon film of a TEM finder grid. A TEM finder grid was used because it enabled the structural characterization of the same SiNW using both HRTEM and Raman spectroscopy, offering direct correlation of the crystalline structures determined by these two independent techniques.

4.2.2 Results and Discussion

In this thesis, the crystalline structures of 144 axial heterostructured SiNWs were characterized using HRTEM. Around 98% of the SiNWs exhibit the expected diamond cubic structure. For example, Figure 4.2 shows the HRTEM image of a VLS-grown axial heterostructured SiNW. The Fourier transform of the HRTEM image and the TEM image of the same SiNW taken at low magnification are shown as insets in Figure 4.2. It is seen that the SiNW is single-crystalline. The angles between the lines joining FFT spots to spot 000 were measured and the ratios of spot spacings were examined. Such values were compared with the standard EDPs for single crystals in various beam directions.[107] It is found that the spots in FFT exhibit a pattern which is characteristic of an fcc material in the <110> zone axis, because the angle between lines joining the $(\bar{1}11)$ and (200) points to spot 000 in FFT is measured to be 54.7° $\pm$ 0.2°, while the angle between those of the $(\bar{1}11)$ and $(\bar{1}\bar{1}1)$ points is 70.8° $\pm$ 0.2°. The (200) and $(\bar{1}11)$ spot spacings were measured and the ratio of these two measured spacings is 1.16. Such pattern matches well with the standard EDPs for an fcc crystal in the <110> orientation. Therefore, the SiNW has a diamond cubic

structure with the Si{111} planes having a spacing of 3.14 Å (as shown in Figure 4.2).

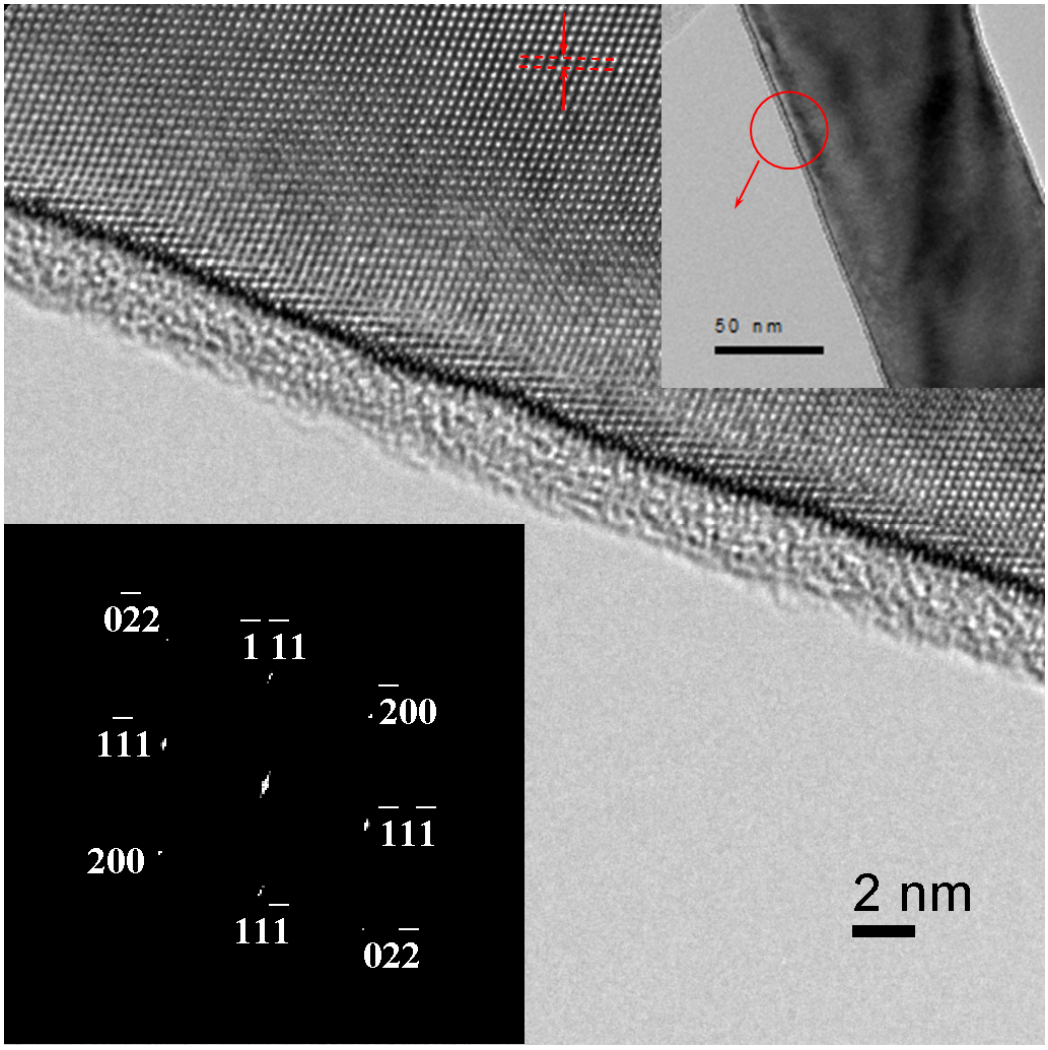


Figure 4.2 HRTEM of a VLS-grown axial heterostructured SiNW, insets: the Fourier transform of the image and the TEM image of the same SiNW taken at low magnification.

The rest (~2%) of the synthesized axial heterostructured SiNWs exhibit the metastable hexagonal (wurtzite) phase. Figure 4.3(a) shows an overview image of a SiNW with a radial width of ~100 nm. Numbers 'I~II' in Figure 4.3(a) are assigned to the different positions in the wire. The HRTEM images and their corresponding

Fourier transforms of regions I and II are shown in Figure 4.3(b) and (c), respectively. It is seen that the Fourier transforms show patterns having a six-fold symmetry. In the case of Si, such pattern could correspond to the diamond cubic structure (stable, Si I, $a = 5.43$ Å)/the body-centred cubic (bcc) structure (metastable, Si III, $a = 6.636$ Å) with the <111> zone axis, or the hexagonal (wurtzite) structure (metastable, Si IV) with the <0001> zone axis. To identify the crystalline structure of the SiNW in Figure 4.3(a), the lattice spacing must be examined with calibrated magnification. This is because the detailed projected atomic arrangements of these crystalline structures in the <111> or <0001> zone axis only differ in the lattice distance.

The average lattice spacing was determined by obtaining 10 line profiles using the DigitalMicrograph (Gatan, version 3.6.5) software across 10 successive lattice planes and by averaging over these periods. For accurate measurement, the diamond cubic structured SiNW on the same TEM grid was used as a standard reference for the magnification calibration. With the assistance of the TEM finder grid, the previously examined diamond cubic SiNW was found and tilted so that the <110> zone axis was parallel to the incident beam. An HRTEM image of the diamond cubic SiNW was taken along the <110> direction and the Si{111} plane has a spacing of 3.14 Å. Such spacing was used to calibrate the magnification of the HRTEM, and the calibrated magnification was then used to measure the interplanar distances of the SiNW in Figure 4.3 at the same magnification value (displayed on the microscope), at which

the calibration was carried out. This produced an overall spacing of 3.28 Å with a standard deviation being 0.02 Å.

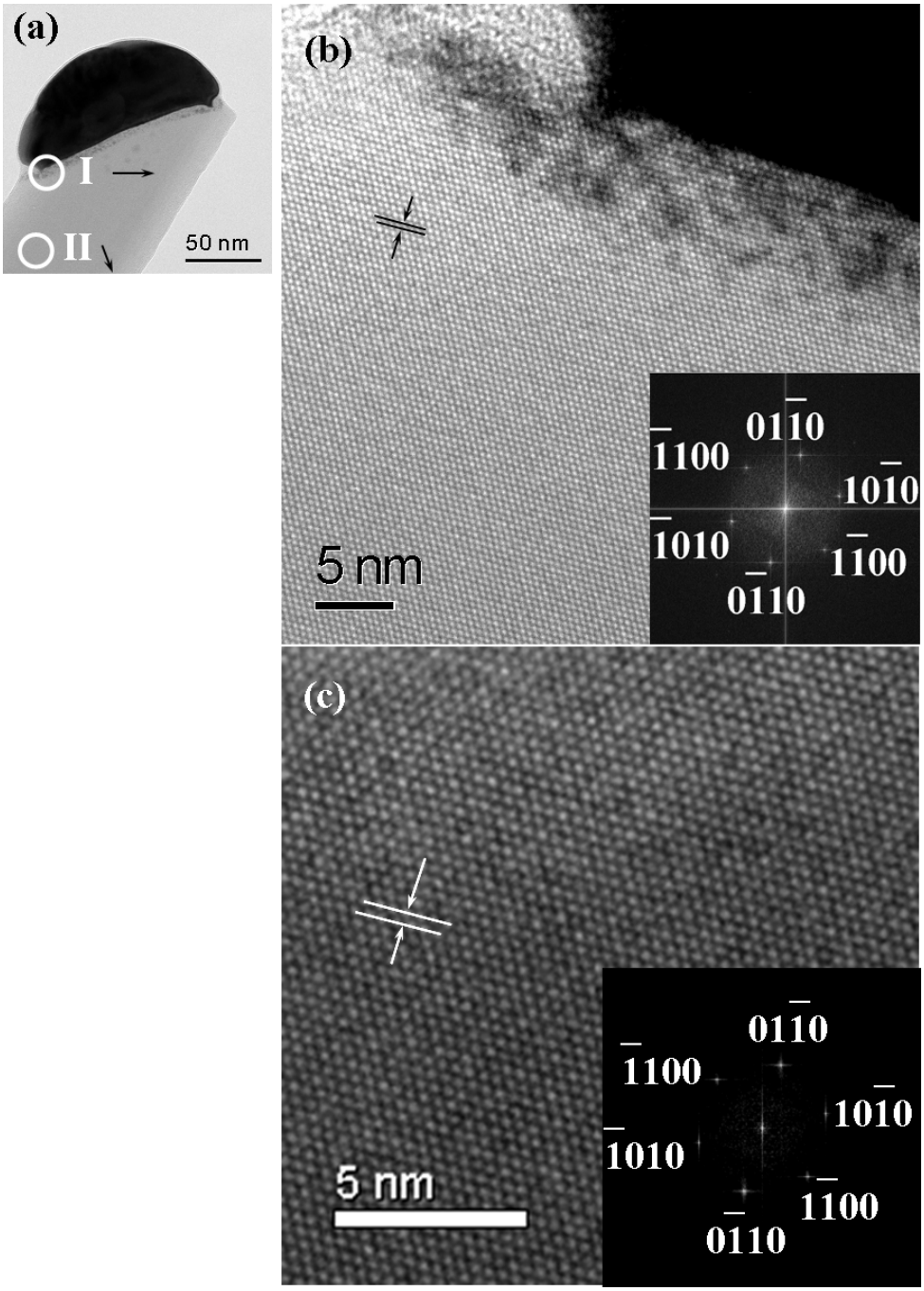


Figure 4.3 (a) TEM image of a SiNW, numbers 'I' and 'II' are assigned to label different positions; (b) HRTEM image of part I in (a); and (c) HRTEM image of part II in (a). Insets in (b) and (c) are their corresponding Fourier transforms.

Table 4.1 compares the lattice distances for the diamond cubic/bcc Si in the <111> zone axis and the hexagonal (wurtzite) Si in the <0001> zone axis with the measured value. It is seen that the measured interplanar spacing is in good agreement with the interplanar spacing between hexagonal (type A) Si $IV_A\{10\bar{1}0\}$ planes.

Table 4.1 Comparison of the FFT patterns and the lattice spacings with the measured values.

Crystalline Structure	**diamond cubic (Si I)**	**bcc (Si III)**	**hexagonal (Si IV)**
FFT Pattern	6-fold symmetry		
Zone Axis	<111>		<0001>
Reflections of the 6 spots around the central spot	{220}	{110}	$\{10\bar{1}0\}$
Lattice Spacing	$d\{220\}_{\text{Si I}} = 1.92$ Å	$d\{110\}_{\text{Si III}} = 4.69$ Å	**type A (Si IV_A):** $d\{10\bar{1}0\}_{\text{Si IV}} = 3.29$ Å **type B (Si IV_B):** $d\{10\bar{1}0\}_{\text{Si IV}} = 3.50$ Å
Measured Lattice Spacing	3.28 ± 0.02 Å		

The EDPs of the same SiNW in Figure 4.3 were further examined using a calibrated camera length. Here a standard Au film specimen (diffraction ring of Au{111} planes with a spacing of 2.36 Å) was used as a reference. With the assistance of the TEM finder grid, the EDPs of a diamond cubic SiNW (previously examined) and the same SiNW in Figure 4.3 were obtained at the same camera length value (displayed on the

microscope), at which the calibration was carried out. As shown in Figure 4.4, the EDPs of the diamond cubic SiNW show primary diffractions outside the Au reference diffraction ring of Au{111} planes [Figure 4.4(b)], whereas the primary reflections for the SiNW in Figure 4.3 fall inside the Au reference [Figure 4.4(c)] [the diffraction ring is only shown schematically in Figure 4.4(b) and (c) for clarity].

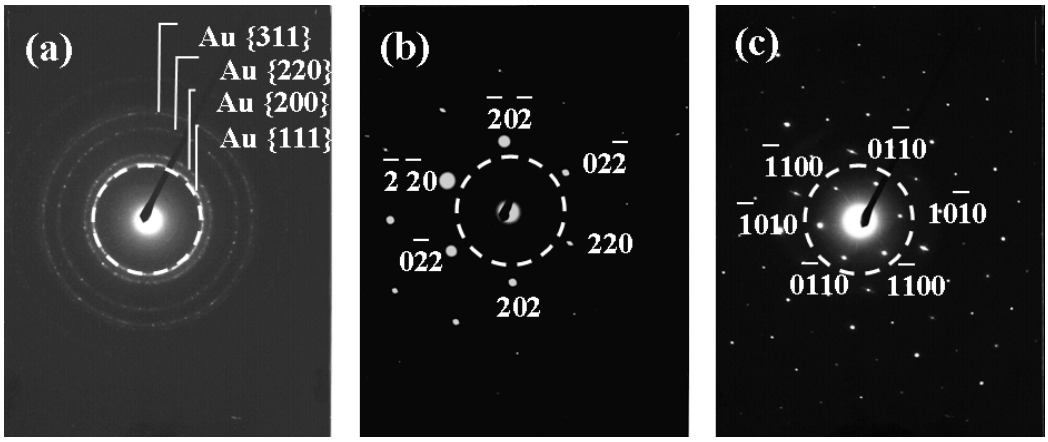


Figure 4.4 (a) Diffraction rings from the Au film as a reference; (b) EDPs of a diamond cubic SiNW with the reference of Au{111} schematically highlighted; and (c) EDPs of the same SiNW in Figure 4.3 with the reference of Au{111} schematically highlighted.

To further confirm the hexagonal (wurtzite) crystalline structure, the same SiNW in Figure 4.3 was tilted so that other zone axes were parallel to the incident beam. Figure 4.5(a) and (b) show the indexed SAED patterns for the same SiNW in Figure 4.3(a). To index the EDPs in Figure 4.5, the angles between lines joining the electron diffraction spots to spot 000 were measured and the ratios of spot spacings were examined. Take Figure 4.5(a) as an example, the angle between the $(1\bar{1}01)$ and $(2\bar{1}\bar{1}0)$ spots is measured to be 40.2° $\pm$ 0.3°, while the angle between the $(1\bar{1}01)$ and

$(0\bar{1}12)$ spots is 49.8° ± 0.3°. The ratio of the measured $(0\bar{1}12)$ and $(1\bar{1}01)$ spot spacings is 1.28. Such patterns match well with the EDPs for the type A hexagonal Si (Si IV_A) in the $[0\bar{1}\bar{1}1]$ zone axis. Following the same method, the EDPs in Figure 4.5(b) were indexed to be the Si IV_A in the $[\bar{1}2\bar{1}3]$ orientation. These experiments confirm that the SiNW in Figure 4.3 has a hexagonal type A structure (Si IV_A).

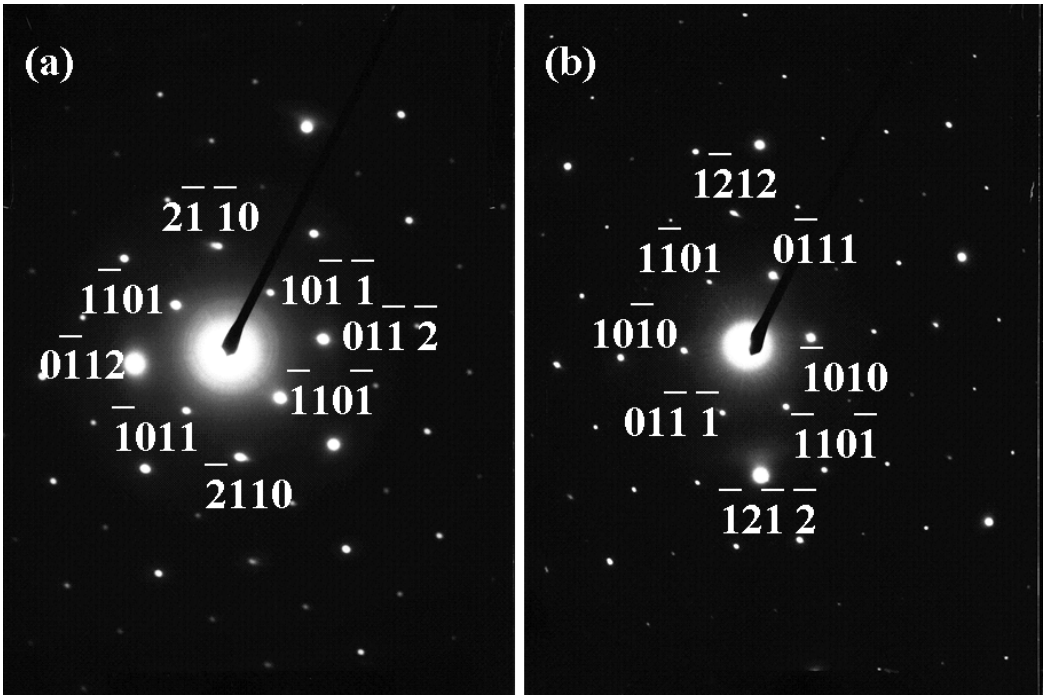


Figure 4.5 Indexed SAED patterns for the same SiNW in Figure 4.3(a) for the (a) $[0\bar{1}\bar{1}1]$ and (b) $[\bar{1}2\bar{1}3]$ beam direction.

Aside from the hexagonal type A (Si IV_A) nanowires, hexagonal type B (Si IV_B) nanowires were also observed in the SiNWs synthesized. Figure 4.6(a) shows an overview image of a ~150° kinked SiNW. Numbers 'I~III' in Figure 4.6(a) are assigned to the different positions of the kink. The corresponding HRTEM images of regions I~III and their Fourier transforms are shown in Figure 4.6(b)~(d), respectively.

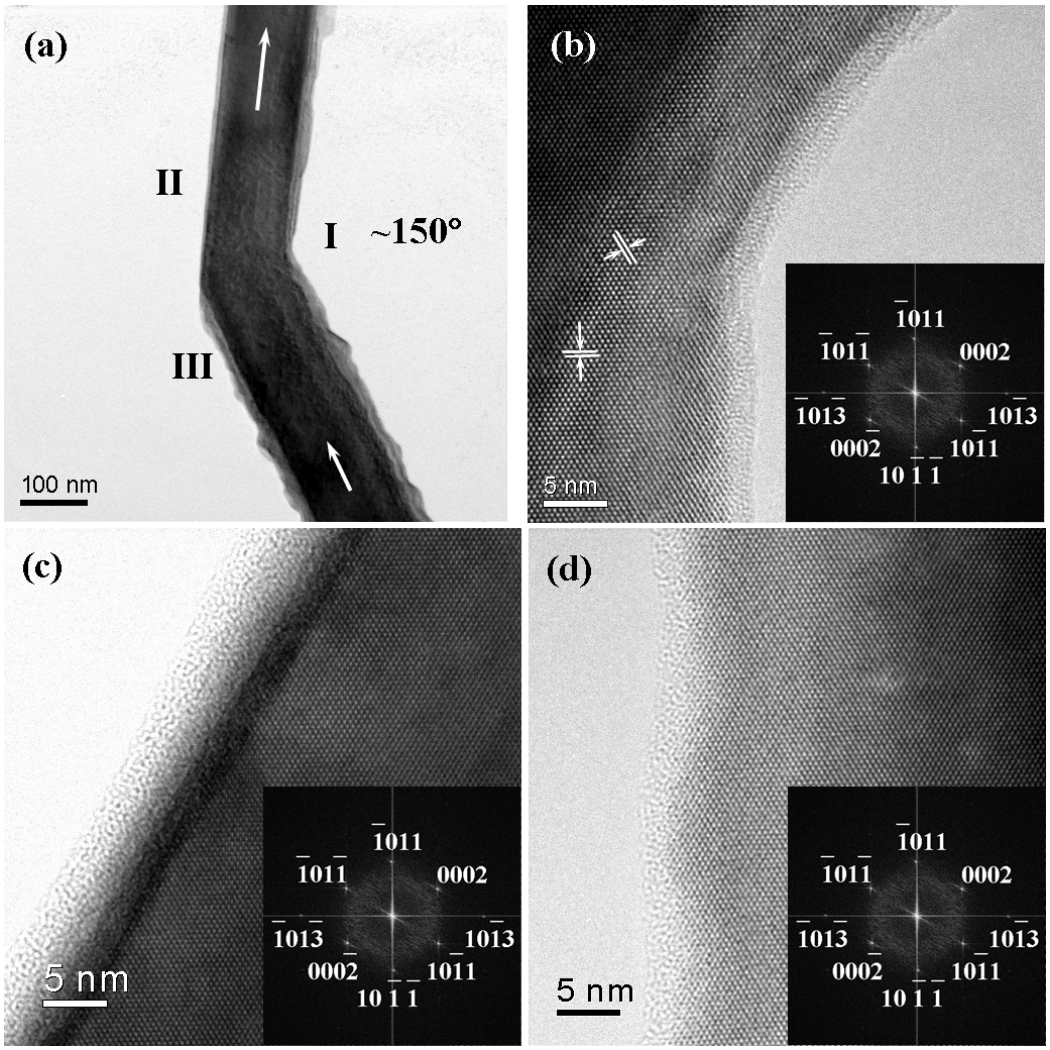


Figure 4.6 (a) TEM image of a ~150° kinked SiNW, numbers 'I~III' are assigned to label different positions; HRTEM image of (b) part I, (c) part II and (d) part III in (a), insets in (b)~(d) are their corresponding Fourier transforms.

The average lattice spacing was determined by obtaining 10 line profiles using the DigitalMicrograph (Gatan, version 3.6.5) software across 10 successive lattice planes and by averaging over these periods. The magnification of the HRTEM was calibrated following the same procedure stated above. The angle between the planes marked as $\{\bar{1}0\bar{1}1\}$ and $\{\bar{1}011\}$ is 56.1° ± 0.3°, while the angle between $\{\bar{1}011\}$ and {0002} planes is 61.8° ± 0.3°. The measured interplanar distances for the $\{\bar{1}011\}$ and {0002}

planes are 3.09 ± 0.02 and 3.31 ± 0.02 Å, respectively. The measured interplanar distances and angles are in good agreement with those calculated for a type B (Si IV_B) hexagonal crystalline structure (see Table 4.2).

Table 4.2 Comparison of the measured interplanar angles and distances with the calculated values. The calculated interplanar distances and angles were obtained using the equations:[133]

$$g_{hkil}^2 = \frac{1}{d_{hkil}^2} = \frac{4}{3a^2}(h^2 + hk + k^2) + \frac{l^2}{c^2},\ i = -(h+k)$$

$$\cos\varphi = \frac{\frac{4}{3a^2}[hh' + kk' + 0.5(hk' + kh')] + \frac{ll'}{c^2}}{g_{hkil}\, g_{h'k'i'l'}},\ i' = -(h'+k')$$

	Si IV_B: $a = b = 4.04$ Å, $c = 6.60$ Å	**Si IV_A: $a = b = 3.80$ Å, $c = 6.27$ Å**	
	calculated	**calculated**	**measured**
angle between the $\{\bar{1}01\bar{1}\}$ and $\{\bar{1}011\}$ planes	55.9°	55.3	56.1° ± 0.3°
angle between the $\{\bar{1}011\}$ and $\{0002\}$ planes	62.1	62.3	61.8° ± 0.3°
$d\{\bar{1}011\}$ (Å)	3.09	2.91	3.09 ± 0.02
$d\{0002\}$ (Å)	3.30	3.14	3.31 ± 0.02

The same SiNW in Figure 4.6 was also tilted so that other zone axes were parallel to the incident beam. Figure 4.7(a) and (b) show the indexed SAED patterns for the same SiNW in Figure 4.6 for the $[\bar{2}4\bar{2}3]$ and $[\bar{1}2\bar{1}3]$ beam directions, respectively. The EDPs in Figure 4.7 were indexed by examining the ratios of the spot spacings and the angles between the plane normals of the patterns, following the method stated above.

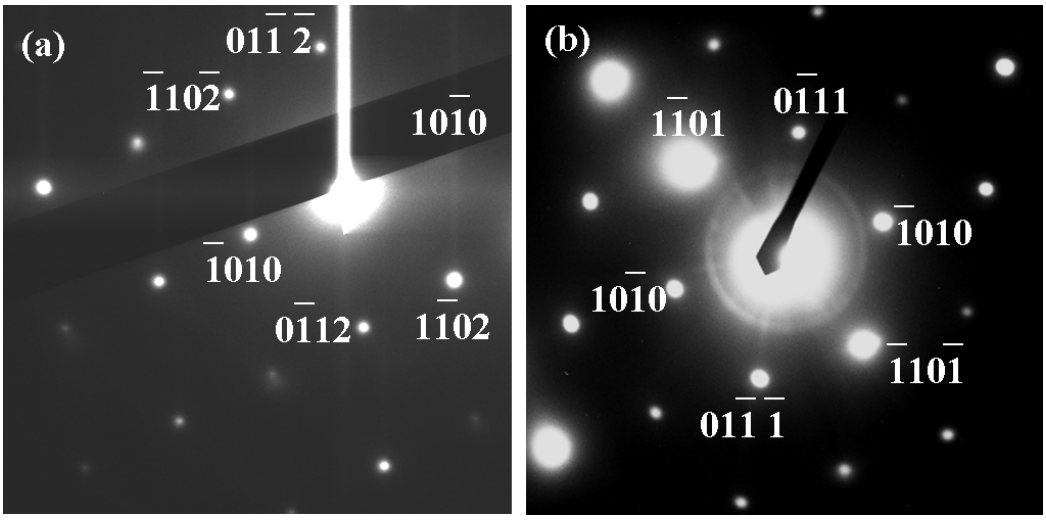


Figure 4.7 Indexed SAED patterns for the same kinked SiNW in Figure 4.6 for the (a) $[\bar{2}4\bar{2}3]$ and (b) $[\bar{1}2\bar{1}3]$ beam direction.

Raman spectroscopy was also used to examine the crystalline structures of the same SiNWs observed in the TEM characterization, in order to confirm the formation of the hexagonal (wurtzite) structured SiNWs. The density of the SiNWs on the TEM finder grid is low enough, so that Raman spectrum of single SiNW can be obtained. Although the magnification of the optical microscope on the Raman spectroscopy is low, the same SiNWs that have been examined using HRTEM can still be identified by observing the nanowire position on the TEM finder grid and the morphology of the SiNWs (such as the ~150° kinked SiNW in Figure 4.6).

A comparison of Raman spectra between the diamond cubic and hexagonal (wurtzite) SiNWs is shown in Figure 4.8, with the bulk diamond Si as a reference. As seen from Figure 4.8, the first order Raman peak of the bulk diamond Si is at 519.5 ± 1.0 cm^{-1} with a FWHM of 4.2 ± 0.6 cm^{-1}. These are in good agreement with the previously

reported values of ~522 cm^{-1} with a line width of ~3.5 cm^{-1}.[134] When acquiring the Raman spectra of SiNWs, one should note that the laser heating effect on nanowires can cause the Raman band downshifting,[135] which results in the misinterpretation of Raman spectra. Therefore, to avoid the heating by the excitation laser, the laser power was kept at a relatively low value, so that the Raman peak of the diamond cubic SiNW was also around 520 cm^{-1} (Figure 4.8), suggesting that the samples were at room temperature and the laser heating effect had not yet occurred. At this low laser power, the Raman spectrum of the hexagonal (wurtzite) structured SiNW is compared with the Raman spectra of the diamond cubic Si bulk and SiNW. No evident difference in Raman spectra between the type A and type B hexagonal (wurtzite) SiNWs was observed in this thesis. The hexagonal (wurtzite) SiNW exhibits a peak centred at 507 cm^{-1}, as well as a broad band between 223 and 288 cm^{-1}, in excellent agreement with the predicted transverse optical (TO) and the 2-fold transverse acoustical (TA) modes of hexagonal (wurtzite) Si.[136] Thus the Raman analysis confirms independently the existence of hexagonal (wurtzite) SiNWs synthesized in this work.

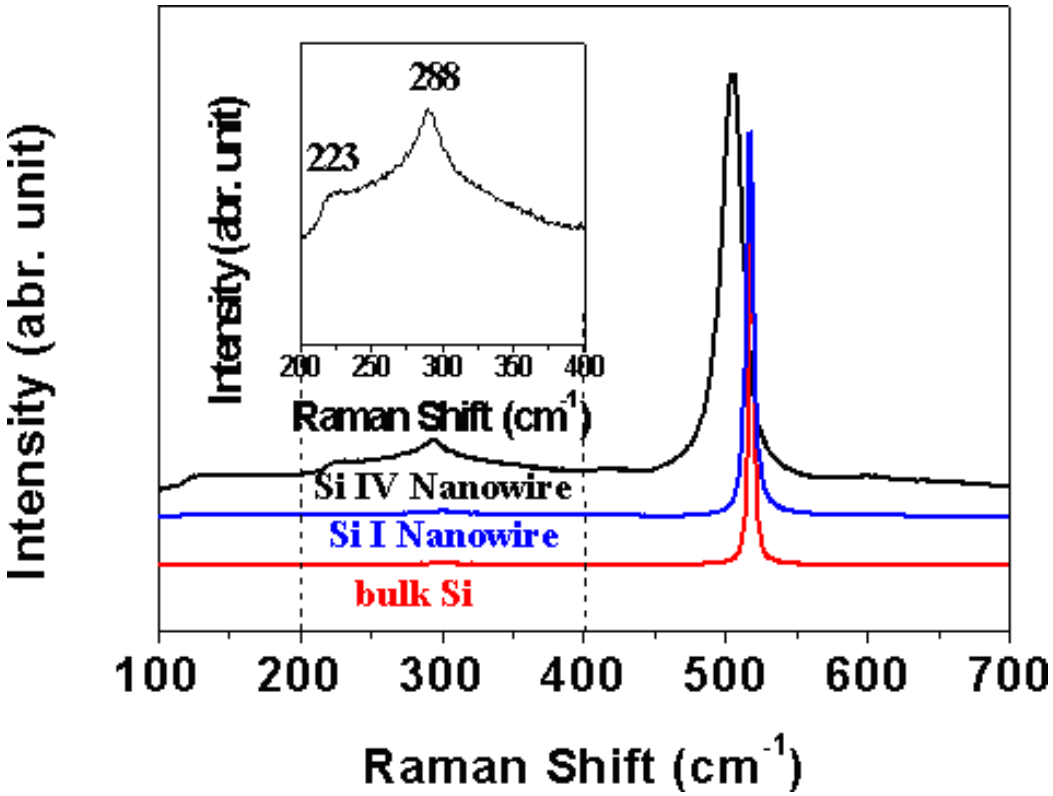


Figure 4.8 Stokes Raman spectra of the hexagonal (Si IV) nanowires, bulk Si and diamond cubic (Si I) nanowires under the same low laser power.

In this thesis, only a small fraction (~2%) of the SiNWs synthesized exhibit the hexagonal (wurtzite) crystalline structures, while all the rest have the conventionally observed diamond cubic phase. Here the observed hexagonal (wurtzite) SiNWs were grown on a Si{111} substrate where the native oxide layer (1~3 nm thick) was removed before immediately transferring the substrate into the growth chamber. This is different from the previously reported hexagonal (wurtzite) SiNWs formed on oxidized substrates with an oxide thickness of 1 μm,[131,132] where the crystallographic alignment with the substrate was lost.

It has been previously suggested that the formation of hexagonal (wurtzite) crystalline structure in SiNWs could be caused by defects like twins[137] and stacking faults,[138] or the phase transformation from diamond cubic to hexagonal Si under high pressure.[125] The applicability of both mechanisms to the hexagonal (wurtzite) SiNWs observed in this thesis is discussed as follows:

(i) Defect-induced formation mechanisms:

Dahmen *et al.*[137] suggested that when a single twin is intersected by a second twin, the strain accommodation causes the region of intersection to transform to the hexagonal stacking (Figure 4.9). Liu *et al.*[138] also suggested that the stacking faults resulting from the fast growth kinetics lead to a variety of hexagonal (wurtzite) Si polymorphs. However, such defect-induced hexagonal (wurtzite) Si formation can be ruled out in this case, as these two arguments result in Si polymorphs, where both the hexagonal (wurtzite) and diamond phases coexist in a localized region [see Figure 4.9(b)], in this thesis only the hexagonal (wurtzite) phase is observed from HRTEM observations, without accompanying any surrounding polymorphs (Figures 4.3 and 4.6 as examples).

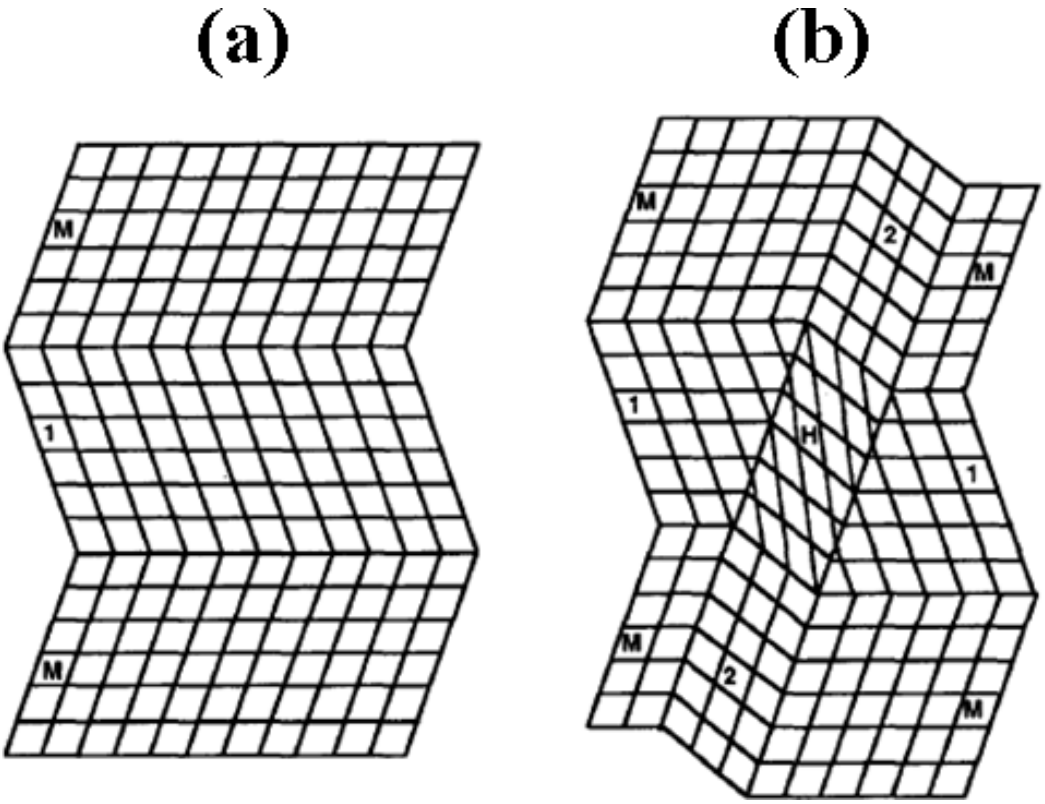


Figure 4.9 Schematic diagram showing a single twin in (a) being intersected by a second twin in (b). Strain accommodation causes the region of intersection to transform to the hexagonal stacking. Matrix labelled M, twins labelled 1 and 2, hexagonal phase labelled H (from Reference 137).

(ii) Pressure-induced phase transformation:

It is known that the diamond cubic Si transforms into hexagonal under a sufficiently high pressure (~8 GPa).[125] Fontcuberta i Morral *et al*.[131] suggested that the large surface stress during the nucleation of the VLS-grown SiNWs, can be a possible cause for the formation of hexagonal (wurtzite) SiNWs. Considering the similarities of the CVD synthesis techniques used by Fontcuberta i Morral *et al*.[131] and used in this thesis, such argument may be applied to explain the observation of the hexagonal (wurtzite) SiNWs in this work. For example, it is hypothesized that if a gold catalyst cluster appears at an unfavourable position on

the Si{111} substrate, *e.g.*, being impeded by neighbouring clusters or substrate defects, the SiNW grown from this Au catalyst may grow under pressure, resulting in the formation of a hexagonal (wurtzite) structured SiNW.

4.3 Growth Direction

4.3.1 Background of Research

The crystallographic growth direction is another important parameter for epitaxially grown SiNWs.[139,140] It has been known that SiNWs grown by VLS with Au as a catalyst tend to grow in the <111> direction.[42,141] Growth in the <110> direction,[142] the <112> direction,[143] and rarely in the <100> direction,[144,145] has also been reported. For SiNWs growing in different crystallographic directions, the shapes and structures of the wire cross section are different.[146] For example, for SiNWs grown in the commonly observed <111> direction, the wire cross section has a hexagonal shape and the six sidewall surfaces are {112} planes.[44] It has been observed that for the VLS-grown SiNWs, the wire growth direction depends strongly on the wire diameter (the diagonal distance of the wire cross section).[147] SiNWs with diameters larger than ~40 nm grown by the VLS approach using Au as a catalyst tend to grow in the <111> direction, while those thinner than ~20 nm are mostly <110> oriented, and the <112> orientation is present in the intermediate range. Wu *et al.*[147] suggested that such dependence of SiNW growth direction on the wire diameter can be due to the

formation of the lowest energy liquid/solid Si{111} interface first and the surface energetics driving the growth along a specific direction as a second stage.

In the past years, models based on various assumptions have been reported to explain the wire diameter dependent SiNW growth direction.[147, 148] Schmidt *et al.*[148] reported the change in the growth direction from <111> to <110> at a diameter of approximately 20 nm in the SiNWs grown by CVD. Based on the modelling of interface and surface energies together with the edge tension term, they demonstrated that for large-diameter SiNWs, the direction with the lowest interface energy is dominant, while for small-diameter SiNWs, the surface energy determines the nanowire preferential growth direction. The free energy F of an interface in the <111>-oriented nanowires can be expressed as:[148]

$$F = \sigma_{LS} A + \varepsilon L \tag{4.1}$$

The first term in Equation 4.1 is the interfacial energy, given by the product of interfacial area A with the corresponding liquid/solid interfacial tension σ_{LS}. The second term is the Si surface tension contribution from the edge of the interface, which is proportional to the circumference L with the edge tension ε, where ε is given by the product of the Si surface tension σ_S with Δz [the interfacial thickness on the Si side (see Figure 4.10)] and $\varepsilon = \sigma_S \Delta z$. The liquid/solid interface is assumed to be flat and perpendicular to the growth direction. Dividing Equation 4.1 by L:

$$f = \frac{F}{L} = \alpha \sigma_{LS} r + \sigma_S \Delta z \tag{4.2}$$

where f is the free energy per unit circumference, $\alpha = \frac{A}{Lr}$, is a geometrical parameter,

and r is the radius of the nanowire. Similarly, the interfacial energy per unit circumference of a <110>-oriented nanowire is

$$f' = \sigma_S' \Delta z + \alpha' \sigma_{LS}' r \tag{4.3}$$

For simplicity it is assumed that Δz takes the same value for both orientations; thus the functions f and f' are crossing at a crossover radius r_C given by

$$r_C = \Delta z \frac{\sigma_S - \sigma_S'}{\alpha' \sigma_{LS}' - \alpha \sigma_{LS}} \tag{4.4}$$

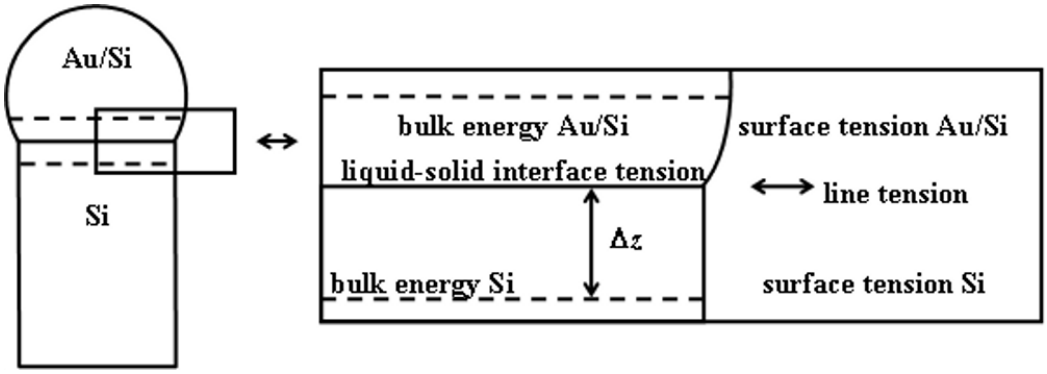


Figure 4.10 Schematic showing the elements in the Schmidt's model (redrawn from Reference 148).

Although the model proposed by Schmidt *et al.*[148] suggests that minimizing the energy with respect to the growth direction results in the <110>-oriented SiNWs for radii smaller than r_C ; while for radii greater than r_C , the <111> direction is energetically more favourable, they did not consider the <112> growth direction due to unavailable parameters.

However, one should note that the VLS-grown SiNW may not always maintain its initial growth direction during the growth, it may change to another growth direction

spontaneously and a nanowire kink is formed. Although such nanowire kinks are undesirable for the integration of SiNW-based devices, they are ideal for building complex 2D and 3D nanostructures (such as branching nanowires) for waveguide devices and biological sensors.[149]

It has been known that SiNW growth conditions have a strong influence on the occurrence of nanowire kinks.[150] For example, it has been reported[151] that kinks tend to occur at high pressure and low temperature, and the high growth rate can be the possible cause of kinking. Wagner *et al.*[152] suggested that nanowire kinks are associated with instabilities at the liquid/solid interface. A change in the liquid/solid interface shape results in the formation of growth kinks. In particular, recent publications[153, 154] suggest that the kinking in SiNWs can be manipulated by controlling the VLS growth, offering the potential to desirably design and synthesize complex nanowire structures for functional device applications. For example, Hyun *et al.*[155] reported that the kinked SiNWs are formed by the sudden change of the pressure during the nanowire growth. Tian *et al.*[153] synthesized the 2D zigzag SiNWs, where kinks are introduced at defined positions and are confined to a single plane, by manipulating the introduction of gas-phase reactants during the growth.

However, many kink-related phenomena in the VLS-grown SiNWs have not been well understood. For example, the shape and crystallographic structures of the SiNW kinks have not been reported in great details. Therefore, it is necessary to study the

detailed structures of the nanowire kinks (should they occur). In this thesis, ~22 μm long axial heterostructured SiNWs with varying doping were grown epitaxially on the oxide-removed Si{111} substrates by the industrial collaborators using a well designed Au-catalysed VLS method (detailed growth methods are described in Chapter 2). The uniformity of the wire growth direction of these SiNWs was checked and the structures of the most commonly observed kinks were studied.

4.3.2 Results and Discussion

4.3.2.1 Determination of the Nanowire Growth Direction

A simple way to determine the growth directions of SiNWs is a "shadow imaging" technique, which has been suggested by Ding *et al*.[156] [Figure 4.11(a)]. This is done by capturing the image and the diffraction pattern simultaneously in the diffraction mode by simply changing the beam convergence so that the beam crossover is under/above the object. The index of the diffraction spot parallel to the nanowire is its growth direction, provided the incident beam is perpendicular to the nanowire.[156] In this work, TEM observation shows that the VLS-grown axial heterostructured SiNWs have the axial length of ~22 μm and diameters in the range of 30~250 nm. About 75% (108 out of 144) of these ~22 μm long SiNWs are straight and kink-free, while the rest (36 out of 144) contain one or more kinks. Among these kinks, a ~109° kink is most commonly observed. The growth directions of both straight and ~109° kinked

SiNWs were determined using the shadow imaging technique.

Figure 4.11(b) shows the indexed SAED patterns of a straight SiNW, and the shadow image of the same wire in the diffraction mode [shown in Figure 4.11(c)] was obtained by increasing the beam convergence. The EDPs in Figure 4.11(b) show a pattern which is characteristic of an fcc material in the <110> zone axis (the ratios of the spot spacings and the angles between the plane normals of the patterns were examined and compared with standard ones). As seen from the shadow image in Figure 4.11(c), the straight SiNW is pointing along the $[\bar{1}11]$ direction. Thus the growth direction of the nanowire is <111>. Figure 4.11(d) shows a ~109° kinked SiNW, viewed along the <110> direction. Using the shadow imaging technique, the growth directions of the SiNW before and after the kink were determined. Figure 4.11(e) is the indexed SAED patterns of the same kink in Figure 4.11(d). By increasing the beam convergence, the shadow image of the kink in Figure 4.11(d) is shown in the diffraction mode. In this shadow image [Figure 4.11(f)], it is seen that the two arms of the ~109° kink are pointing to the $[\bar{1}11]$ and $[1\bar{1}1]$ directions, respectively. Thus the growth directions of the nanowire before and after the ~109° kink are determined to be both <111>.

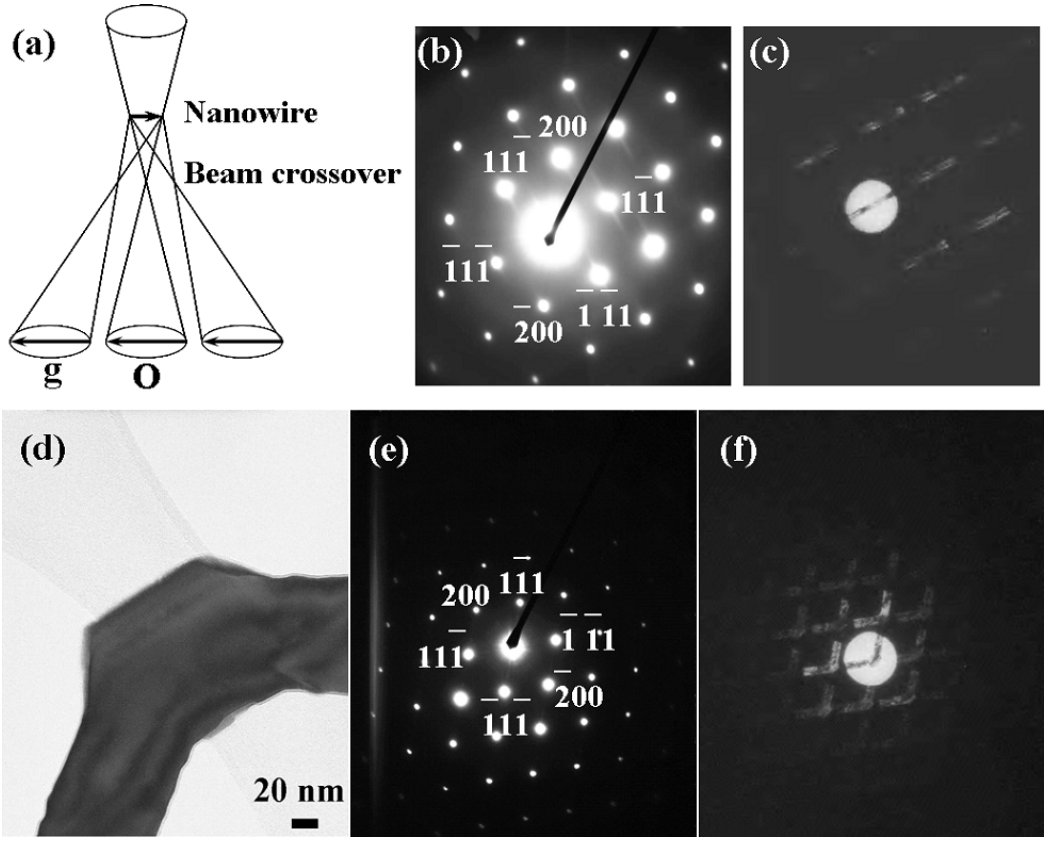


Figure 4.11 Shadow imaging technique for determining the nanowire growth direction: (a) optical diagram for shadow imaging (from Reference 156); (b) SAED patterns of a straight SiNW; (c) the corresponding shadow image of the same straight SiNW recorded in the diffraction mode; (d) TEM image of a ~109° kink in a VLS-grown SiNW, viewed along the <110> direction; (e) SAED patterns of the same kink in (d); and (f) the corresponding shadow image of the same kink in (d) recorded in the diffraction mode.

Another method to determine the SiNW growth direction is to use the HRTEM image and its Fourier transform. As an example shown previously in Figure 4.2, the sidewalls of the SiNW are flat and parallel to the wire growth direction. The Fourier transform in Figure 4.2 shows that the SiNW is pointing along the $[\bar{1}11]$ direction, indicating the wire growth direction to be <111>.

For the ~109° kinked diamond cubic SiNWs observed in this thesis, the growth directions before and after the kink can also be determined using HRTEM. Figure 4.12(a) shows a TEM image of a commonly observed ~109° kinked SiNW, viewed along the <110> direction. Labels 'I~IV' [indicated in Figure 4.12(a)] have been assigned to different positions of the kink. Their corresponding HRTEM images are shown in Figure 4.12(b)~(e), respectively. The Fourier transforms of the HRTEM images in Figure 4.12(b) and (e) show that the SiNW is pointing along the $[\bar{1}11]$ direction before the kink, and along the $[11\bar{1}]$ direction after the kink, respectively. It indicates that the nanowire growth directions before and after the kink are both <111> for the ~109° kink. This is consistent with the observation from the electron diffraction studies.

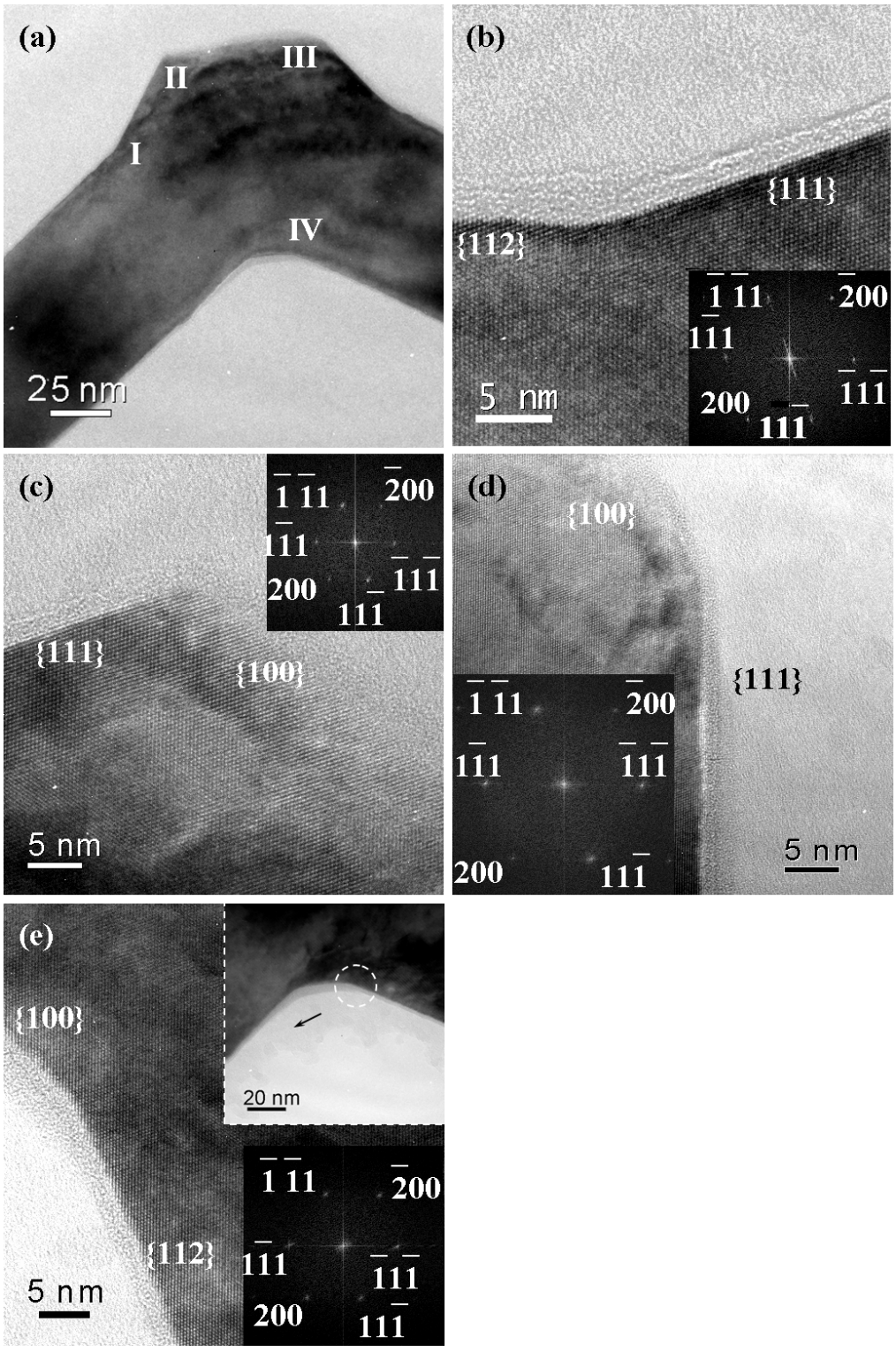


Figure 4.12 (a) TEM image of a ~109° kink in a VLS-grown SiNW, taken along the <110> direction, numbers 'I~IV' are assigned to label different positions; HRTEM image of (b) part I, (c) part II, (d) part III and (e) part IV in (a); insets in (b)~(d): the corresponding Fourier transforms; insets in (e): image taken at low magnification and the corresponding Fourier transform.

4.3.2.2 Elbow-shaped Kink Structure

For the ~109° kinked diamond cubic SiNWs observed in this thesis, it is also seen that the sidewall surfaces of the nanowire do not change abruptly at the kink and they appear to be blunted by several short facets [see Figure 4.11(d) and Figure 4.12(a)]. Here TEM characterizations of 23 diamond cubic SiNWs with ~109° kinks were carried out, and it is interesting to note that similar elbow-shaped structures are always observed when imaging the ~109° kinks along the <110> direction. Using an HRTEM, the crystallographic orientations of these short facets at the kink are revealed.

As an example shown in Figure 4.12, it is seen that the radial width of the wire does not change before and after the kink. The SiNW has a single-crystalline structure across the whole kinking area, as there are no atomic-scale twin defects or stacking faults. It has been known since 1960's that the side surfaces are {112} planes for SiNWs grown in the <111> direction.[44] The orientations of the short facets at the kink are indentified using the HRTEM images and their corresponding Fourier transforms [Figure 4.12(b)~(e)]. Figure 4.13 schematically shows the 2D elbow-shaped structure of the ~109° kink in Figure 4.12(a) (viewed along the <110> direction). At the convex side of the kink, the two {112} planes are replaced by two {111} planes and one {100} plane, while they are blunted by a {100} plane at the concave side.

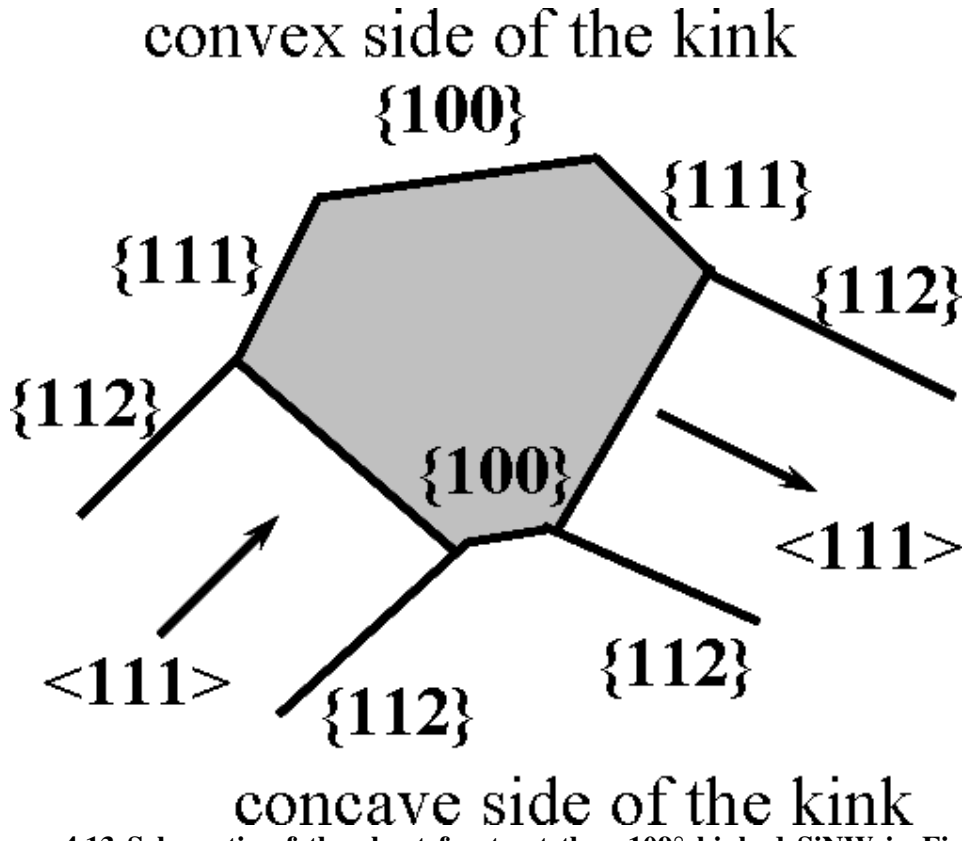


Figure 4.13 Schematic of the short facets at the ~109° kinked SiNW in Figure 4.12(a), viewed along the <110> direction.

SiNWs with ~109° kinks were also imaged using a SEM. Figure 4.14(a) shows an SEM image of a ~109° SiNW kink. Although the kinked SiNW was not viewed along the <110> zone axis, it shows a hint that the nanowire sidewalls do not change abruptly at the ~109° kink, exhibiting an elbow-like structure. Here a possible 3D kink structure visualizing the crystallographic relations around the ~109° SiNW kink is proposed and schematically shown in Figure 4.14(b).

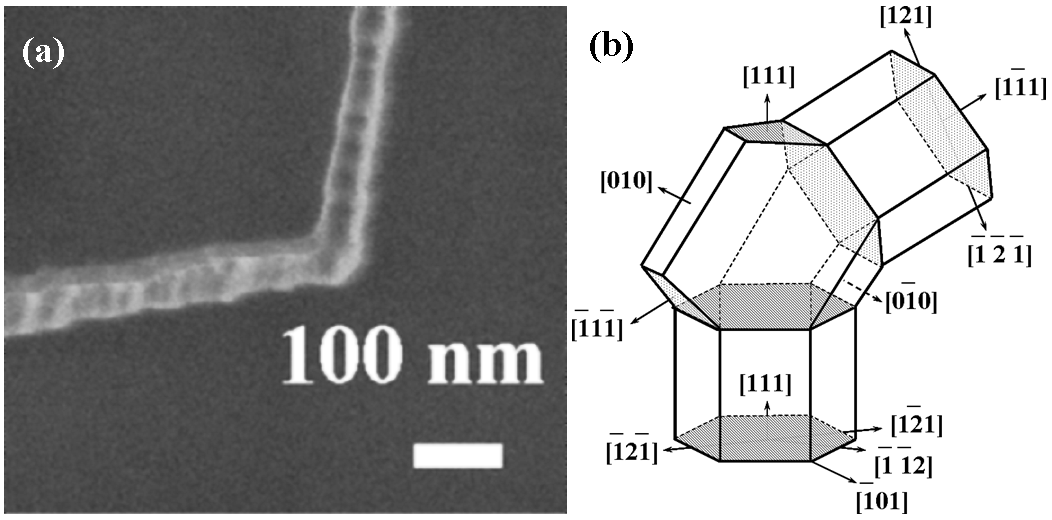


Figure 4.14 (a) SEM image of a ~109° SiNW kink (image taken by Dr Gareth Hughes); and (b) a possible 3D sketch visualizing the crystallographic relationship of the ~109° SiNW kink.

It has been suggested that the formation of VLS-grown SiNW kinks results from a change in the liquid/solid interface shape.[152] In the case of ~109° kinked SiNWs, it is assumed that growth occurs initially at a single liquid/solid interface parallel to a Si{111} plane. However, another inclined {111} plane may be partially exposed at the liquid/solid interface during the growth, if there is any disturbance to the VLS growth process. During the kinking process, growth perpendicular to the newly-formed interface proceeds at the expense of the initial one. The liquid droplet shifts from the original liquid/solid interface to the new interface.[152] However, it is still not clear what determines the morphology and shape of the VLS growth-related nanowire kinks. Based on the *in situ* TEM observation of the SiNW kink formation during the ultra high vacuum (UHV)-VLS growth, Madras *et al.*[157] suggested that different shortening rates of the original Si{111} plane at the convex side of the kink may result in different kink morphologies.

Following Madras' ideas,[157] a possible formation mechanism of the elbow-shaped structure at the ~109° SiNW kink is proposed in this thesis. Figure 4.15(a)~(f) schematically show the <110> projected atomistic model for the formation of the elbow-shaped kink structure in the ~109° kinked SiNW. It is assumed that the diamond cubic SiNW initially grows in the <111> direction by stacking Si{111} planes [Figure 4.15(a)]. The kink initiates when another inclined Si{111} plane [in blue colour in Figure 4.15(b)] is partly exposed at its eventual concave side in addition to the original interface. As shown in Figure 4.15(c), however, the shortening of the original Si{111} plane (in red colour) at the eventual convex side does not begin simultaneously when the new interface (in blue colour) starts to grow in area. Some time later the initial Si{111} interface (in red colour) starts to shorten [Figure 4.15(d)], while the new interface (in blue colour) keeps on growing until finally the initial Si{111} interface has disappeared [Figure 4.15(e)]. During this process, the SiNW does not lengthen along the new <111> growth direction until the growth along the original direction terminates. Due to the delay of the original Si{111} plane shortening, a larger liquid/solid interface is resulted after the droplet completely shifted to the new Si{111} interface [Figure 4.15(e)]. If it is assumed that the volume of the liquid droplet does not change during shifting, the liquid droplet must be stretched thinner on a larger liquid/solid interface, and meets the SiNW at an angle smaller than the droplet's equilibrium contact angle. This thus generates an inward force favouring the narrowing of the SiNW until the droplet's equilibrium contact angle is returned. The axial growth of the SiNW along the new <111> direction

continues when the kink is completed [Figure 4.15(f)]. This model may possibly explain the formation of the elbow-shaped kink structure and the constant wire radial width before and after the ~109° kink observed in this thesis.

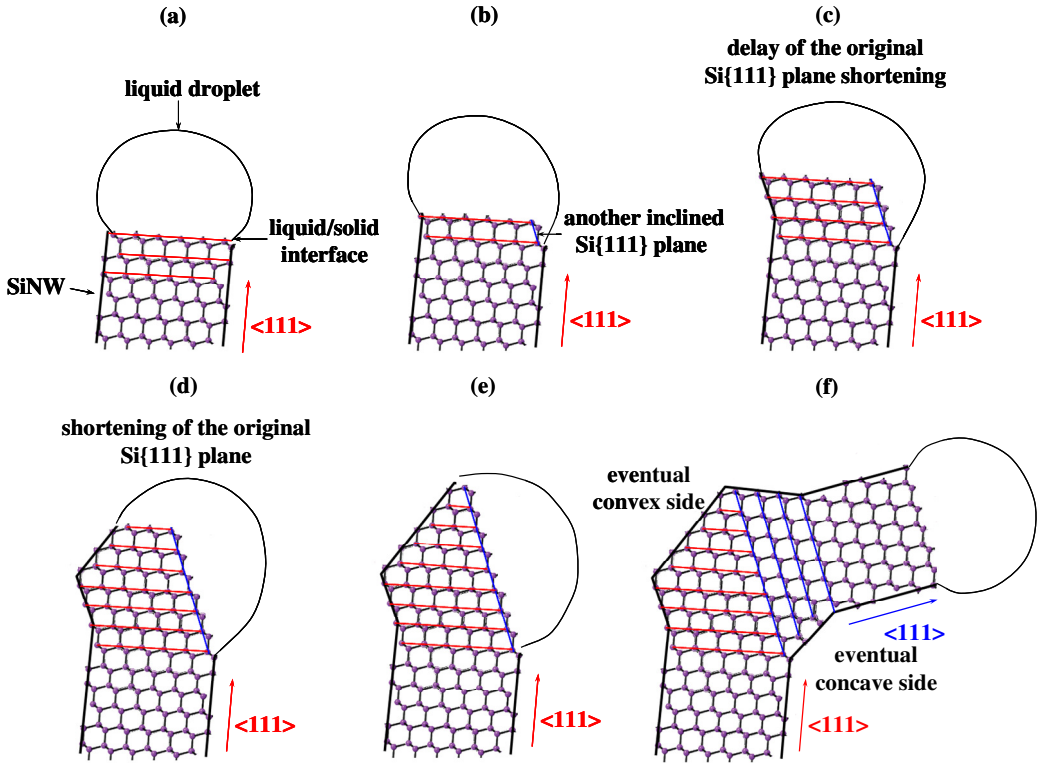


Figure 4.15 The <110> projected atomistic representation of the kink formation mechanisms for resulting in the elbow-shaped kink structure in a ~109° kinked diamond cubic SiNW.

4.4 Chapter Summary

This chapter discussed the uniformities of the crystalline structure and wire growth direction of the VLS-grown axial heterostructured SiNWs on an oxide-removed Si{111} substrate. The phase purity of the VLS-grown SiNWs was checked using HRTEM and Raman spectroscopy, and the wire growth direction was determined

using both the "shadow imaging" and the HRTEM techniques. A very small fraction (~2%) of the synthesized SiNWs exhibit the metastable hexagonal (wurtzite) crystalline structures, while a large majority of the SiNWs have the expected stable diamond cubic phase. About 75% of the ~22 μm long axial heterostructured diamond cubic SiNWs are kink-free and <111>-oriented. For the most commonly observed ~109° kinked diamond cubic SiNWs, the wire growth directions before and after the kink are both <111>. The ~109° kink exhibits an elbow-shaped structure, where the nanowire sidewalls are blunted by several {111} and {100} short facets.

Chapter 5

Doping-dependent Nanofaceting on Silicon Nanowire Sidewalls

5.1 Introduction

Axial heterostructured SiNWs with varying doping are promising in many applications as nanoscale functional devices.[60] Because of the high surface area to volume ratio of nanowires, the surface plays an important role in controlling nanowire properties. To have a good control over the wire surface structure to achieve high-performance functional devices, it is essential to study the dependence of sidewall morphology of SiNWs on the impurity doping.

It is believed that nanowires are cylinders or prisms in shape, bounded by sidewalls, which, on average, are parallel to the growth direction. However, Givargizov[158] observed periodic instabilities in the diameter of Si whiskers grown via the VLS

reaction, as a consequence of which the whiskers consist of a row of knots and necks with approximately equal distances between them [Figure 5.1(a)]. It has been suggested[158] that the periodicity is due to a kind of self-oscillation, where the contact angle of the catalyst droplet depends on the roughness of the liquid/solid interface, which, in turn, depends on the supersaturation of liquid alloy. The instability manifests itself at high temperature, high supersaturation, and only for the so-called whiskers which have a larger diameter (> 300 nm) than nanowires.[158] Nebol'sin *et al*.[159] reported that Si whiskers exhibit microscale surface faceting (periodic "hill-and-valley" structure) during the copper-catalysed VLS growth [Figure 5.1(b)]; however, little or no facets occurred in the whiskers grown with gold catalyst. Hannon *et al*.[160] reported that Au diffusion during SiNWs growth may also induce faceting and determine the sidewall properties, where the formation of facets along the length of the wire leads to very rough, undulating sidewall profiles, resulting from the direct CVD growth of Si on the sidewalls [Figure 5.1(c)]. Ross *et al*.[161] observed in an *in situ* TEM experiment the sawtooth-like faceting on the surface of SiNWs from the Au-catalysed UHV-CVD growth [Figure 5.1(d)]. In their experiments, Ross *et al*.[161] found that the wire cross section is not a regular hexagon, but consists of three wider and three narrower sides. The sawtooth-like faceting is clearly visible on the three narrower sidewalls, but is also occasionally found on the three wider sides, with much smaller amplitude and period. The period of the faceting on the three narrower sidewalls was found to be proportional to the wire diameter.

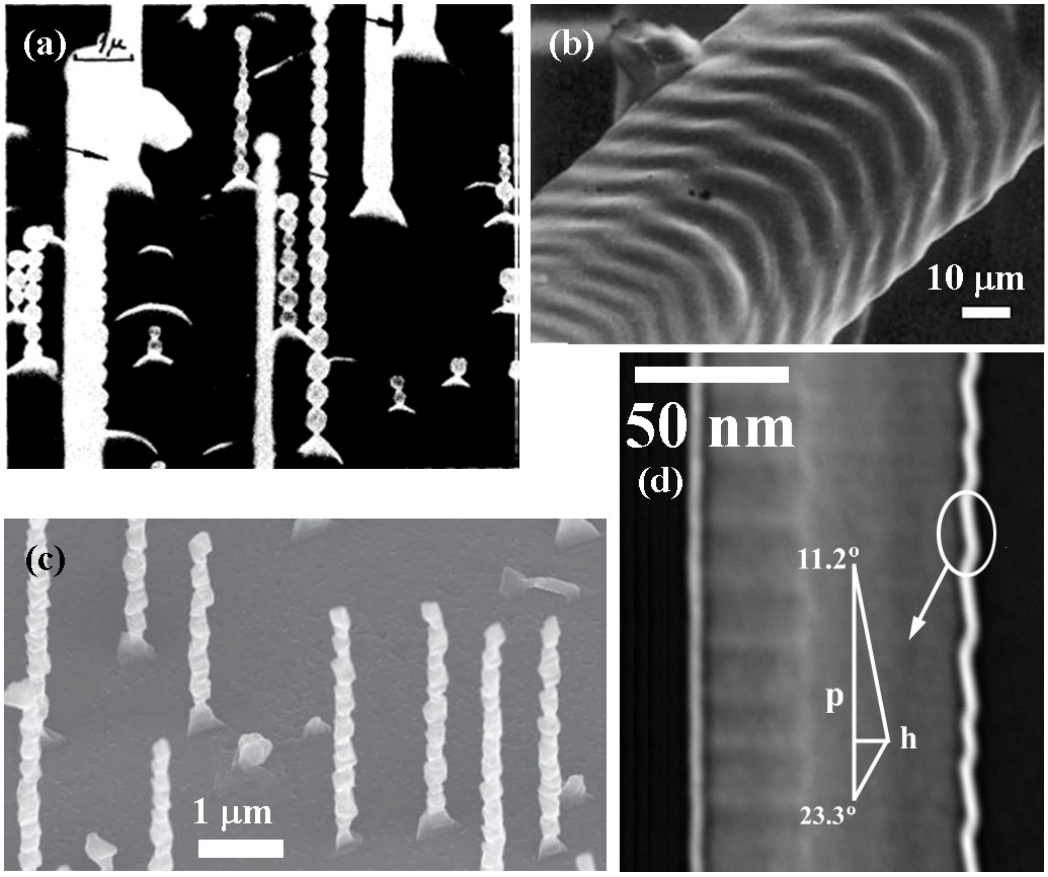


Figure 5.1 Experimental examples of (a) SEM image of the periodic instabilities for Si whiskers (from Reference 158); (b) SEM image showing the microscale faceting on the lateral surface of Si whisker (from Reference 159); (c) SEM image showing the very rough and undulating SiNW sidewalls (from Reference 160); and (d) defocused TEM image of a SiNW showing the sawtooth-like faceting on the nanowire sidewalls. The facet angles are indicated; *p* and *h* denote the sawtooth period and amplitude (from Reference 161).

Ross *et al.*[161] interpreted the occurrence of the faceting as a result from the interplay of the geometry and surface energies of the wire and liquid droplet. In their model, they assumed that the liquid droplet wets the liquid/solid interface only, but not the sidewalls. The change in free energy per unit length of wire growth is

$$\frac{dE}{dz} = L\Delta\mu + \Gamma_v^{eff} \tag{5.1}$$

where $\Delta\mu$ is the supersaturation of Si during growth, and

$$\Gamma_{\nu}^{eff} = \frac{\gamma_{\nu}}{\cos\theta_{\nu}} + (\gamma_d \sin\theta_d + \gamma_i)\sin\theta_{\nu} \tag{5.2}$$

is the surface energy contribution. Here L is the wire width at the terminal facet; ν is an index labelling the different stable facets; γ_{ν} is the surface energy of facet ν, and θ_{ν} is its angle [see Figure 5.2(a)]; γ_d is the surface energy of the droplet, and θ_d is its contact angle [Figure 5.2(a)]; and γ_i is the interface energy between the droplet and wire. If there is no stable facet normal to the growth direction, the wire must be either widening or narrowing as it grows: for a widening wire [$\theta_{\nu} > 0$, as in Figure 5.2(a)], the angle θ_d increases as the wire grows. It raises Γ_{ν}^{eff} (Equation 5.2) when ν is a widening facet. Eventually, a narrowing facet having $\theta_{\nu} < 0$ will become more favourable, as it lowers Γ_{ν}^{eff}. Then the new facet is introduced, and the wire thereafter becomes narrower as it grows. However, in the case of Figure 5.2(b), the narrowing of the wire eventually leads to the droplet applying an increasing outward force on the wire, favouring the introduction of a new widening facet, until the process is reversed. They also proposed that switching only occurs at some critical force, when $\left|\Gamma_w^{eff} - \Gamma_n^{eff}\right| = \Gamma_c$, where $\nu = w$ denotes the widening facet and $\nu = n$ the narrowing one.[161]

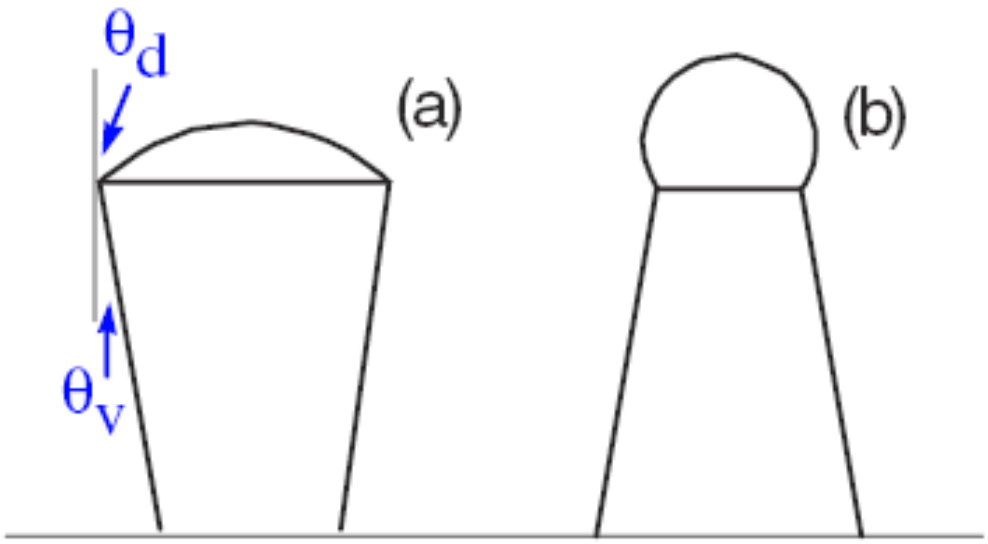


Figure 5.2 Schematic showing the elements of the model proposed by Ross *et al*. (from Reference 161).

Although Ross's model explains the occurrence of periodic faceting in the *in situ* TEM observation of VLS-grown intrinsic SiNWs and predicts the proportionality between the facet period and the wire diameter, it fails to explain the phenomena observed in much wider wires with a rather different cross sectional shape than those reported.[161] The broken symmetry between opposite sides of the wire also indicates the role of additional factors not considered. Furthermore, their SiNWs were grown at relatively high temperature in a UHV environment. Different growth mechanisms may apply in a growth system with background pressure of oxygen or water vapour at low temperatures. In addition, the effects of impurity doping on such nanofaceting are not known. In this thesis, axial heterostructured SiNWs with varying doping were synthesized by the industrial collaborators using a low pressure CVD-VLS approach. The purpose of this chapter is to present and explain the doping-dependent sidewall

nanofaceting observed in axially doped SiNWs, which were not grown under UHV conditions, and to theoretically analyze the equilibrium nanofacet period on 1D nanowire sidewalls in general.

5.2 Observation of the Doping-dependent Nanofaceting

In this work, ~22 μm long axial heterostructured SiNWs consisting of three sections: the *p*-type (B-doped), *n*-type (P-doped) and intrinsic Si sequentially with approximately equal lengths (*p-n-i* SiNWs), were synthesized using the VLS approach (details of synthesis are described in Chapter 2). The growth conditions were designed by the industrial collaborators to precisely control the doping and the axial length in each SiNW section. To study the surface morphology of the ~22 μm long axial heterostructured *p-n-i* SiNWs, TEM images were taken of adjacent areas along the wire growth direction. The image of the whole nanowire was reconstructed by assembling all the TEM images taken from the nanowire base to the Au catalyst (the nanowire top). The holey carbon support film on which the SiNWs were deposited provides a reference for the adjacent TEM images of the nanowire to be matched. Since the growth of the axial heterostructured SiNWs is sufficiently well-controlled, we are confident that for a ~22 μm long *p-n-i* SiNW, the bottom 1/3 of the nanowire corresponds to the *p*-type (B-doped) region, while the middle 1/3 corresponds to the *n*-type (P-doped) region and the top 1/3 (near the Au catalyst) the intrinsic Si region. Therefore, in the reconstructed images of the ~22 μm long *p-n-i*

SiNWs, by measuring the axial length of the wire from the Au catalyst, one can differentiate the three SiNW regions with different doping.

Figure 5.3(a) shows the image of a ~22 μm long axial heterostructured *p*-*n*-*i* SiNW reconstructed from TEM images taken of adjacent areas along the wire growth direction. The three SiNW sections, the *p*-type (B-doped), *n*-type (P-doped) and intrinsic Si with approximately equal lengths are schematically shown. Figure 5.3(b), (c) and (d) show TEM images taken at the *p*-type (B-doped), the *n*-type (P-doped) and the intrinsic SiNW regions, respectively. It is seen that the nanoscale sidewall faceting occurs in the *p*-type (B-doped) region, while both the *n*-type (P-doped) and the intrinsic SiNW regions exhibit a smooth surface morphology.

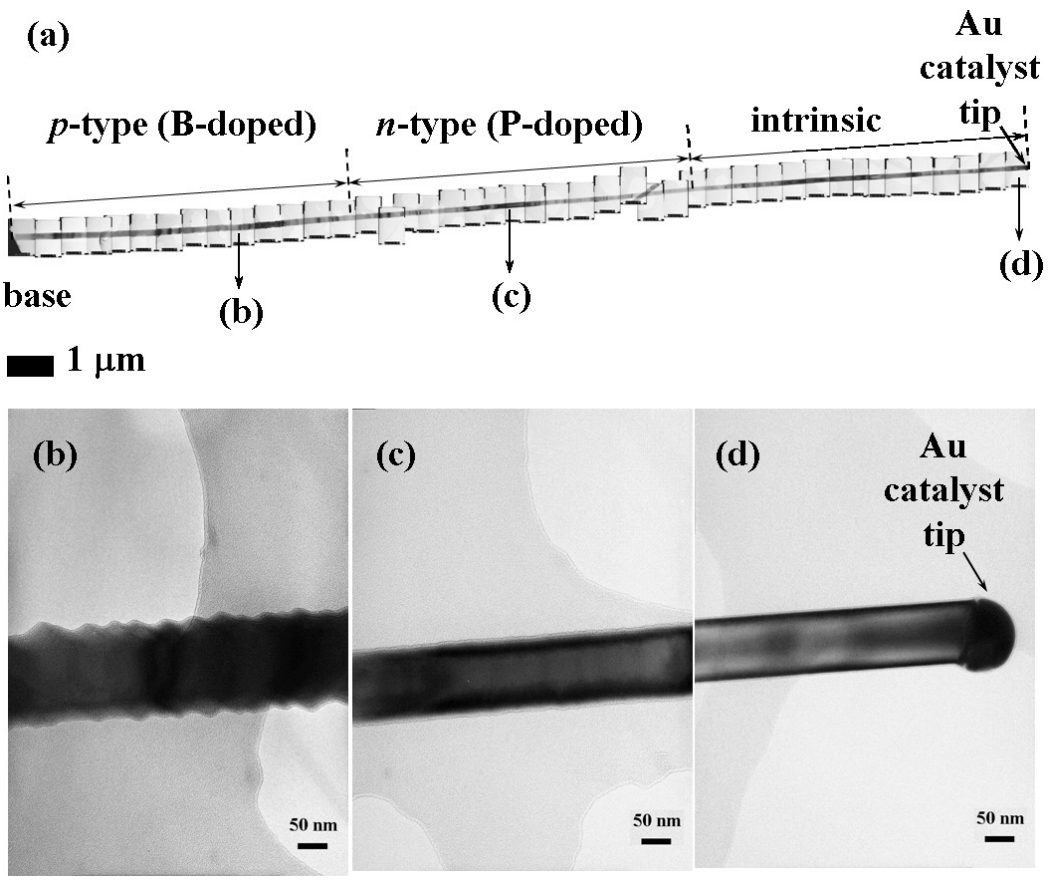


Figure 5.3 (a) Image of a ~22 μm long axial heterostructured *p-n-i* SiNW reconstructed from TEM images taken of adjacent areas along the wire growth direction. TEM image of the SiNW in (a) taken at (b) the *p*-type (B-doped) SiNW region; (c) the *n*-type (P-doped) SiNW region; and (d) the intrinsic SiNW region.

In all nanowires (Figure 5.3 as an example), the wire is thicker in the *p*-type (B-doped) SiNW region, as compared with either the *n*-type (P-doped) or the intrinsic region; however, the radial width of the wire in the *n*-type (P-doped) is close to that in the intrinsic SiNW region. It indicates that the thickening in the radial direction of the SiNWs is accelerated during the growth of the *p*-type (B-doped) region, and the introduction of dopant gas has an influence on the nanowire growth mechanism and behaviour. In this work, SiH_4 gas was the Si source for the nanowire growth, and B_2H_6 and PH_3 dopant gases were used for the *p*-type and *n*-type doping, respectively.

The influence of dopant gas on SiNW growth can be explained from the view point of the dehydrogenation of SiH_4. The reaction mechanism for the dehydrogenation of SiH_4 and the subsequent elimination of hydrogen is[162]

$SiH_4\ (g) \rightarrow H + SiH_3$ (I)

$SiH_3 \rightarrow H + SiH_2$ (II)

$2SiH_2 \rightarrow H_2\ (g) + 2SiH$ (III)

$2SiH \rightarrow H_2\ (g) + 2Si$ (IV)

$2H \rightarrow H_2\ (g)$ (V)

In the case of the *p*-type (B-doped) SiNW section growth, B_2H_6 dopant gas was introduced. It is known that the dissociation energy of B_2H_6 is lower than that of SiH_4,[163] therefore, B_2H_6 first dissociates into BH_3 with the reaction:

$B_2H_6\ (g) \rightarrow 2BH_3\ (g)$ (VI)

Then the combination of BH_3 and SiH_4 forms a SiH_4-BH_3 complex:[163]

$SiH_4 + BH_3 \rightarrow SiH_4\text{-}BH_3$ (VII)

The complex dimmer SiH_4-BH_3 is easily dissociated into SiH_3 and BH_4 radicals:[164]

$SiH_4\text{-}BH_3 \rightarrow SiH_3 + BH_4$ (VIII)

Hence the reaction (II) is enhanced, as well as the subsequent dehydrogenation reactions (III) and (IV). Therefore, B_2H_6 catalyses the SiH_4 dehydrogenation in the vapour phase. It is known that for Si planar surfaces, the enhanced SiH_4 dehydrogenation by B_2H_6 will lead to an increase in the Si growth rate for boron-doped films (some surface boron might be present due to the direct CVD of

B_2H_6),[165,166] suggesting that in the case of SiNWs, it will lead to enhanced nanowire sidewall growth, resulting in the radial thickening in the *p*-type (B-doped) SiNW region.[167]

On the other hand, PH_3, unlike B_2H_6, is known to suppress the Si growth, which is attributed to the PH_3 and P atoms absorbed on the Si surface blocking the reaction sites.[168] Therefore, the radial width of the wire in the *n*-type (P-doped) region is close to that in the intrinsic SiNW region.

HRTEM was used to determine the crystallographic planes on which the nanofaceting occurs. Figure 5.4(a) shows a TEM image of the sidewall nanofacets of an axial heterostructured *p*-*n*-*i* SiNW in the *p*-type (B-doped) region, viewed along the <110> direction. A low magnification image is shown in the inset. The 2D schematic drawing of the nanofacets is also shown in Figure 5.4(a) and the facet angles are indicated. The long and short facets are at angles of ~19° and ~35°, respectively, to the flat sidewall which is parallel to the wire growth direction. Figure 5.4(b) shows the HRTEM image of the nanofacets. It is seen that the nanowire is single-crystalline. The Fourier transform of the image shows the wire growth direction to be <111>. It is known that the original sidewalls (without nanofaceting) of the <111>-oriented SiNWs are Si{112} planes.[44] Here the periodic long and short facets replacing the original Si{112} planes are found to be {111} and {100} surfaces, respectively.

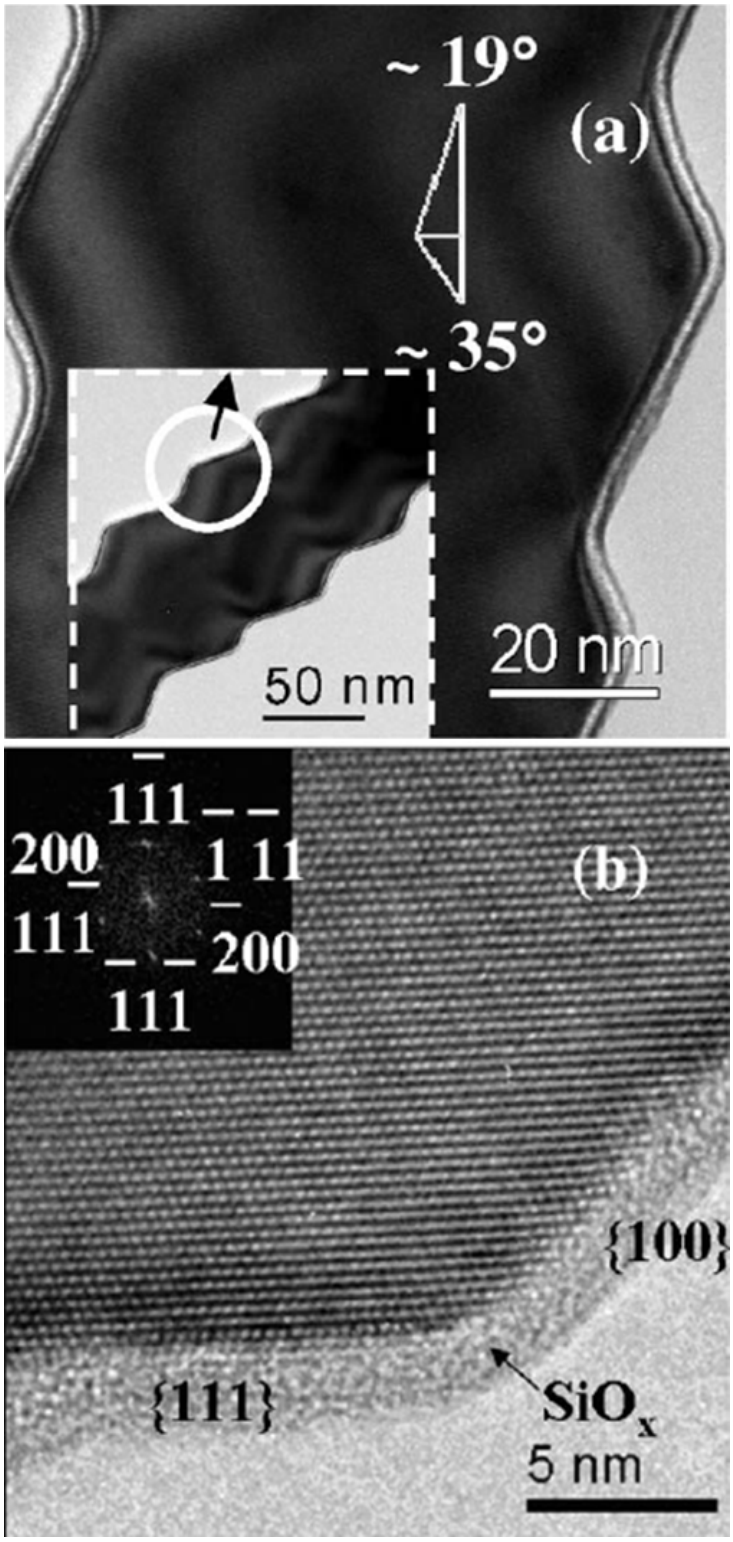


Figure 5.4 (a) TEM image of the sidewall nanofacets in the *p*-type (B-doped) region of an axial heterostructured *p-n-i* SiNW, viewed along the <110> direction, inset: image taken at low magnification and facet angles are indicated; and (b) HRTEM image of the facets, inset in (b): Fourier transform of the image.

High resolution scanning electronic microscopy (HRSEM) was also used to study the shape and morphology of the axial heterostructured *p*-*n*-*i* SiNWs in the *p*-type (B-doped) region. An example is shown in Figure 5.5. Tilting experiments indicate that the SiNW is a hexagonal prism in shape (three of the six sidewalls can be seen in Figure 5.5), and the nanofaceting is observed on all the six nanowire sidewalls.

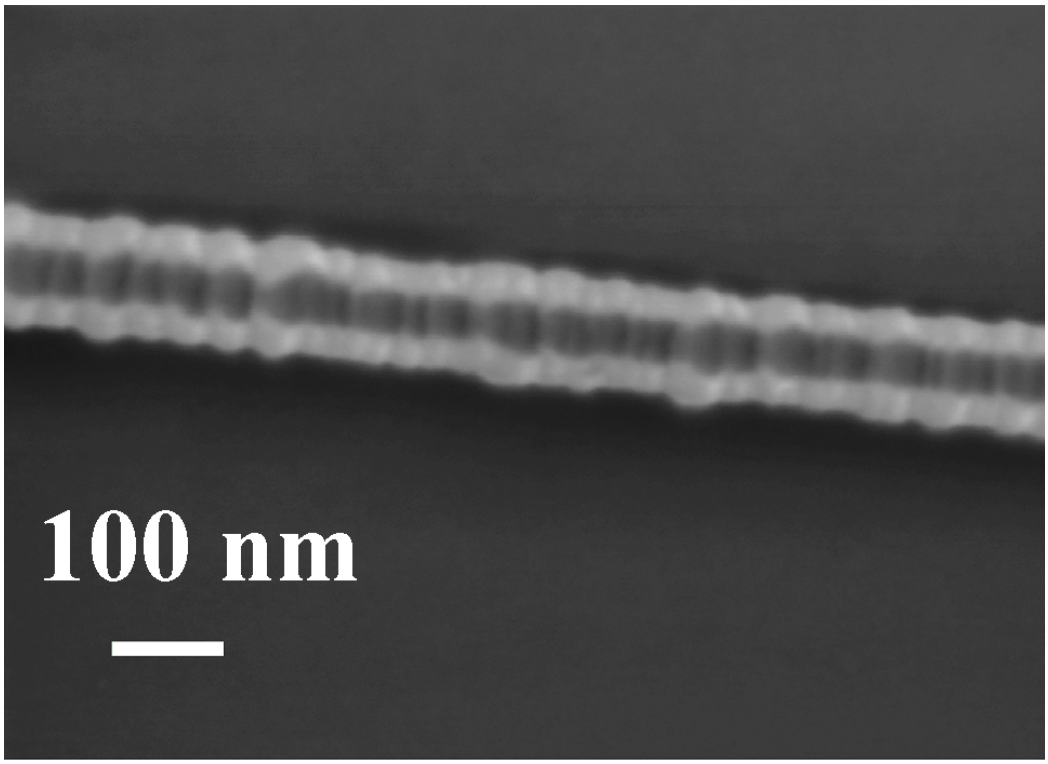


Figure 5.5 HRSEM image of the sidewall nanofacets in the *p*-type (B-doped) region of an axial heterostructured *p*-*n*-*i* SiNW (image taken by Dr Gareth Hughes).

Here the observation is different from the previously reported nanofaceting in intrinsic SiNWs during the UHV-VLS growth.[161] For the previously reported SiNW nanofaceting, the wire cross section is an irregular hexagon with alternating wider and narrower sides, and the nanofaceting occurs primarily on the three narrower sidewalls,

and is occasionally visible on the three wider sides [as shown in Figure 5.6(a)].[161] In the work presented here, the axial heterostructured *p*-*n*-*i* SiNWs were not grown under UHV conditions, and the difference in nanowire morphology could be due to the much higher growth pressure used in this work. Therefore a different 3D crystal model [Figure 5.6(b)] was constructed, in order to match both the HRTEM and HRSEM observations of the sidewall nanofaceting in the *p*-type (B-doped) region of the axial heterostructured *p*-*n*-*i* SiNWs. In this model, growth occurs at a single liquid/solid interface parallel to a Si{111} plane, and the wire surfaces are bounded with alternating long {111} and short {100} faces. Figure 5.6(c) schematically shows the 2D structure of the sidewall nanofacets viewed along one of the <110> directions.

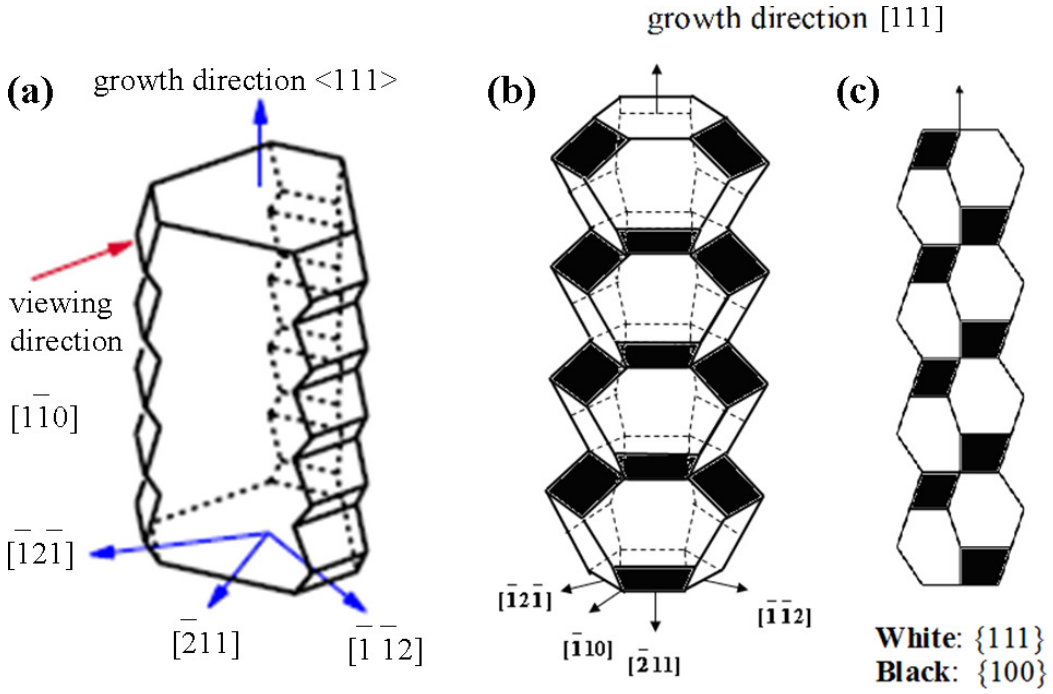


Figure 5.6 (a) Schematic of the 3D structure of the previously reported intrinsic SiNW with sidewall nanofaceting (from Reference 161); (b) schematic of the 3D structure of the axial heterostructured *p-n-i* SiNW with sidewall nanofaceting in the *p*-type (B-doped) region observed in this work; and (c) schematic of the 2D structure of the wire in (b) viewed along the [$\bar{1}$10] direction.

5.3 The Cause of the Doping-dependent Nanofaceting

5.3.1 Discussion on the Previously Suggested Mechanisms

The possible cause for the occurrence of nanofaceting on nanowire sidewalls has been previously discussed, including the regular twinning induced faceting,[169] Au-rich clusters on the SiNW sidewalls,[170] and/or absence of stable orientation parallel to the wire growth direction.[161] To study the applicability of these mechanisms on the

doping-dependent nanofaceting observed in this thesis, detailed analysis of each suggestion is as follows:

(i) Twinning-induced faceting:

It has been suggested[169] that regular and repeated formation of {111} twin planes in group III-V nanowires can result in the {111} type faceting on nanowire sidewalls. In this model (as shown in Figure 5.7), the nanowire sidewall facets are correlated to twin segments of alternating orientation. The segments have varying thickness and are separated by twin planes.[171] However, no twin faults were observed from extensive HRTEM characterizations [Figure 5.4(b) as an example] of the faceted *p*-type (B-doped) region in the axial heterostructured *p-n-i* SiNWs. Therefore, the twinning-induced faceting can be ruled out in this case.



Figure 5.7 3D atomic model of the nanowire with faceting on sidewalls. Such faceting results from the periodic alternation of twin segments (from Reference 171).

(ii) Au-rich clusters induced faceting:

Au is often used as the metal catalyst to grow nanowires.[172] However, Au can diffuse throughout the wire and the substrate and remains in the wire and its surfaces.[173] Au is known to induce faceting on Si surfaces with a wide variety of orientations.[174,175,176] Therefore, Au-rich clusters on the SiNW sidewalls are suggested to cause faceting on nanowire surfaces.[173]

To study if the nanofaceting observed in this thesis is induced by surface Au, HAADF-STEM was used to detect single Au atoms in SiNWs. STEM measurements were carried out in a 200 kV JEOL JEM-2200MCO STEM with two aberration correctors. Figure 5.8(a) shows the HAADF image of an axial heterostructured *p-n-i* SiNW taken near the Au catalyst tip on the <112> zone axis. Bright spots associated with impurities are visible, two of which are highlighted. STEM images are sometimes called *Z*-contrast,[177] because the intensity scattered by an atom scales with the atomic number *Z* of the atom. The intensity profiles across several successive Si planes through the bright spots 1 [along the aa' direction indicated in Figure 5.8(a)] and 2 [along the bb' direction in Figure 5.8(a)] are shown in Figure 5.8(b). Excess intensity associated with each impurity is shown in each plot in Figure 5.8(b). As seen from the intensity profile across several Si lattices through the impurity 2 [along the bb' direction], single impurity imaged near the Au catalyst tip [near the position b' in Figure 5.8(a)] produce similar excess intensities, providing circumstantial evidence that the

bright spots 1 and 2 are due to single Au atoms. Figure 5.8(c) shows the HAADF image of the same axial heterostructured *p*-*n*-*i* SiNW taken at the faceted *p*-type (B-doped) region on the <110> zone axis. However, no bright spots with excess intensities are observed to decorate the sidewall surfaces, indicating that the faceted *p*-type (B-doped) SiNW sidewall surface is free of Au contamination. As clean surfaces rarely facet, it indicates that the sidewall nanofaceting observed in this thesis should be due to some factors other than the Au-rich clusters on nanowire surfaces.

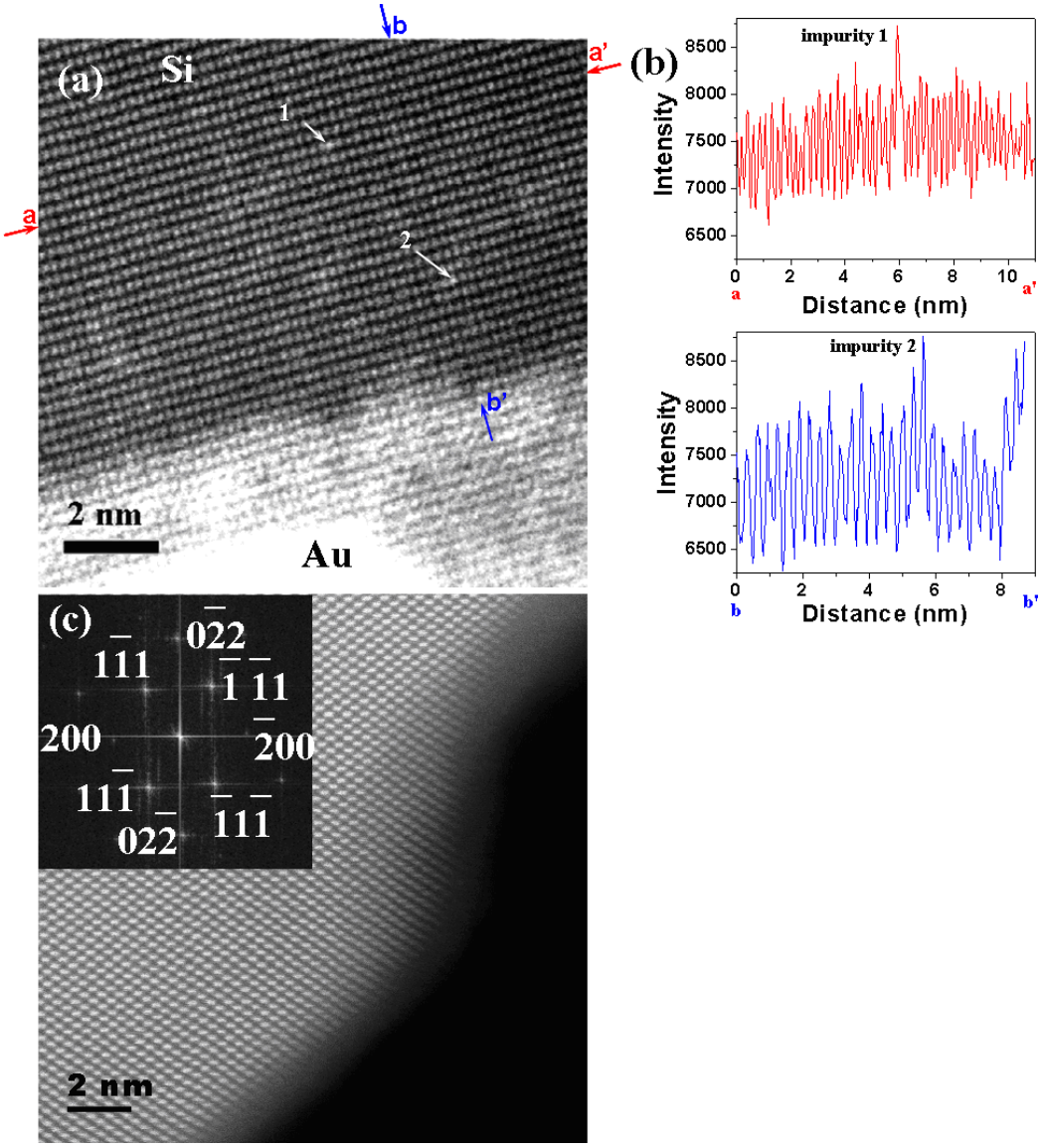


Figure 5.8 (a) HAADF-STEM image of single Au atoms (marked by arrows) in the near-catalyst region of an axial heterostructured *p-n-i* SiNW, as a reference for the contrast between Au and Si; (b) intensity profiles across several Si lattices through two bright spots associated with impurities 1 [along the aa' direction in (a)] and 2 [along the bb' direction in (a)]; and (c) HAADF image of the faceted *p*-type (B-doped) SiNW region in the same *p-n-i* SiNW, viewed along the <110> direction, inset: Fourier transform of the image (the HAADF-STEM images were taken by Dr Peng Wang).

(iii) Faceting resulting from the absence of stable orientation parallel to the wire growth direction:

Ross *et al*.[161] have proposed a thermodynamic model to explain the occurrence of sidewall nanofaceting observed during the UHV-VLS growth of intrinsic SiNWs. In their model, it is suggested that the faceting alternation results from the interplay of the geometry and surface energies of the wire and liquid droplet during the nanowire growth.[161] The allowed facets correspond to a wire that is widening or narrowing as it grows (as shown in Figure 5.2).

To test the applicability of this model to the nanofaceting observed in this thesis, a reference nanowire sample consisting of four sections: intrinsic, *p*-type (B-doped), *n*-type (P-doped), and intrinsic Si sequentially with approximately equal lengths (*i*-*p*-*n*-*i* SiNWs) was prepared using the same VLS approach described in Chapter 2. In such ~24 μm long axial heterostructured *i*-*p*-*n*-*i* SiNWs, ~6 μm long intrinsic SiNWs were grown before growing the remaining ~18 μm long *p*-*n*-*i* sections (~6 μm long for each section). If nanofacets result from the self-oscillation of the liquid droplet during the *p*-type (B-doped) section growth, nanofacets would be expected to occur only in the *p*-type (B-doped) region, while the initially-grown intrinsic region should exhibit the same smooth surface morphology as the finally-grown intrinsic region. Both TEM and HRSEM techniques were used to characterize the surface morphology of the axial heterostructured *i*-*p*-*n*-*i* SiNWs,

and the TEM image analysis follows the same method used to study the *p*-*n*-*i* SiNWs.

It is observed that the sawtooth-like nanofaceting also occurred in the initially-grown intrinsic region, in addition to the faceted *p*-type (B-doped) SiNW region (Figure 5.9), while both the *n*-type (P-doped) and the finally-grown intrinsic SiNW regions still exhibited smooth surface morphology. The growth conditions are the same for the initially-grown and the finally-grown intrinsic SiNW regions, and no Au loss is observed as the wire grows, so the liquid droplet configuration at the liquid/solid interface is expected to be the same during the growth of the initially-grown and the finally-grown intrinsic SiNW regions. It indicates that the nanofaceting occurred on the initially-grown intrinsic SiNW sidewalls does not result from the periodic changes of the liquid droplet configuration at the liquid/solid interface during the growth as suggested in Ross's model (Equations 5.1 and 5.2). Other factors should be considered to explain the nanofaceting on SiNW sidewalls observed in this thesis.

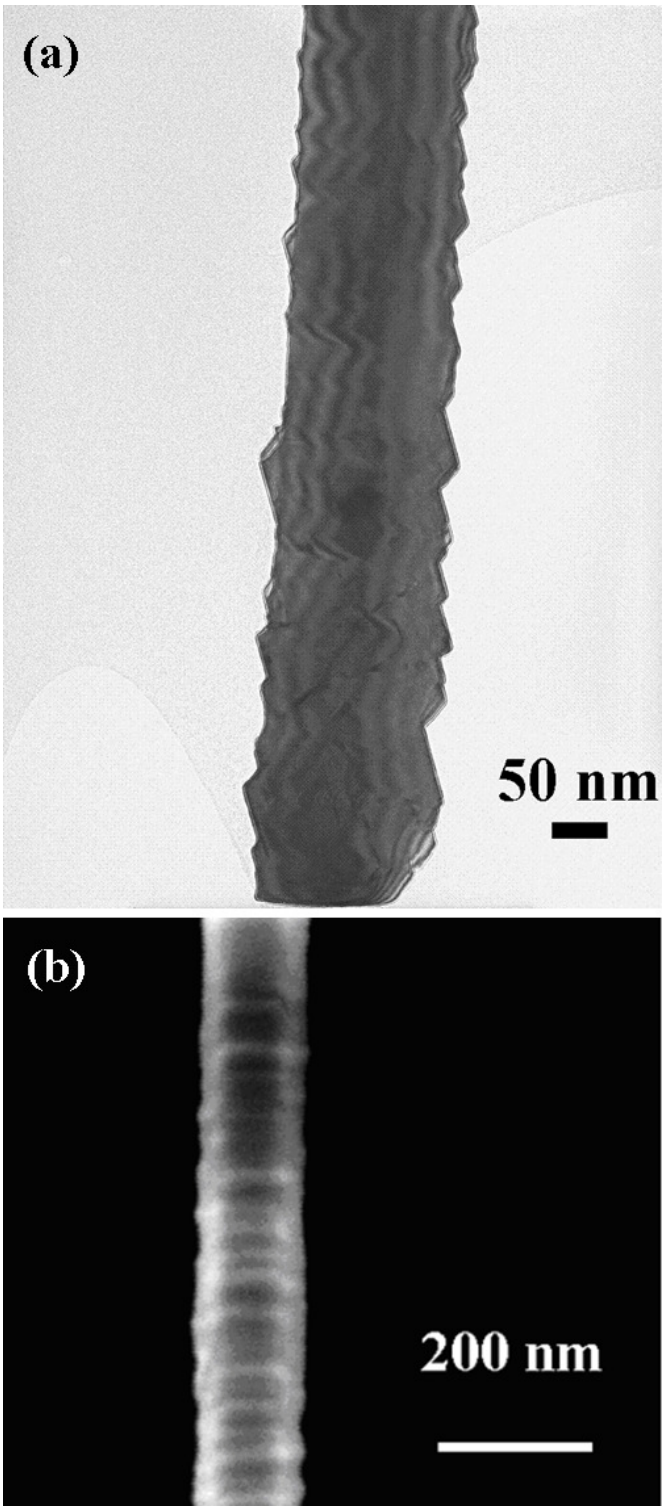


Figure 5.9 (a) TEM image showing the initially-grown intrinsic region of a ~24 μm long axial heterostructured *i-p-n-i* SiNW, viewed along the <110> direction; and (b) HRSEM image of the initially-grown intrinsic region of a ~24 μm long axial heterostructured *i-p-n-i* SiNW (the HRSEM image was taken by Dr Gareth Hughes).

5.3.2 Impurity-induced Faceting Mechanism

Here an impurity-induced faceting mechanism is proposed to explain the doping-dependent nanofaceting on SiNW sidewalls observed in this thesis. It is known that faceting often occurs when the environment of the surface is changed, *e.g.*, by the introduction of a small density of impurities or by a change in the temperature.[178] In this work, the growth temperature was kept constant during the growth of the axial heterostructured SiNWs; however, dopant impurities were introduced.

Figure 5.10(a) shows two growth interfaces in a VLS process, the liquid/solid interface between the droplet and the wire, and the vapour/solid interface between the vapour-phase reactants and the exposed sidewalls of the growing nanowire. During the growth of the axial heterostructured SiNWs, the introduction of the B_2H_6 dopant gas catalyses the SiH_4 dehydrogenation, leading to an enhanced SiNW sidewall growth at the vapour/solid interface. Faceting requires a large amount of mass transport at the surface,[178] and the nanofaceting occurs on the SiNW sidewalls during the enhanced vapour-solid growth when the B_2H_6 dopant gas is introduced. The sidewalls of the <111>-oriented SiNWs are Si{112} planes,[44] which can be considered as periodic {111} and {100} steps with atomic-layer heights [Figure 5.10(b)].[179] It has been reported previously that very small levels of impurities, such as C,[180] Sb,[181] and H,[182] can generate facets on the Si{112} surface, suggesting the possibility that surface boron impurities could have had a similar effect on the Si{112}

nanowire sidewalls, using the periodic {111} and {100} steps as nucleation sites for the facet growth.

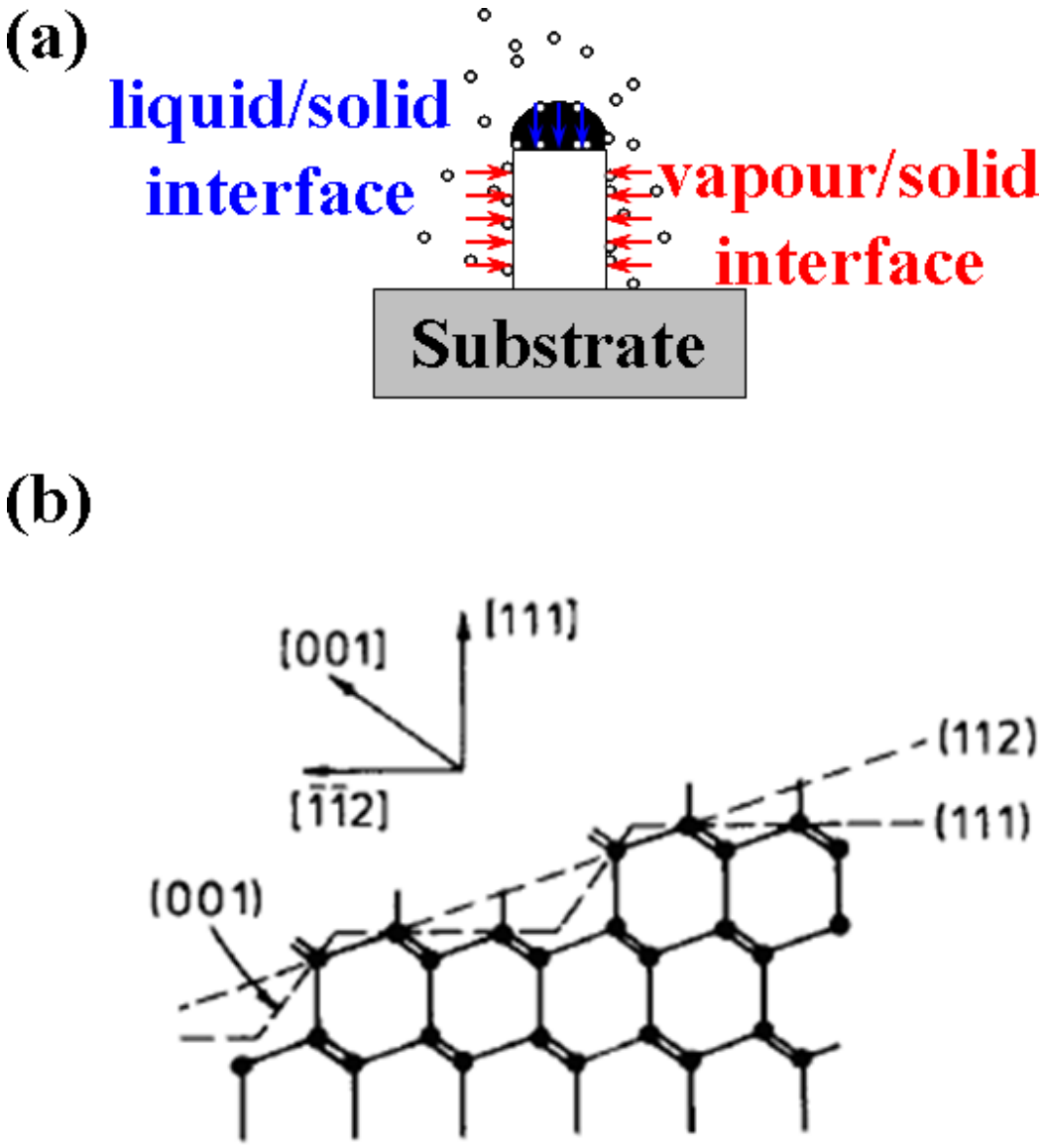


Figure 5.10 (a) Schematic showing the two growth interfaces during a VLS nanowire growth; and (b) schematic showing the side view of the ideal Si{112} surface.

5.4 Nanofaceting Model of Nanowires

It is known that many microstructural properties of 1D nanowires depend strongly on dimensionality.[131,147] It is thus of interest to study if the observed nanofaceting on SiNW sidewalls exhibits such size-dependent properties. Here the dependence of the magnitude of the sidewall nanofaceting on the diameter of SiNWs was studied (the shape of the wire cross section is close to a regular hexagon, and the wire diameter is defined as the diagonal of the regular hexagonal wire cross section). Figure 5.11(a) shows the schematic of wire cross section. It is assumed that the wire cross section is a regular hexagon before the faceting occurs and the wire diameter is $2r$, with the length of each side of the hexagon being r. Figure 5.11(b) shows the schematic of the faceted SiNW viewed along the $[\bar{1}10]$ direction, two parallel dashed lines (in red colour) are drawn as the flat sidewalls parallel to the wire growth direction before the faceting occurs, geometric relationships show that the perpendicular distance between these two parallel dashed lines is equals to $\sqrt{3}r$. L denotes the periodicity length (the facet period), as shown in Figure 5.11(b). If the lengths of both the $\sqrt{3}r$ and L can be measured in an actual TEM image of the faceted SiNW taken along the <110> zone axis, the relationship between the facet period L and the wire diameter $2r$ can be obtained by performing a statistical analysis over a number of faceted SiNWs.

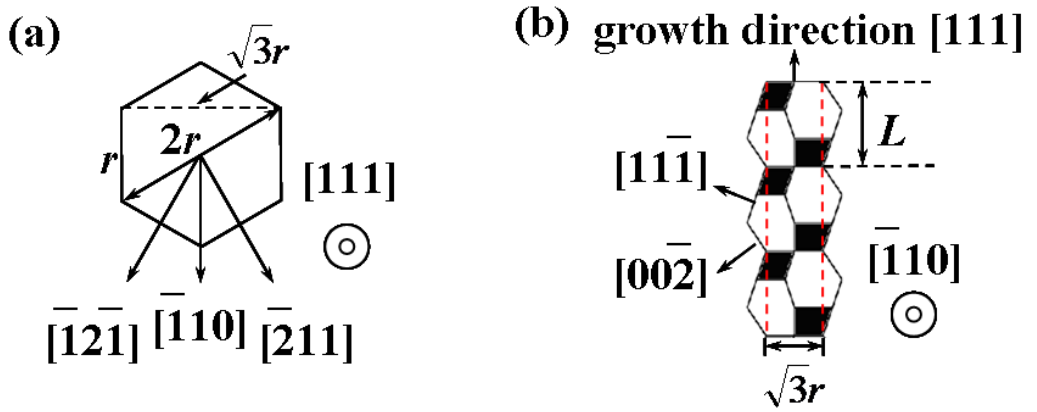


Figure 5.11 (a) Schematic of the regular hexagonal wire cross section; and (b) schematic of the faceted nanowire viewed along the [$\bar{1}10$] direction.

In this work, TEM images of the *p*-type (B-doped) regions (with sidewall nanofaceting) in several <111>-oriented axial heterostructured *p-n-i* SiNWs were taken along the <110> zone axis. Four examples are shown in Figure 5.12(a)~(d). Following the ideas stated above, two parallel dashed lines [in red colour in Figure 5.12(a) as an example] are schematically drawn as the flat sidewalls parallel to the wire growth direction before the faceting occurs. The perpendicular distance between these two parallel lines is measured as $\sqrt{3}r$ and the value of the wire diameter $2r$ can be obtained. It is seen from Figure 5.12(a)~(d) that the facet angles are kept constant while the width of facets varies. To obtain the average facet period of the wire, the number of facets on the SiNW sidewalls in the TEM image was counted, the width of each facet was measured and the average facet period was determined by averaging over these measured facet widths.

The measured average facet periods are 61 $\pm$ 4 nm, 56 $\pm$ 2 nm, 51 $\pm$ 3 nm and 50 $\pm$ 3

nm, for the SiNW with the diameters of ~50 nm [Figure 5.12(c)], ~60 nm [Figure 5.12(b)], ~150 nm [Figure 5.12(a)] and ~175 nm [Figure 5.12(d)], respectively. Figure 5.12(e) plots the average facet period versus the wire diameter for several <111>-oriented axial heterostructured *p-n-i* SiNWs in the faceted *p*-type (B-doped) region. It is seen that the average facet period decreases as the wire diameter increases.

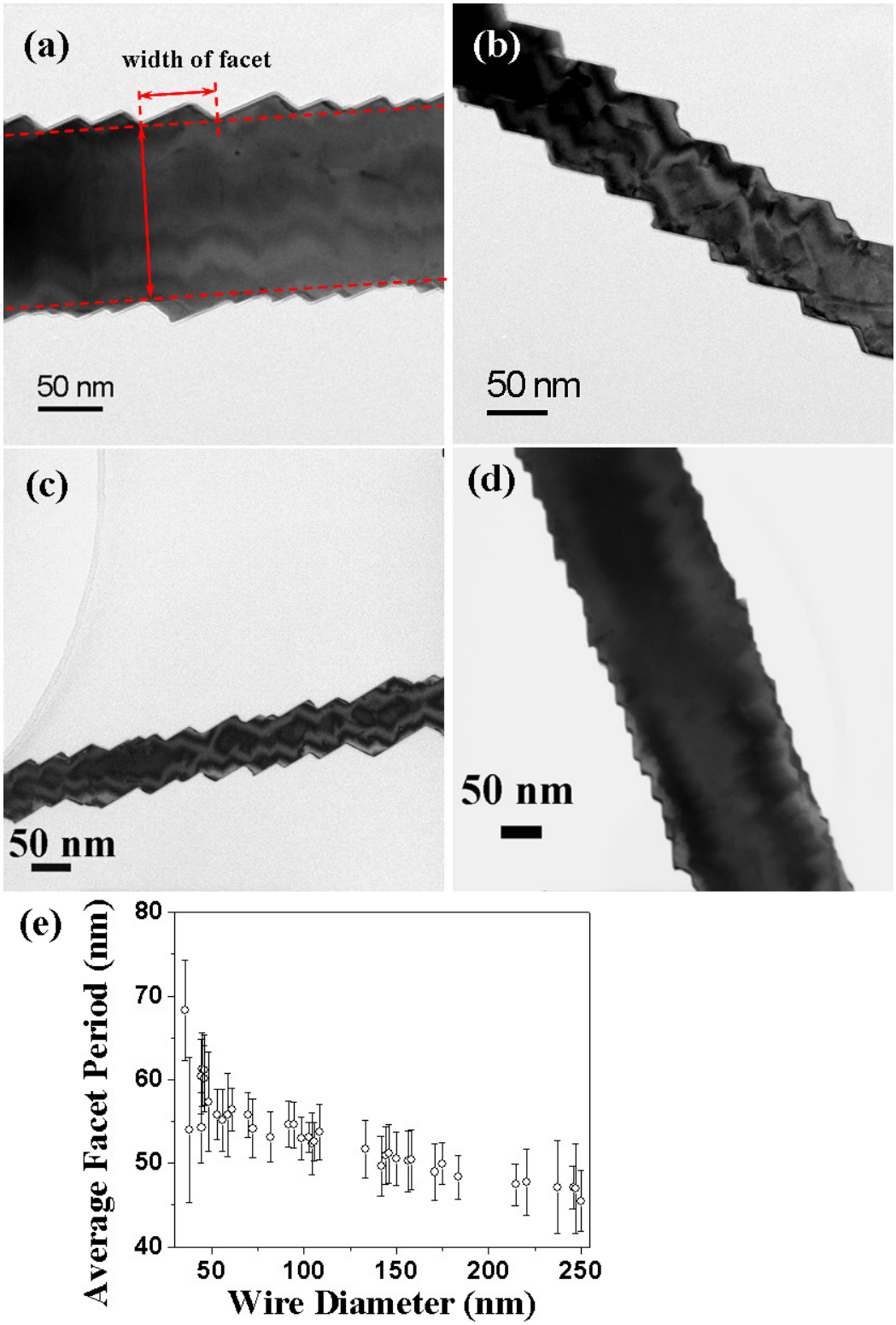


Figure 5.12 TEM images of <111>-oriented axial heterostructured *p-n-i* SiNWs in the faceted *p*-type (B-doped) region with wire diameters of (a) ~150 nm; (b) ~60 nm; (c) ~50 nm; (d) ~175 nm; and (e) plot of average facet period versus wire diameter. TEM images in (a)~(d) are all viewed along the <110> zone axis.

To understand the dependence of facet period on the wire diameter in 1D nanowires, firstly it is necessary to have a general understanding of the faceting mechanisms of a planar surface. Faceting of a planar surface and its corresponding mechanisms are longstanding problems in materials science and surface physics.[183,184,185] Broadly, faceting is defined as the break-up of a surface of some arbitrary macroscopic orientation into a "hill-and-valley" structure which exposes surfaces of different orientations.[178] Faceting can be understood in terms of the lowering of surface energy by the reconstruction of a surface into facets with lower surface energy, despite the resulting increase in surface area. A simple consideration of surface energies, however, does not predict the period of the facets on a surface. For a fully faceted surface under steady state conditions, the total surface area for each facet is fixed no matter what facet size distribution there is. Marchenko *et al.*[186] have developed the theory of a periodically faceted surface, and found the facet period of the equilibrium structure. It is shown[186] that the period of faceting results from a competition between the energy cost of forming the edges of the facets and the elastic relaxation energy due to the discontinuity of the surface stress tensor at the edges. This is because the edge formation energy cost drives towards long facet periods with fewer edges, while the elastic relaxation energy partially cancels as the edges get closer together thereby driving towards a shorter facet period.[187] While existing models for surface faceting can reliably predict facet period on planar surface,[188] they fail in the case of nanowire sidewalls.

Following the faceting theory of a planar surface,[186] a model predicting the period of nanofacets on nanowire sidewalls is developed in this thesis. By considering the periodic nanofaceting on one of the six nanowire sidewalls (it is the same for the other five sidewalls), the total free energy f of the faceted nanowire sidewall per unit projected area is given by

$$f = f_{surf} + E_{boundaries} + E_{elastic} \tag{5.3}$$

where f_{surf} is the surface free energy of all facets on the sidewall, $E_{boundaries}$ is the energy for forming edges, apexes and sidewall boundaries, and $E_{elastic}$ is the elastic energy due to the discontinuity of the surface stress tensor at the crystal edges.[189]

Here the surface free energy f_{surf} can be expressed as

$$f_{surf} = c_1\gamma^0_{\{111\}} + c_2\gamma^0_{\{100\}} \tag{5.4}$$

where $\gamma^0_{\{111\}}$ and $\gamma^0_{\{100\}}$ are the surface tensions of the {111} and {100} facets, respectively, and c_1 and c_2 are constants. Because the interplanar angles between Si{112}, {111} and {100} planes are fixed, the surface area of either the {111} or the {100} facet is proportional to that of the original (unfaceted) {112} SiNW sidewall.

For a nanowire structure, $E_{boundaries}$ should include the energy of the edges formed between nanofacets of different orientations on one sidewall, and the energy of apexes and sidewall boundaries formed when nanofacets on neighbouring sidewalls meet (the edges, apexes and sidewall boundaries are schematically shown in Figure 5.13). As seen from Figure 5.13, within the axial length of one facet period *L*, there are on

average two edges and two apexes formed. There are also two boundaries formed between the {111} and {100} facets on neighbouring sidewalls, and one boundary between the adjacent {111} facets. Thus the energy of boundaries per unit projected area is given by

$$E_{boundaries} = 2\frac{\eta}{L} + 2\frac{B}{rL} + \frac{2c_3\eta_1 + c_4\eta_2}{r} \tag{5.5}$$

The first term in Equation 5.5 is the edge formation energy per unit projected area, where η is the free energy cost per unit length of creating an edge between {111} and {100} nanofacets on one sidewall. The second term is the apex formation energy per unit projected area, where *B* is the free energy due to the facet interactions at the apex. The third term in Equation 5.5 describes the energy of the sidewall boundaries formed, where η_1 and η_2 are the free energy costs per unit length for forming the sidewall boundaries between {111} and {100} facets and the boundaries between the adjacent {111} facets on neighbouring sidewalls, respectively. Here c_3 and c_4 are constants, because the interplanar angles between Si{112}, {111} and {100} planes are fixed, the length of the sidewall boundaries is proportional to the axial length of the nanowire. The projected area of faceted sidewall is proportional to *r*, whereas the numbers of apexes and sidewall boundaries are independent of *r*, so the second and the third terms in Equation 5.5 are inversely proportional to *r*.

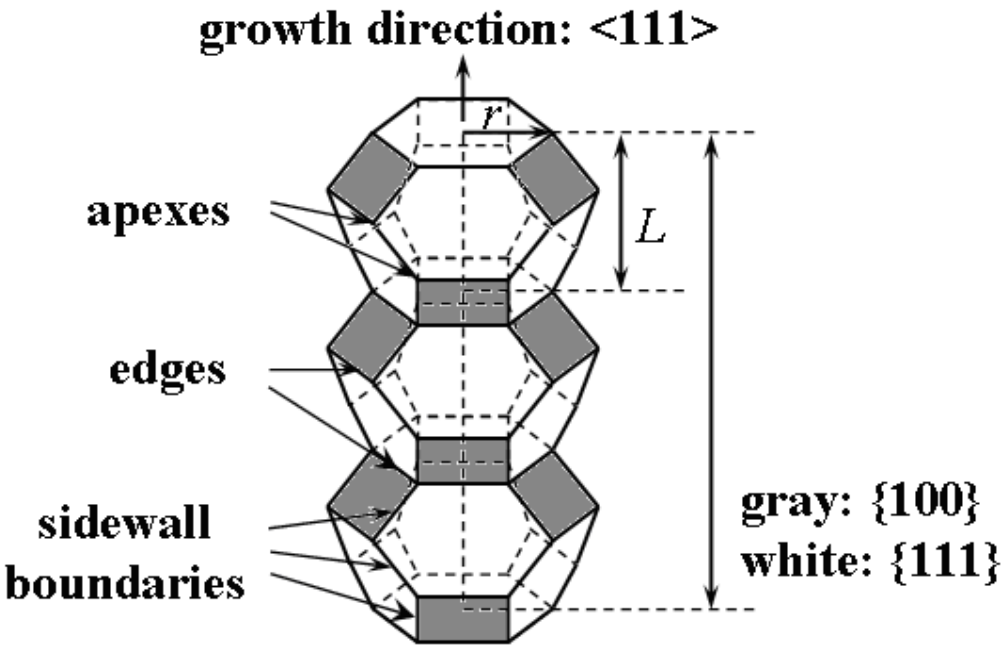


Figure 5.13 Schematic of the 3D structure of a <111>-oriented axial heterostructured *p-n-i* SiNW with sidewall nanofaceting in the *p*-type (B-doped) region. The edges, apexes and sidewall boundaries in the model are indicated.

The third term in Equation 5.3, $E_{elastic}$, describes the elastic relaxations of the surface: when alternating facets coexist on the surface, neighbouring facets have different values of the intrinsic surface stress tensor σ_1 and σ_2 (Figure 5.14). Due to this intrinsic surface stress tensor discontinuity, effective elastic forces, *F*, are created at the edges between two adjacent facets (as displayed in Figure 5.14). These forces generate the strain field that affects significantly the energetics of faceted surfaces and promotes the formation of a periodic structure of facets.[188] Following Alerhand *et al.*,[189] the elastic strain field is generated by the linear crystal edges, and the elastic relaxation energy depends on the period *L*:

$$E_{elastic} = -\frac{g}{L}\ln(\frac{L}{b\pi}) \tag{5.6}$$

where b is the lattice constant of Si, and g is a quantity calculated from the Young's modulus Y, the Poisson's ration ν, and the intrinsic surface stress tensor σ, and

$$g = \frac{c_5(1-\nu^2)\sigma^2}{Y} \tag{5.7}$$

where c_5 is a geometric factor which depends on the particular symmetry of the tensor and the magnitude of elastic anisotropy of the crystal.[188]

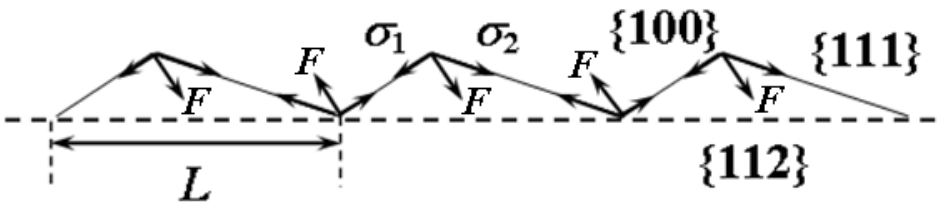


Figure 5.14 Schematic of the 2D periodic nanofaceting occurred on a SiNW sidewall surface. Effective elastic forces due to surface stress tensor discontinuity appear at edges.

By substituting Equations 5.4~5.6 into Equation 5.3, one obtains the following expression for the free energy of the faceted nanowire surface per unit projected area:

$$f = (c_1\gamma^0_{\{111\}} + c_2\gamma^0_{\{100\}}) + [2\frac{\eta}{L} + 2\frac{B}{rL} + (\frac{2c_3\eta_1 + c_4\eta_2}{r})] - \frac{g}{L}\ln(\frac{L}{b\pi}) \tag{5.8}$$

f has a minimum ($\frac{df}{dL} = 0$) when the period of faceting L is

$$L = b\pi\exp(2\frac{\eta}{g} + 1 + \frac{4B}{g2r}) \tag{5.9}$$

As seen from Equation 5.9, only the term in the argument of the exponential that arises from the apex energy B is dependent on wire diameter, $2r$, and becomes

increasingly important at small diameters, such as in a nanowire system. The facet period L is a function of the wire diameter $2r$, and L decreases as the wire diameter increases. This prediction from the model is in accordance with the experimental observation [Figure 5.12(e)]. The solid line in Figure 5.15 shows the fitting of the experimental data [Figure 5.12(e)] to Equation 5.9 using the Microcal™ Origin 6.0 software.

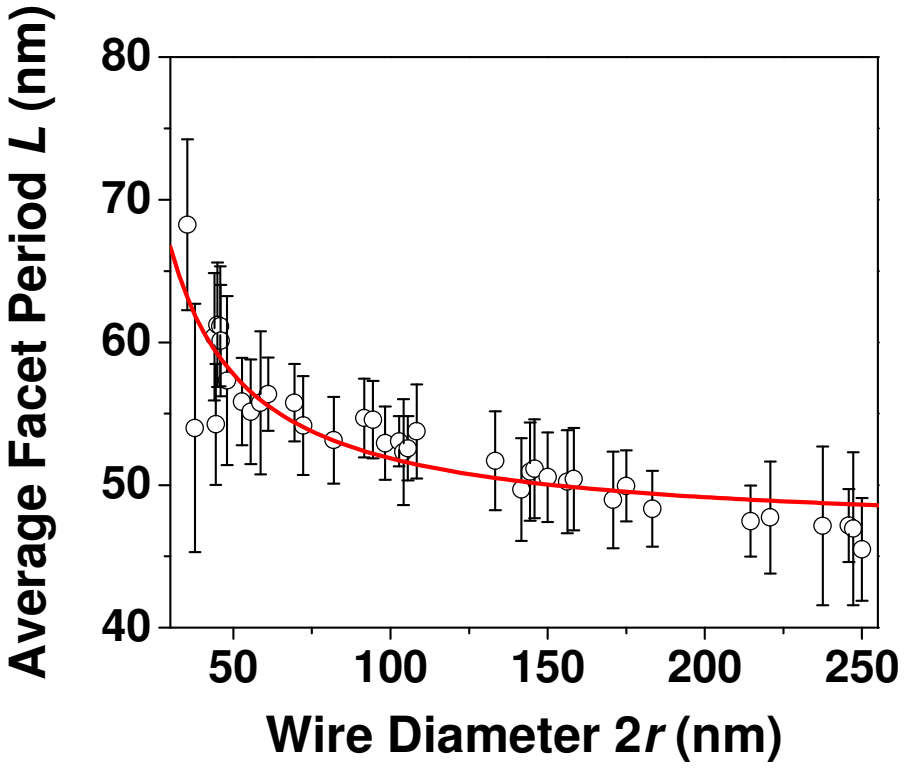


Figure 5.15 The dependence of average facet period on the wire diameter of the <111>-oriented axial heterostructured *p-n-i* SiNWs in the faceted *p*-type (B-doped) region. The solid line through the data points is the nonlinear least-square fit to Equation 5.9.

The relationships derived from fitting are

$$\frac{\eta}{g} = 1.153 \pm 0.006 \tag{5.10}$$

$$\frac{B}{g} = 26.8 \pm 2.0 \text{ Å} \tag{5.11}$$

The possible values of g can be evaluated from Equation 5.7 by calculating the surface stress tensor with the Young's modulus and Poisson's ratio of Si measured under the different measurement conditions,[190, 191] and g is in the range of 0.009~0.011 eV/Å. Therefore, the ranges of the values of edge energy η and apex energy B can be calculated from Equations 5.10 and 5.11, respectively. Table 5.1 compares the calculated values of the edge energy η and apex energy B with the corresponding reported values in the literature. It is seen that these values derived from fitting are within the ranges of previously reported values.

Table 5.1 Values of the edge energy and the apex energy.

	calculated values	**reported values**
edge energy η (eV/Å)	$0.01038 \pm (5\times10^{-5}) \sim 0.01268 \pm (7\times10^{-5})$	0.001~0.024[192,193]
apex energy B (eV)	$0.24 \pm 0.02 \sim 0.29 \pm 0.02$	0.06~0.3[190]

The observed (as well as predicted) dependence of facet period on wire diameter is different from the linear relationship observed experimentally by Ross *et al.*[161] in the *in situ* TEM observation of the nanofaceting on intrinsic SiNW surfaces during UHV-VLS growth. The difference is likely to be due to the different mechanisms of the nanowire growth and facet formation. Ross *et al.*[161] interpreted the faceting they

observed as resulting from the interplay of the geometry and surface energies of the wire and liquid droplet. In the work presented here, heterostructured SiNWs with axially varying doping were not grown under UHV conditions, and the nanofaceting occurs during the enhanced sidewall growth that arises when the B_2H_6 dopant gas is introduced, rather than from instabilities in the liquid droplet at the primary growth front, as suggested in Ross's model.[161] As such, the theoretical model presented here describes the thermodynamic equilibrium structure with a term arising from apex energy that becomes significant on surfaces with nanoscale radii of curvature. The nanofaceting occurs on the SiNW sidewalls during the enhanced vapour-solid growth when the B_2H_6 dopant gas is introduced, and is therefore not kinetically constrained. It is also likely that the stress induced by the boron impurities enhances surface diffusion allowing a large amount of mass transport at the surface.

Here the model has been developed assuming a regular hexagonal cross section for the nanowires. The HRSEM image in Figure 5.5 shows that this is a reasonable approximation for the nanowires in the present study. Truncated hexagons have also been observed under different growth conditions.[161] The theoretical model presented here can be readily adapted to truncated hexagon cross sections by noting that the hexagon sides, while still being proportional to *r*, are not exactly equal to *r*.

In addition, it is emphasized that this model may not apply to SiNWs with very small diameters. In this work, no SiNWs with diameters less than 30 nm were synthesized,

thus it is not known if the nanofaceting occurs on the sidewalls of these thin SiNWs. However, it can be foreseen that the nanofaceting (if there are any) on small-diameter nanowire sidewalls would be different from that on large-diameter nanowire sidewalls. Firstly, the growth behaviour of ultra-thin nanowires (diameter < 10 nm) has been suggested to be different from the classical VLS growth of large-diameter nanowires.[194] If nanofacets do occur on the sidewalls of such ultra-thin nanowires, a different faceting model should come into play. Secondly, the growth direction of the VLS-grown SiNWs depends strongly on the wire diameter, *i.e.*, the small-diameter (< ~20 nm) SiNWs are <110> oriented, while SiNWs with diameters larger than 40 nm normally grow along <111>, and those with intermediate diameters grow along <112>.[147] For nanowires growing in different directions, the shapes of the cross section as well as the sidewall orientations are different. Therefore, the nanofacets (if there are any) occurring on the sidewalls of non-<111> oriented SiNWs will be different from those on the <111>-oriented SiNW sidewalls. A different faceting mechanism will apply to SiNWs in the small-diameter region.

5.5 Chapter Summary

The surface morphology of the VLS-grown axial heterostructured SiNWs with varying doping were studied using various EM techniques. The SiNW sidewalls exhibit nanoscale periodic faceting, which is strongly doping dependent, *i.e.*, sidewall faceting occurs in the *p*-type (boron-doped) region, while both the *n*-type

(phosphorus-doped) and the intrinsic SiNW regions exhibit smooth surface morphology. The nanowires are axially oriented along <111>, and the crystallographic planes on which the nanofaceting occurs are Si{111} and {100}. The nanofaceting occurs during the enhanced sidewall growth that arises when the B_2H_6 dopant gas is introduced for the *p*-type doping of SiNWs. A thermodynamic model predicting the facet period of nanowire sidewall faceting is developed. An extra energy cost term arising from the formation of apexes between facets on nanowire sidewalls is considered, and the nanofacet size is predicted to decrease as the wire diameter increases. The model fits the experimental data well, and the fitted parameters in the model lie within the ranges of their expected values.

Chapter 6

Indium Nitride Colloidal Nanoparticles

6.1 Introduction

Indium nitride (InN) is an important group III-V semiconductor which can be used in many optoelectronic devices, such as LEDs and laser diodes.[86] In particular, free-standing InN colloidal nanoparticles are expected to exhibit a larger band gap than bulk InN by the size reduction, making it possible to extend the emission of the InN-based LEDs. However, due to the challenges in chemical synthesis and the instability of InN (low bulk dissociation temperature of 500~550 °C),[83,84,85] reports on successful solution-phase synthesis of InN colloidal nanoparticles are scarce. In addition, many fundamental microstructural and optical properties of InN colloidal nanoparticles, such as crystalline structures, chemical compositions and optical band gap, have not been extensively studied.

6.1.1 Crystalline Structures

Bulk InN crystallizes into two different structures, the hexagonal (wurtzite) which is its stable form and the cubic (zincblende) which is the metastable form. In both structures, each indium atom is coordinated by four nitrogen atoms. Conversely, each nitrogen atom is coordinated by four indium atoms. The main difference between the hexagonal (wurtzite) and the cubic (zincblende) structures is in the stacking sequence of closest packed diatomic planes. The theoretical lattice parameters for hexagonal (wurtzite) InN scatter in the ranges of $a = b = 3.501 \sim 3.536$ Å and $c = 5.540 \sim 5.709$ Å, and the theoretical reported values of the lattice constant for cubic (zincblende) InN are in the range of 4.92~4.98 Å.[195] Under pressure, InN transforms to a rocksalt structure (cubic, $a = 4.57$ Å).[196,197,198]

For the InN films, most of the publications reported the formation of hexagonal (wurtzite) phase, but the cubic (zincblende) structure of InN has also been occasionally reported.[199,200,201] In the case of the InN colloidal nanoparticles grown in solution, Bai *et al.*[99] reported that the two phases of cubic InN and hexagonal InN coexist in the nanoparticles prepared by the solvo-thermal method. The average sizes are approximately 30 nm and 27 nm for the cubic InN and hexagonal InN nanoparticles, respectively. Apart from the 0D InN nanoparticles, they also observed 2D nanosheets and 1D nanorods with a cubic crystalline structure, and suggested that these 1D and 2D InN nanostructures are grown from the aggregation of the unstable

cubic InN nanoparticles.[99] Sardar *et al.*[100] synthesized the hexagonal InN colloidal nanoparticles with an average size of 10~15 nm. The hexagonal InN colloidal nanoparticles synthesized by Greenberg *et al.*[102] exhibit the sphere-like or cube-like shapes. The nanocrystalline InN prepared by Xiao *et al.*[103] has rod-like and plate-like morphologies, where numerous 10~30 nm hexagonal structured crystallites aggregate together. Schofield *et al.*[104] reported the 2~10 nm InN nanoparticles synthesized exhibit a cubic crystalline structure.

6.1.2 Chemical Compositions

For bulk InN, the stoichiometry between indium and nitrogen is a topic of two separate debates. The indium-rich debate originates from the nitrogen loss at higher growth temperatures, where the thermal decomposition is more likely.[202] On the other hand, the nitrogen-rich debate suggests that for non-equilibrium growth techniques such as RF sputtering and MBE, excess nitrogen incorporation occurs more readily at lower growth temperatures.[203] Butcher *et al.*[204,205] showed that the stoichiometry of InN films can sometimes be far from unity (In_xN_y with varying compositions, $x \neq y$).

In addition, indium strongly chemisorbs molecular O_2, but it does not chemisorb molecular N_2, only atomic nitrogen.[206] Hence, surface oxidation and degradation after aging in air is a contentious problem for InN-based devices. Foley *et al.*[207]

pointed out that at the first stage of oxidation is the formation of a type of In-N-O complex. Kurimoto *et al*.[208] suggested that aged InN films consist at the beginning of a mixing of InN:O (InN heavily doped with oxygen) and In_2O_3 phases and finally is completed with totally changing into In_2O_3. InN films have been known to suffer from considerable oxidation at the surface.[209,210]

In the case of InN nanoparticles, Kwon *et al*.[211] observed the formation of In_2O_3 precipitates in InN quantum dots grown on GaN substrates during the MOCVD growth and/or subsequent postgrowth in H_2 ambient. González *et al*.[212] reported that the MOVPE-grown InN quantum dots on GaN/Al_2O_3 substrates undergo a natural aging process under ambient conditions by oxygen incorporation. However, the aging process of InN colloidal nanoparticles chemically synthesized in a solution is not known, due to the lack of reports on successful syntheses.

6.1.3 Optical Properties

InN is a direct band gap group III-V semiconductor. The band gap E_g of InN has been a longstanding controversy in the literature and the stoichiometry can be one of the sources of the controversy. Early absorption studies on InN polycrystalline films grown by direct current (DC)-discharge,[213] cathodic sputtering[214] and RF sputtering,[215] have suggested a band gap $E_g = 1.8 \sim 2.0$ eV at room temperature. Recently, with the realization of high quality InN film, several research groups have

reported that the band gap energy of InN is to be around 0.65~0.9 eV,[216,217,218] and argued that the previously accepted high band gap values are due to the poor sample quality and oxygen contamination. However, some others still believed that the band gap of InN is around 1.89 eV as reported before, and claimed that the newly-reported narrow band gap may be due to the defect level emission, although the current progress seems to lead to the conclusion that the optical band gap energy of InN is near ~0.7 eV.[219]

For the InN colloidal nanoparticles grown in a solution, Sardar *et al*.[100] showed that the optical absorption spectrum of the hexagonal InN colloidal nanoparticles reveals a well-defined absorption band at ~1575 nm (0.8 eV). However, no compositional properties of these nanoparticles were studied. Photoluminescence (PL) measurement of the hexagonal InN colloidal nanoparticles by Greenberg *et al*.[102] showed a PL peak at ~505 nm (2.5 eV), which they tentatively ascribed to the emission from defects and surface states in the nanoparticles. Xiao *et al*.[103] observed a broad PL peak at 2.2 eV for the hexagonal InN crystallites synthesized using a benzene thermal conversion approach. Schofield *et al*.[104] reported a broad emission centred at 690 nm (1.8 eV) for the cubic InN nanopaticles synthesized by the decomposition of $InN_3(CH_2CH_2CH_2NMe_2)_2$ in trioctylphosphine oxide and toluene.

In this work, a well designed chemical method has been innovated by the industrial collaborators to prepare the InN colloidal nanoparticles with different sizes and size

distributions by simply controlling the solution-phase reaction time. Figure 6.1 shows the PL measurements carried out by the industrial collaborators, for InN colloidal nanoparticles grown for 10, 20 and 30 minutes in solution. The emission bands are centred at around 536, 675 and 730 nm for the InN colloidal nanoparticles grown for 10, 20 and 30 minutes, respectively. It is seen that the harvested colloidal nanoparticles exhibit a massive blueshift of the band gap energy, as compared with bulk InN (0.7 eV, PL emission band at 1771 nm).

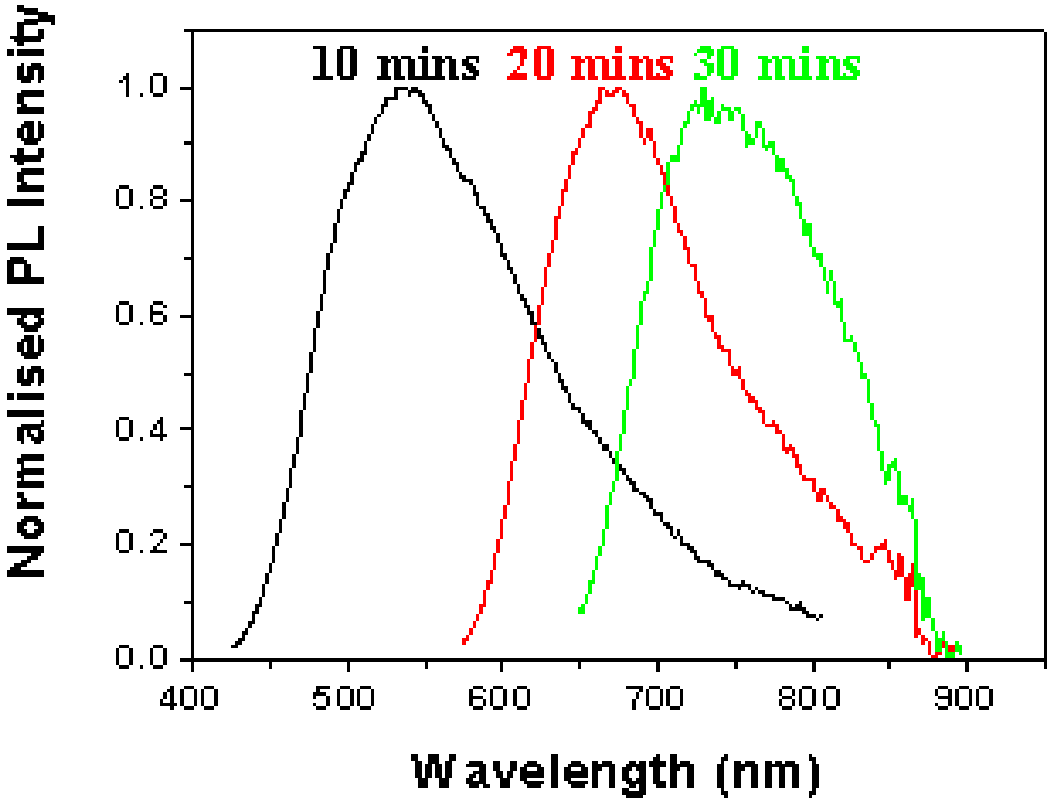


Figure 6.1 Photoluminescence spectra of the InN colloidal nanoparticles grown for 10, 20 and 30 minutes in solution, respectively (data from industrial collaborators).

However, the physical origins of the band gap blueshift in the colloidal nanoparticles

synthesized in this work are not known. To answer these questions, it is required (i) to examine the shape, crystalline structures and compositions of the harvested materials and to check if they are InN colloidal nanoparticles; and (ii) to understand the dependence of optical band gap energy on the size reduction and the effects of particle size distribution on PL spectra. These are the purposes of this chapter.

6.2 Results and Discussion

6.2.1 Confirmation of the Formation of Indium Nitride Colloidal Nanoparticles

To check the formation of the InN colloidal nanoparticles in the solution-phase synthesis, it is necessary to examine the compositions, crystalline structures and shape of the as-grown colloidal nanoparticles. Here TEM combined with chemical analytical spectroscopy is a versatile tool that not only provides atomic-resolution lattice images, but also allows direct identification of the chemical information of nanoparticles. In this thesis, suspensions containing harvested colloidal nanoparticles were drop-cast on the TEM finder grids with a 20 nm thick holey carbon film, and the microstructural properties of the colloidal nanoparticles, including the compositions, crystalline structures and shape, were characterized using TEM, HRTEM, STEM and EDX techniques.

6.2.1.1 Compositions

One of the most direct methods to check the formation of the InN colloidal nanoparticles synthesized in this work is to identify the elements in the nanoparticles. Here energy dispersive X-ray spectroscopy (EDX) was employed to examine the compositions of the harvested colloidal nanoparticles. By using a fine electron probe, EDX spectra were acquired under the STEM mode. Figure 6.2(a) shows the STEM image of the high-density specimen of the InN colloidal nanoparticles on the carbon support film. Large (> 10 nm) nanoparticles as well as a large number of small-size (< ~5 nm) nanoparticles are observed. For the small-size nanoparticles, EDX spectra were acquired in the high-density region where numerous small-size InN nanoparticles are overlapped and agglomerated. For the large-size nanoparticles, EDX spectra were acquired by positioning the probe on the individual nanoparticle.

Figure 6.2(b) shows the EDX spectra of the large-size InN nanoparticle, the small-size nanoparticle agglomerates and the carbon support film on which the nanoparticles were deposited. Here the Cu and C signals come from the TEM grid with carbon film. The Si signal may come from the EDX detector or the Si contamination from the glassware used for reaction, because no Si-containing substance was added into solution during the synthesis. As seen from Figure 6.2(b), the large-size nanoparticles contain In, N, Zn and O. The small-size nanoparticle agglomerates also contain In and Zn, although there is an overlap of the C, N and O signals, the EDX spectrum still

shows a hint of the N signal. The carbon film on which the nanoparticles were deposited contains O and Zn.

Generally, colloidal nanoparticles are known to have an inorganic core that is stabilized by a layer of organic ligands. In this work, Zn-containing organic ligands were used as the capping layers of the InN colloidal nanoparticles. The presence of Zn and O in the nanoparticles and the carbon film is due to the Zn-containing organic capping layers, the residue of which was dissolved in the suspensions containing the InN nanoparticles. When preparing the TEM specimens, the suspension containing both InN nanoparticles and the residual ligands was drop-cast onto the carbon support film, giving an explanation for the presence of Zn and O in the specimens. There is also another possibility that the presence of O results from the surface oxidation of the InN nanoparticles.[211] The oxygen may exist as an amorphous indium oxynitride in the InN matrix, as previously suggested by Westra *et al*.[220] on the InN film.

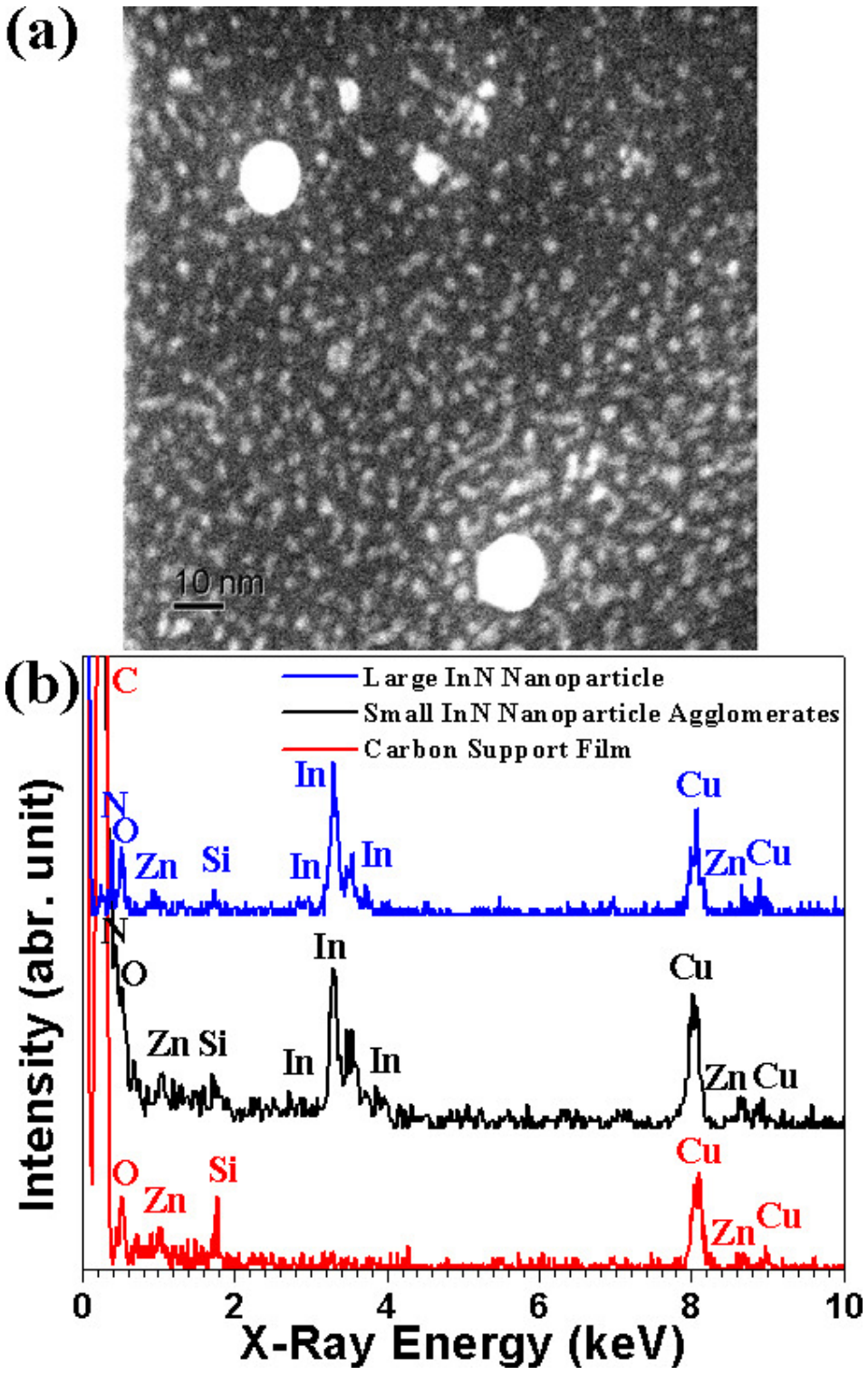


Figure 6.2 (a) STEM image showing the InN colloidal nanoparticles with different sizes; and (b) EDX spectra obtained from the large-size nanoparticle, small-size nanoparticle agglomerates and carbon support film.

6.2.1.2 Crystalline Structures

EDX characterization shows that the harvested colloidal nanoparticles contain In and N. To further confirm the formation of InN colloidal nanoparticles, their crystalline structures were examined using HRTEM with the calibrated magnification. This is because different materials exhibit different crystalline structures, and the interplanar spacings in different crystal structures are characteristic of that structure, thus determination of the crystalline structure of a material offers important information for identifying that material. Although crystalline structures of a material can be determined by X-ray and neutron diffraction, HRTEM is indispensable for the characterization of nanoscale particles, especially when the particle size and shape are important. This is because the crystalline structures for nanoparticles can be particle size dependent and different from that of the corresponding bulk material. For example, it has been previously predicted[221] that there exists a threshold nanoparticle size, below which the metastable phase of a semiconductor is stabilized. Therefore, it is necessary to investigate the crystalline structures of the colloidal nanoparticles synthesized in this work with different sizes. Here HRTEM is a powerful tool to study the crystalline structures of individual InN colloidal nanoparticles, if a low-density TEM specimen (nanoparticles with different sizes are well separated from each other) is prepared.

It is known that bulk InN crystallizes into two different structures, the hexagonal (wurtzite) which is its stable form and the cubic (zincblende) which is the metastable form. In this thesis, the crystalline structures of 88 colloidal nanoparticles synthesized were examined using HRTEM. Both the hexagonal (wurtzite) and the cubic (zincblende) structures are observed, and the crystalline structure of the InN colloidal nanoparticles is found to be particle size dependent.

Firstly, hexagonal (wurtzite) InN colloidal nanoparticles (20 out of 88) are observed in nanoparticles smaller than 7 nm. As an example shown in Figure 6.3(a), the HRTEM image shows a nanoparticle with a size of ~4 nm. The Fourier transform of the corresponding particle image [marked by the red square in Figure 6.3(a)] is shown in Figure 6.3(b). The ratios of the spot spacings as well as the angles between the plane normals in the FFT patterns were examined. The spots shown in the FFT in Figure 6.3(b) were found to correspond to the hexagonal structure with the $<2\bar{1}\bar{1}0>$ zone axis. Another HRTEM image and its corresponding Fourier transform of a ~5 nm nanoparticle are shown in Figure 6.3(c) and (d), respectively. The FFT patterns in Figure 6.3(d) were indexed by examining the ratios of the spot spacings and the angles between the plane normals of the patterns. The configurations shown in the FFT in Figure 6.3(d) correspond to the hexagonal structure with the $<01\bar{1}1>$ zone axis.

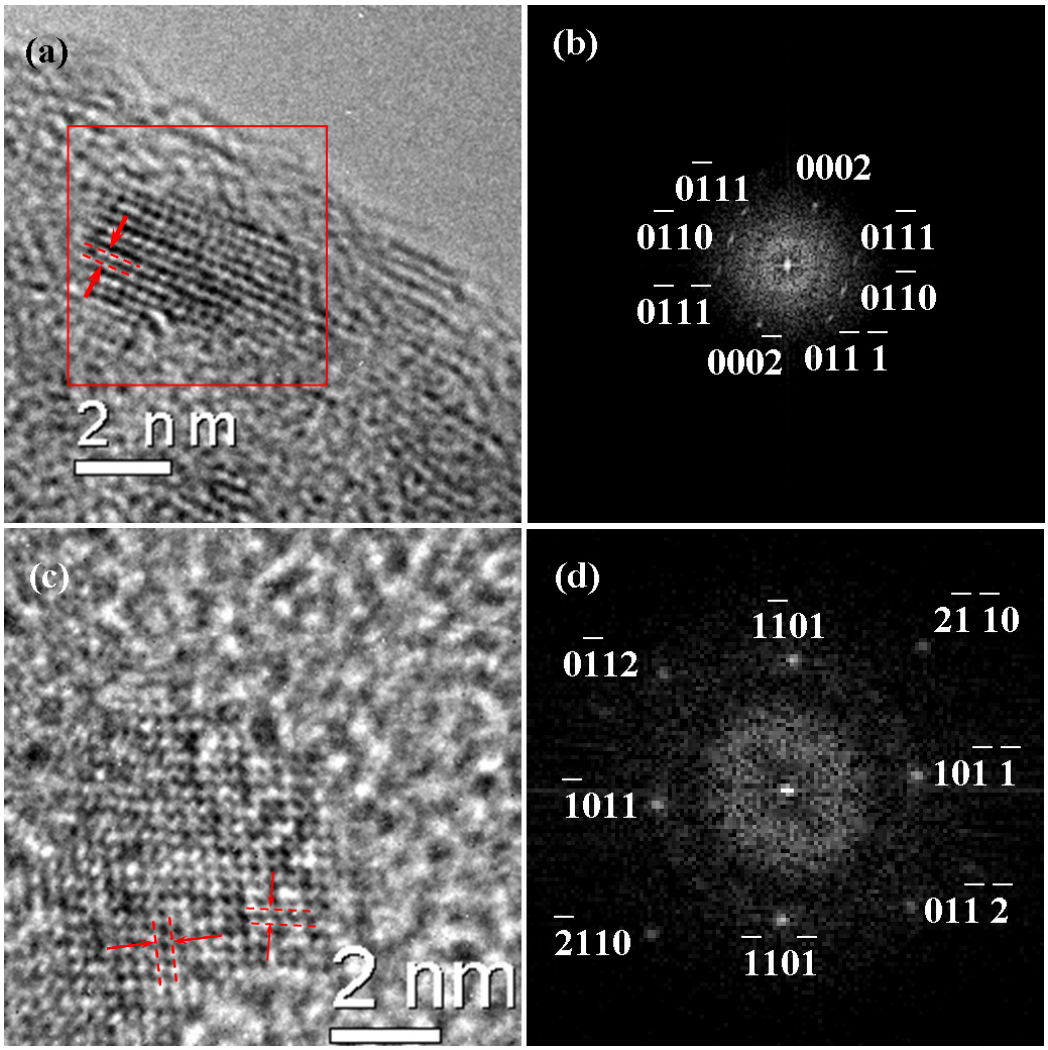


Figure 6.3 (a) HRTEM image of a ~4 nm InN colloidal nanoparticle; (b) Fourier transform of the localized image of the nanoparticle region marked by a red square in (a); (c) HRTEM image of a ~5 nm InN colloidal nanoparticle; and (d) Fourier transform of the image in (c).

The average lattice spacing of the colloidal nanoparticles was determined by obtaining several line profiles across groups of 10 successive lattice planes and by averaging over these periods (the number of line profiles obtained depends on the size of the nanoparticle). For accurate measurements, a standard reference specimen (intrinsic diamond cubic SiNW, Si{111} planes with a spacing of 3.14 Å) was used for the magnification calibration. The calibrated magnification was then used to

measure the interplanar distances of the InN colloidal nanoparticles at the same magnification value (displayed on the microscope), at which the calibration was carried out. An additional systematic error of 1% accuracy is present in the measurements as a result of the magnification calibrations performed on different days. The measured interplanar distances for the {0002} and $\{\bar{1}011\}$ planes [as indicated in Figure 6.3(a) and (c), respectively] are 2.82 ± 0.03 and 2.68 ± 0.02 Å, respectively. The lattice constants are calculated to be $a = b = 3.52 \pm 0.03$ Å, and $c = 5.64 \pm 0.06$ Å, which are in good agreement with the reported values of the hexagonal InN scattered in the ranges of $a = b = 3.501$~3.545 Å and $c = 5.540$~5.709 Å.[195]

Secondly, cubic (zincblende) InN colloidal nanoparticles are observed at different sizes. For example, Figure 6.4(a)~(c) show the HRTEM images of three nanoparticles with the sizes of ~5, ~7 nm and ~16 nm, respectively. The corresponding FFTs of the particle images [marked by red squares in Figure 6.4(a) and (b), respectively] are shown as insets in Figure 6.4(a) and (b), respectively, and the Fourier transform of Figure 6.4(c) is shown in Figure 6.4(d). All these FFTs show a pattern which is characteristic of an fcc material in the <110> zone axis. The average lattice spacing of these cubic (zincblende) InN colloidal nanoparticles was determined following the same procedures stated above. The measured lattice spacing for the {111} planes is 2.86 ± 0.02 Å, and the lattice constant is calculated to be 4.95 ± 0.03 Å. It matches well with the cubic (zincblende) InN with the lattice constant of 4.92~4.98 Å.[195]

Here InN colloidal nanoparticles with hexagonal (wurtzite) crystalline structure are observed in nanoparticles smaller than 7 nm, while the cubic (zincblende) ones are found not only in < 7 nm nanoparticles, but also in those larger than 7 nm. Therefore, cubic (zincblende) InN colloidal nanoparticles exhibit larger sizes than the hexagonal (wurtzite) ones. A similar observation has been previously reported for the InN nanocrystals by Bai *et al*,[99] who suggested that cubic (zincblende) InN nanocrystals are liable to grow into larger dimensions.

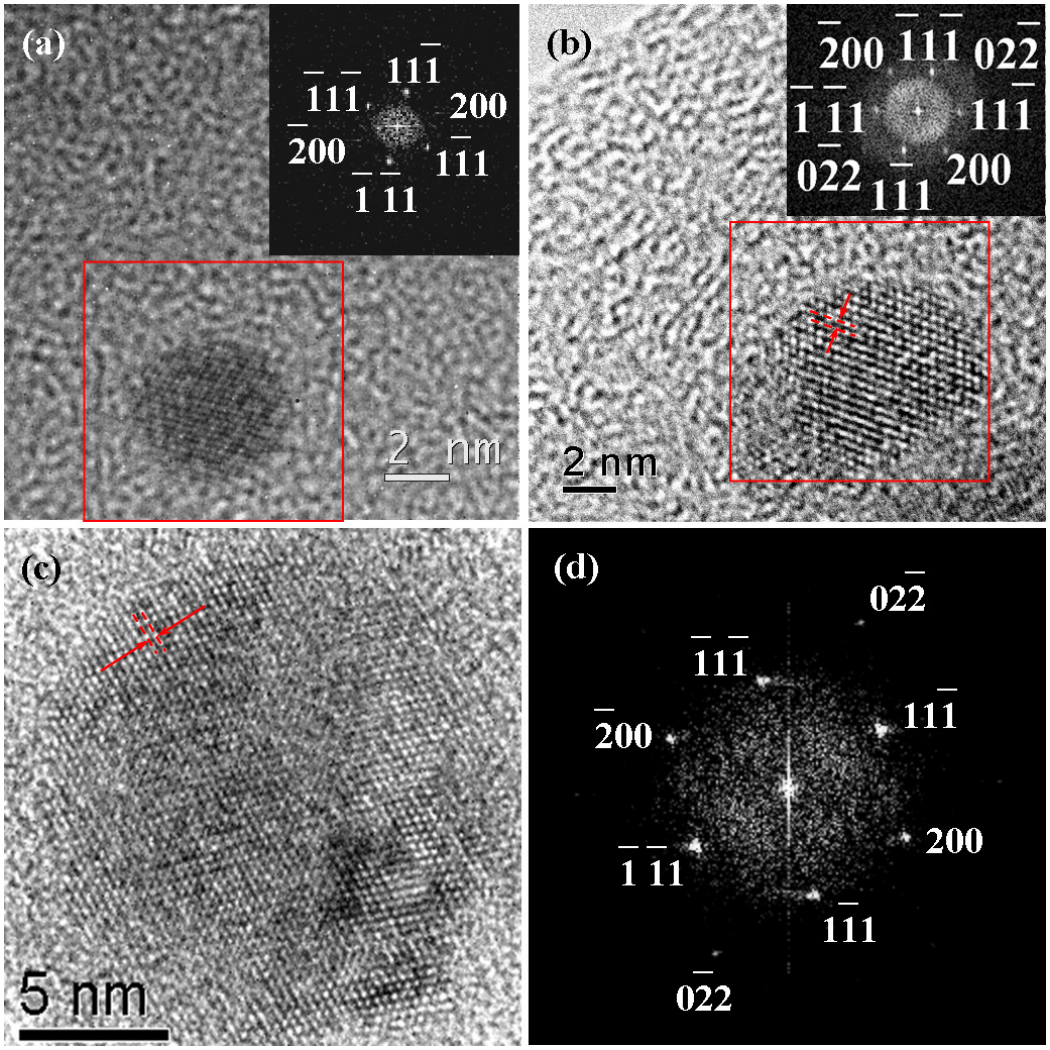


Figure 6.4 HRTEM images of (a) a ~5 nm and (b) a ~7 nm InN colloidal nanoparticles, insets in (a) and (b) are the corresponding Fourier transforms of the particle images (marked by red squares); (c) HRTEM image of a ~16 nm InN colloidal nanoparticle; and (d) the Fourier transform of the image in (c).

Thirdly, in large-size (> 7 nm) nanoparticles, significant amounts of defects are frequently observed. As an example shown in Figure 6.5(a), stacking faults, twins as well as changes in crystalline structure between the cubic (zincblende) and the hexagonal (wurtzite) phases are observed in a ~25 nm InN colloidal nanoparticle. Figure 6.5(b) is the image of the same nanoparticle taken at low magnification. In Figure 6.5(a), the interfaces between stacking faults, twins and different crystalline

structures are indicated by dashed lines. The crystallographic analysis shows that the regions separated by these interfaces have different crystalline structures. For example, Figure 6.5(c) and (d) correspond to the FFTs of the localized images in the regions I and II [marked by red squares in Figure 6.5(a)], respectively. The ratios of the spot spacings as well as the angles between the plane normals in the FFT patterns were examined. It is found that the spots shown in the FFTs of the regions I and II correspond to the hexagonal $<2\bar{1}\bar{1}0>$ [Figure 6.5(c)] and the fcc <110> zone axes [Figure 6.5(d)], respectively. Thus the region I of the nanoparticle has the hexagonal (wurtzite) structure, while the region II is cubic (zincblende). Regions of cubic (zincblende) and hexagonal (wurtzite) InN alternate with the following epitaxial relationship: $\{111\}_{\text{zincblende}} \parallel \{0002\}_{\text{wurtzite}}$.

However, evident microstructural defects are seldom observed in both the hexagonal (wurtzite) and the cubic (zincblende) InN colloidal nanoparticles with sizes smaller than 7 nm. A similar observation has been previously reported on silicon nanocrystals.[222] Theoretical prediction[223] suggests that dislocations and line defects are unstable within crystallites of dimensions smaller than a specific size, because in small nanoparticles, the residual strain arising from volume contraction during crystallization is smaller, and it can be more easily adjusted by the elasticity. Defects only need to travel small distances to reach the surface and disappear. However, the difficulty associated with moving a defect out of a nanoparticle will increase rapidly with increased particle size.[222]

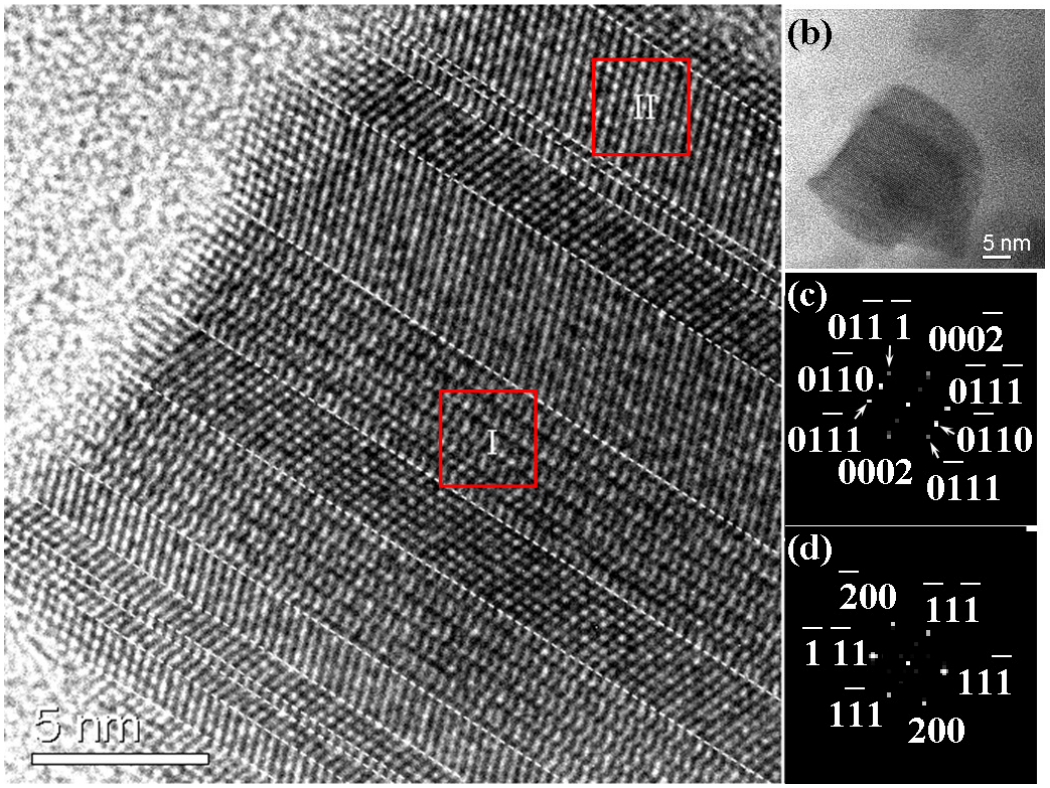


Figure 6.5 (a) HRTEM image showing the defects in an InN nanoparticle, numbers 'I' and 'II' are assigned to different regions of the nanoparticle; (b) image of the same nanoparticle in (a) taken at low magnification; (c) and (d) are the corresponding Fourier transforms of the localized images of the regions I and II [marked by red squares in (a)], respectively.

6.2.1.3 Shape

Colloidal nanoparticles commonly exhibit a 0D sphere shape.[224] However, a kinetic shape-controlling nanocrystal growth mechanism[98] suggested that a high growth rate results in a variety of highly anisotropic shapes, including 1D rods, 2D discs and 3D complex structures, while a slow growth rate produces equilibrated and nearly spherical nanoparticles (this mechanism has been applied to the shape control of a variety of colloidal nanocrystal systems[225, 226, 227]). The shape of colloidal nanoparticles plays an important parameter in the determination of their properties.[228]

Therefore, the shape of the InN colloidal nanoparticles was examined before discussing their physical properties. Here TEM was employed to characterize the shape of the InN colloidal nanoparticles synthesized. Figure 6.6(a) shows a typical TEM image of the harvested InN colloidal nanoparticles deposited on the carbon support film. It is seen that the nanoparticles are well separated from each other and have a nearly "spherical" shape. However, one should note that the TEM image shown in Figure 6.6(a) is only a 2D projection image, which contains little or no information on the thickness of samples. In 3D [Figure 6.6(b)], the nanoparticles may have different shapes, such as 0D spheres or 2D discs.

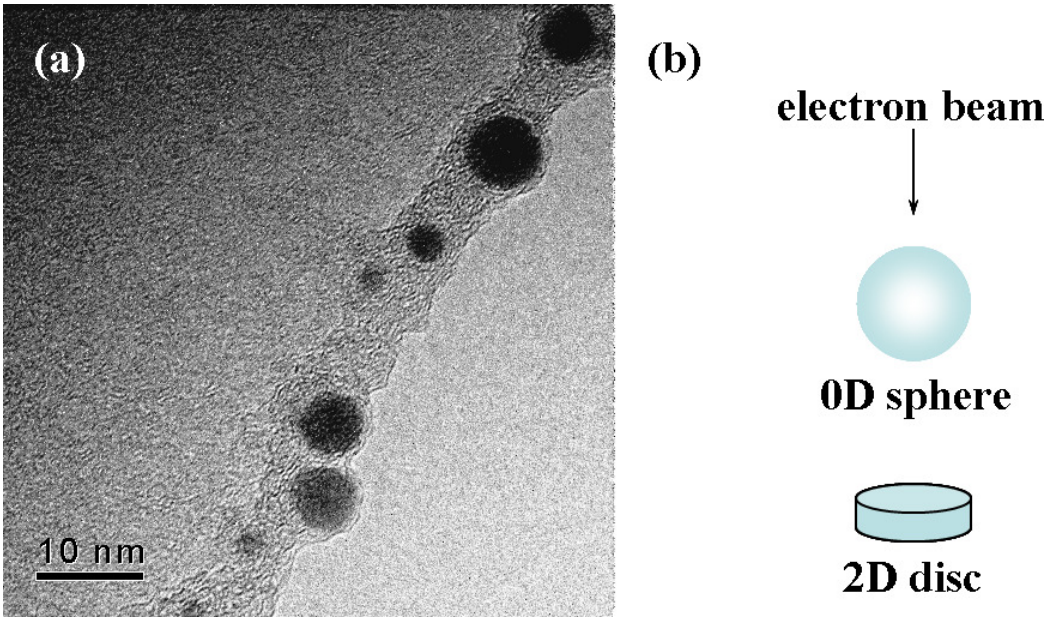


Figure 6.6 (a) TEM image of the InN colloidal nanoparticles deposited on the holey carbon support film; and (b) schematic of the possible shapes in 3D.

Here HAADF-STEM was used to further characterize the colloidal nanoparticles. Because in STEM, the HAADF signal increases with atomic number (hence the mass)

and sample thickness. For nanoparticles of the same average mass, thicker regions in nanoparticles will scatter more electrons than thinner regions, all other factors being constant (thicker areas will appear brighter than thinner areas in HAADF-STEM images), so the HAADF contrast can be used to qualitatively determine the thickness of nanoparticles, offering some information on their 3D shapes.

Figure 6.7(a) shows an HAADF-STEM image of an InN colloidal nanoparticle. Figure 6.7(b) shows the HAADF-STEM intensity profiles across two lines aa' and bb' [dashed lines in Figure 6.7(a)] over the nanoparticle. In Figure 6.7(c), the same image in Figure 6.7(a) is plotted in a 3D perspective. It is seen that the HAADF intensity increases gradually from the particle edges and reaches to a maximum at the central area of the nanoparticle. Qualitative argument indicates that the nanoparticle is thickest at the centre, and the thickness decreases gradually from the centre to the particle edge. Therefore, the 2D disc shape can be ruled out, as the thickness of the disc is constant [see Figure 6.6(b)]. It is believed that the colloidal nanoparticles observed in this thesis have a near-spherical shape.

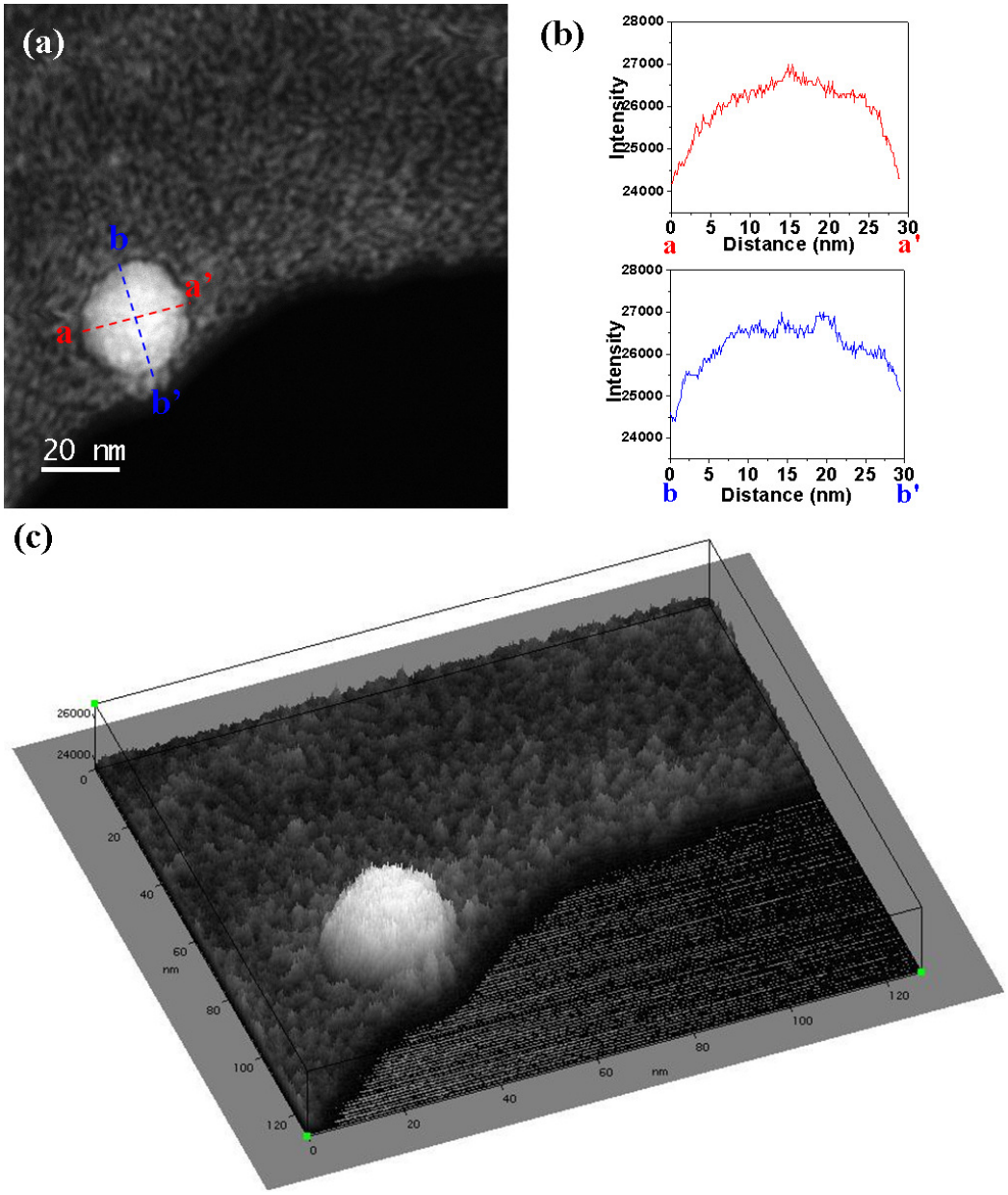


Figure 6.7 (a) HAADF-STEM image showing an InN colloidal nanoparticle; (b) HAADF-STEM intensity profiles across two dashed lines aa' and bb' in (a) over the nanoparticle; and (c) the same image as in (a) in pseudo 3D graphics.

6.2.2 Size-dependent Optical Properties

6.2.2.1 Particle Size and Size Distribution

The physical and chemical properties of colloidal nanoparticles are strongly affected not only by the particle shape, crystalline structures and composition, but also by the size of the nanoparticles. It is known that the most striking property of semiconductor nanoparticles is the massive changes in optical properties as a function of the size.[229] Therefore, the size of the InN colloidal nanoparticles need to be examined before studying their optical properties. In particular, control of the size of colloidal semiconductor nanoparticles through synthesis has significant implications for the utilization of their size-dependent properties. A simple way to manipulate the colloidal nanoparticle size is to control the time of solution-phase reactions. In this thesis, the effects of solution-phase reaction time on the size and size distribution of the InN colloidal nanoparticles were studied. A well designed wet-chemistry method was used by the industrial collaborators to synthesize the InN colloidal nanoparticles. Three InN colloidal nanoparticle specimens with different particle sizes and size distributions were obtained by keeping the chemical reaction for 10, 20 and 30 minutes in solution, respectively. In addition, as shown at the beginning of this chapter, these three colloidal nanoparticle specimens exhibit different band gap upshifts (Figure 6.1). Therefore, to understand the size-dependent optical properties of the InN colloidal nanoparticles, the particle size and size distribution were examined.

Here the TEM technique was employed to examine the size of the InN colloidal nanoparticles synthesized. The average size and size distribution of each InN colloidal nanoparticle specimen were determined using HRTEM by measuring 400 nanoparticles from each specimen. Magnification calibration of the HRTEM micrograph followed the same procedures stated above, and the calibrated magnification was then used to measure the size of nanoparticles at the same magnification (displayed on the microscope), at which the calibration was carried out. An additional systematic error of 1% accuracy is present in the measurements as a result of the magnification calibrations performed on different days. The diameter of a spherical nanoparticle was determined by obtaining the line profile [with the program DigitalMicrograph (Gatan, version 3.6.5)] across HRTEM fringes between two edges on the nanoparticle which are diametrically opposite. In the case of very small nanoparticles, where HRTEM is unlikely to reveal their lattice fringes (in this thesis, for the InN colloidal nanoparticles with sizes smaller than 3 nm, direct HRTEM structure determination was not achieved due to the small size of the nanoparticles and the increased instabilities of InN with reduced sizes), the location of the particle boundary was determined by observing the abrupt change in intensity between the particle and the carbon support film. One should note that there is some uncertainty in identifying the exact position of the particle boundary, although the uncertainty is small (1%) since the abrupt change in contrast is confined to a narrow range of radii.

Figure 6.8(a)~(c) show typical TEM images of the InN colloidal nanoparticles grown for 10, 20 and 30 minutes in solution, respectively. It is seen that the nanoparticles are free of agglomeration, and most of them are spherical in shape. Only a small fraction of nanoparticles deviate from a regular spherical shape by being elongated in one direction, or by exhibiting faceted surfaces [as an example shown in the inset in Figure 6.8(c)]. For those nanoparticles without a regular spherical shape, typically the maximum measurement length across the nanoparticle is measured for statistical analysis.[230,231]

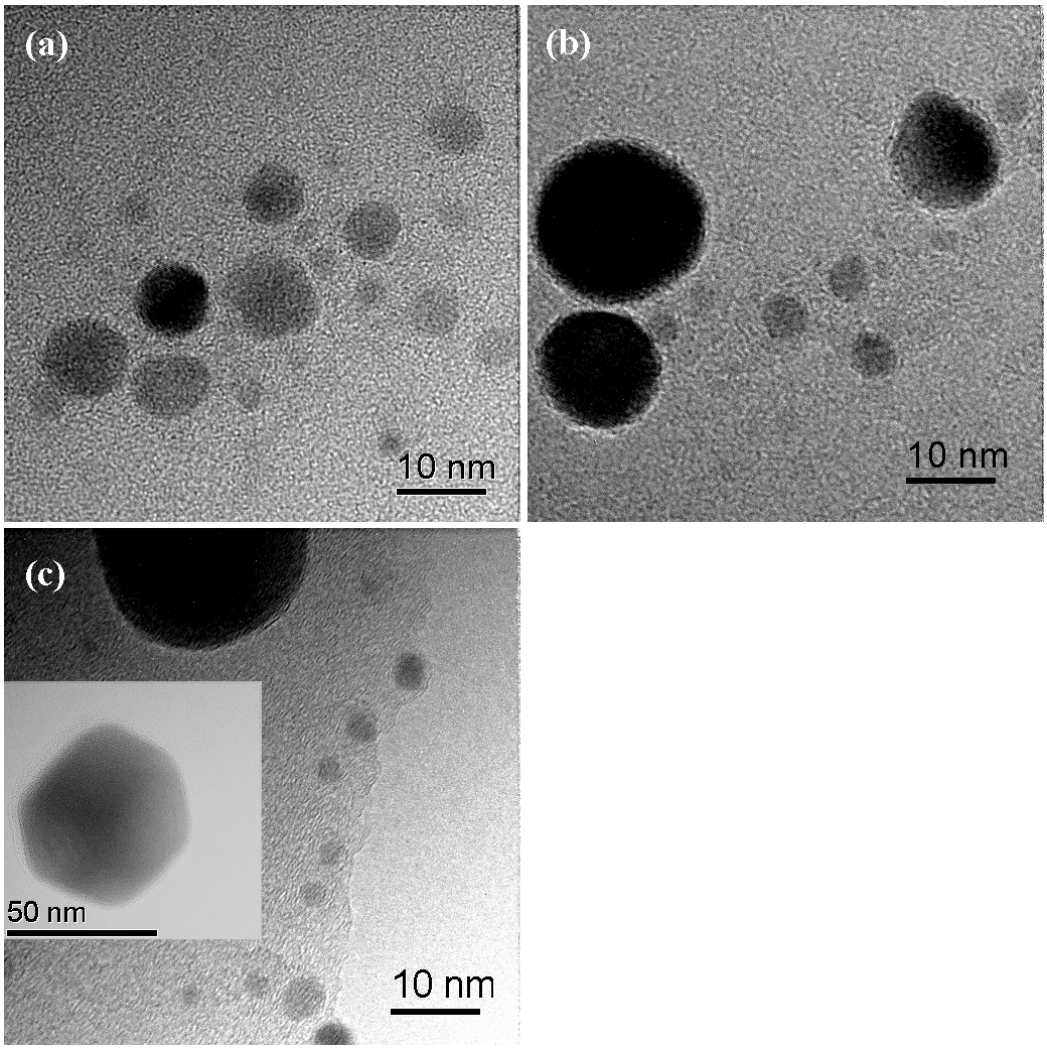


Figure 6.8 TEM images of the InN colloidal nanoparticles grown for (a) 10 minutes; (b) 20 minutes; and (c) 30 minutes in solution. Inset in (c): TEM image of an InN colloidal nanoparticle with a size larger than 50 nm observed in the specimen grown for 30 minutes.

Figure 6.9(a), (b) and (c) show the size histograms of the InN colloidal nanoparticles grown for 10, 20 and 30 minutes in solution, respectively. It is seen that the particle size distribution becomes broader with prolonged reaction time. For each specimen, the particle size distribution determined from the TEM images exhibits two peaks, each of which exhibits a Gaussian-like shape: there is a sharp peak in the small particle size region (< 6 nm), and a broader peak in the large-size region. It indicates

that in all InN colloidal nanoparticle specimens, a large majority of nanoparticles exhibit sizes smaller than 6 nm. Insets in Figure 6.9(a)~(c) are the corresponding histograms in the small-size region (< 6 nm), for the InN colloidal nanoparticles grown for 10, 20 and 30 minutes in solution, respectively. It is seen that as the reaction time is prolonged, the sizes of the two populations of nanoparticles all increase, and those larger nanoparticles grow faster than the smaller ones. In this thesis, experimental observation shows that

(i) Both the hexagonal and cubic InN colloidal nanoparticles are observed with the sizes of 4~5 nm [Figure 6.3 and Figure 6.4(a)].

(ii) A cubic (zincblende) structure is observed in the InN colloidal nanoparticles larger than ~7 nm while no nanoparticles larger than ~7 nm exhibit a pure hexagonal (wurtzite) phase [Figure 6.4 and 6.5]. Significant amount of defects, including stacking faults, twins, and crystalline structure changes between the cubic (zincblende) and the hexagonal (wurtzite) phases are observed in large-size (> 7 nm) InN colloidal nanoparticles (Figure 6.6).

It is thus assumed that the small-size (< 6 nm, the sharp peak in the histogram) nanoparticles are mainly hexagonal and cubic InN, while those with larger sizes (the broader peak) consist of both the cubic InN nanoparticles and defective ones.

The centres of the size distribution and the standard deviations were determined from fitting. Here the Microcal^{TM} Origin 6.0 software was used to fit each size distribution

plot in Figure 6.9, and a superposed Gaussian model containing two Gaussian peaks has the best fit to each size histogram. The green-colour solid lines in each histogram in Figure 6.9 show the individual Gaussian fits and the blue-colour lines are the fittings to the superposed Gaussian models.

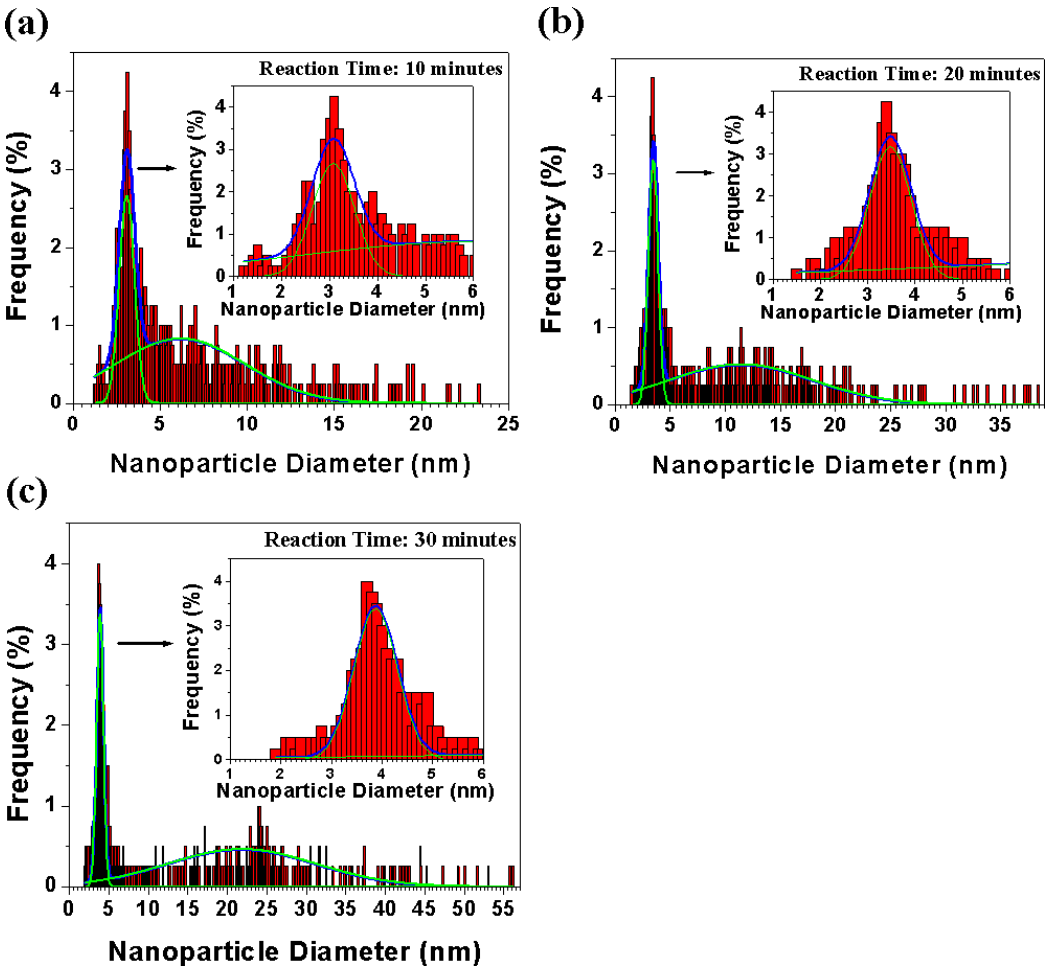


Figure 6.9 Size histograms of the InN colloidal nanoparticles grown for (a) 10, (b) 20 and (c) 30 minutes in solution, respectively. Each histogram is fitted with a model of two Gaussian functions superposed together. Insets in (a)~(c): the corresponding histograms in the small nanoparticle size (< 6 nm) region.

Since a large majority of nanoparticles exhibit sizes smaller than 6 nm, the centre of the Gaussian distribution in the small-size region (< 6 nm) is the most probable size of

the nanoparticles, and the standard deviation of the distribution gives an idea of how narrow or wide the size distribution is. Table 6.1 lists the most probable sizes and the standard deviations (with fitting errors) obtained from the fitting of the size histograms in Figure 6.9 in the small particle size (< 6 nm) region, for the InN colloidal nanoparticles grown for 10, 20 and 30 minutes in solution, respectively. It is seen that the most probable size of the InN colloidal nanoparticles increases with the increase of reaction time.

Table 6.1 Most probable sizes and standard deviations (with fitting errors) from the fitting to the size histograms in Figure 6.9 in the small-size (< 6 nm) regions.

InN Nanoparticles	most probable size (nm)	standard deviation
10 minutes' reaction	3.08 ± 0.03	0.88 ± 0.05
20 minutes' reaction	3.56 ± 0.02	0.87 ± 0.04
30 minutes' reaction	3.87 ± 0.02	0.86 ± 0.04

6.2.2.2 Possible Growth Mechanisms

As stated above, experimental observations show that the crystalline structures of the InN colloidal nanoparticles depend on the particle size, and the most probable particle size and size distribution depend on the reaction time. To understand such dependences and to give an explanation to the experimental observation of two populations of InN colloidal nanoparticles (Figure 6.9), solution-phase growth mechanisms of each subsequent reaction stage are hypothesized:

(i) At the initial stage of reaction, the reactants' concentration is high and a large number of very small nanoparticles (initial "seeds") are nucleated at a short time. At such small sizes, InN nanoparticles with both the stable hexagonal (wurtzite) and the metastable cubic (zincblende) phases[232] can coexist. The total energy of InN in the cubic (zincblende) structure is predicted to be only ~20 meV per ion pair higher than that in the hexagonal (wurtzite) structure,[232] and the theoretical prediction[233] suggests that the kinetic barriers to structural transformations in defect-free nanoparticles can be easily overcome at very small nanoparticle sizes.

(ii) As the reaction proceeds, the rate of particle nucleation decreases as the reactants are consumed, and small-size InN colloidal nanoparticles grow into big ones. It is hypothesized that some factors in the synthesis procedure inhibit the growth of the hexagonal (wurtzite) InN nanoparticles, but not that of the cubic (zincblende) ones. For example, surfactants or capping materials (usually large organic molecules) bind to the nanoparticle surface, acting as capping agents and poisoning some of the active sites of nanoparticles, thus protecting the particles from increasing in size. The InN colloidal nanoparticles of the higher-energy cubic (zincblende) phase may have more active sites than the stable hexagonal (wurtzite) ones, thus the growth of the cubic InN colloidal nanoparticles is faster than that of the hexagonal ones. The coarsening of colloidal nanoparticles could be attributed to either the Ostwald ripening process[234]

or the oriented attachment growth mechanism.[235] Defects are generated if imperfect oriented attachment occurs.

6.2.2.3 Optical Properties

It is known that semiconductor nanoparticles exhibit size-tuneable band gaps and luminescence energies owing to the quantum-size effect.[236] The band gap energy of a semiconductor is defined as the energy difference between the top of the valence band and the bottom of the conduction band. The colour of light emitted by the semiconductor material is determined by the width of the gap. In a bulk semiconductor, the gap width is a fixed parameter. However, in the case of nanoscale semiconductor particles, their band gap energies increase as the motion of the charge carriers is confined in the reduced sizes. This phenomenon is known as the quantum-size effect.[236]

The relationship between band gap and particle size can be approximated using the effective mass model for spherical particles with a Coulomb interaction term,[237] where the band gap $E_g^{particle}$ can be approximated by:

$$E_g^{particle} = E_g^{bulk} + E_{well} + E_{Coulomb} \quad (6.1)$$

As seen from Equation 6.1, the minimum energy required for creating an electron-hole pair in a nanoparticle is made up of several contributions. One contribution is the

bulk band gap energy, E_g^{bulk}. Another important contribution is the confinement energy for the carriers, E_{well}. For spherical nanoparticles,

$$E_{well} = \frac{h^2}{2d^2}\left(\frac{1}{m_e} + \frac{1}{m_h}\right) \tag{6.2}$$

where d is the diameter of the spherical nanoparticle, m_e is the effective mass of the electron, m_h is the effective mass of the holes, and h is the Planck's constant. In the case of InN, the electron effective mass is $0.10m_0$ and the effective masses of heavy and light holes are $1.63m_0$ and $0.27m_0$, respectively,[238] where m_0 is the free electron mass.

The third term in Equation 6.1, the Coulomb energy, $E_{Coulomb}$, is also considered to calculate the energy required to create an electron-hole pair. The Coulomb interaction takes into account the mutual attraction between the electron and the hole, multiplied by a coefficient that describes the screening of the carriers by the crystal. The strength of the screening coefficient depends on the relative permittivity ε of the semiconductor. An estimate of the Coulomb term yields[239]

$$E_{Coulomb} = -\frac{1.8e^2}{2\pi\varepsilon\varepsilon_0 d} \tag{6.3}$$

where ε_0 is the permittivity of free space, e is the charge of the electron, and the reported value of the relative permittivity ε of InN is 15.3 at 300 K.[240]

Then, by inserting Equations 6.2 and 6.3 into 6.1, one obtains

$$E_g^{particle} = E_g^{bulk} + \frac{h^2}{2d^2}\left(\frac{1}{m_e} + \frac{1}{m_h}\right) - \frac{1.8e^2}{2\pi\varepsilon\varepsilon_0 d} \tag{6.4}$$

As seen from Equation 6.4, the basic approximation for the band gap of a spherical nanoparticle comprises two size-dependent terms, the confinement energy, which varies as $\frac{1}{d^2}$, and the Coulomb attraction, which varies as $\frac{1}{d}$. The confinement energy is always a positive term, and thus the energy of the lowest possible state is always raised with respect to the bulk situation. On the other hand, the Coulomb interaction is always attractive for an electron-hole pair system and therefore lowers the energy of its formation. Because of the $\frac{1}{d^2}$ dependence, the quantum confinement effect becomes the predominant term for very small nanoparticle sizes.

Equation 6.4 gives an approximation of the relationship between the optical band gap energy and the nanoparticle size. For the InN colloidal nanoparticles to have the band gaps of the observed 2.31 eV (emission at 536 nm), 1.84 eV (emission at 675 nm) and 1.70 eV (emission at 730 nm) (Figure 6.1), the diameters of the InN nanoparticles can be calculated by solving Equation 6.4. Table 6.2 shows the calculated InN nanoparticle diameters with either the heavy or the light hole mass of InN. It is seen that the calculated particle diameters using the heavy hole mass match well with the experimentally determined most probable sizes of the InN colloidal nanoparticles [in the small-size (< 6 nm) regions in Figure 6.9]. It indicates that the shifts of the PL bands of the InN colloidal nanoparticles with reaction time are due to the quantum-size effect of nanoparticles. The band gap energy decreases as the particle size increases with prolonged reaction time.

Table 6.2 The calculated diameters of the InN nanoparticles using either the heavy or light hole mass, where d_h and d_l denote the particle diameters calculated using the heavy and the light hole masses, respectively.

InN Nanoparticles	Emission band (nm)	Band gap (eV)	d_h (nm)	d_l (nm)	Experimentally obtained most probable size [Figure 6.9, in the small-size (< 6 nm) region] (nm)
10 minutes' reaction	536	2.31	3.04	3.47	3.08 ± 0.03
20 minutes' reaction	675	1.84	3.60	4.11	3.56 ± 0.02
30 minutes' reaction	730	1.70	3.83	4.38	3.87 ± 0.02

As the optical properties of semiconductor nanoparticles are strongly dependent on particle size, a particle size distribution is expected to cause inhomogeneous broadening of optical spectra as a result of distributed band gap energies. Here a theoretical analysis of the PL line shape for different particle size distributions is presented.

First of all, let us start the theoretical analysis by considering the PL line shape of the bulk of a direct band gap semiconductor. Considering the photoluminescence arising from the recombination of carriers at the band-edge, the resulting line shape can be represented by a Gaussian profile:[241]

$$g_{bulk}(E) = \frac{A}{\Gamma\sqrt{2\pi}} \exp\left[-\frac{(E - E_g^{bulk})^2}{2\Gamma^2}\right] \tag{6.5}$$

where the prefactor A represents the area under the curve and hence the integrated intensity, Γ is the parameter representing the intrinsic line width of the PL spectrum arising from the vibronic coupling, and E_g^{bulk} is the bulk band gap energy.

In the case of a semiconductor nanoparticle, the band gap energy is raised with respect to that of the bulk due to the quantum-size effect (Equation 6.4). In view of the shift of the direct interband transition energy, the PL spectrum of a semiconductor nanoparticle will also be shifted by the same amount. Following Equation 6.5, the PL spectrum of a spherical semiconductor nanoparticle with a diameter of d can thus be given by

$$g_{particle}(E,d) = \frac{A}{\Gamma\sqrt{2\pi}} \exp\left[-\frac{(E - E_g^{particle})^2}{2\Gamma^2} \right] \tag{6.6}$$

If the nanoparticle size is not uniform, but has a distribution, $P(d)$, each particle would exhibit a PL peak at a position dictated by its diameter, and the PL spectrum of the nanoparticle system can be taken as the superposition of the contribution from each individual nanoparticle.

In addition, one should note that the luminescence also depends on the exciton oscillator strength, which is strongly size dependent. The oscillator strength is a dimensionless number that describes the relative intensity of an optical transition. By confining the electron and hole in a small cluster, the oscillator strength can increase due to the enhanced spatial overlap between the electron and hole wave functions and the coherent motion of exciton.[242] The variation of the oscillator strength (f_{osc}) with the nanoparticle diameter d is usually assumed to be of a polynomial form such as

$$f_{osc} \propto d^{-\beta} \tag{6.7}$$

by effective-mass-theory-based calculations, where β is a constant, which has been previously suggested to be $\beta = 3$ for semiconductor nanoparticles with a spherical

shape.[243] Therefore, the influence of the size-dependent oscillator strength on the luminescence of semiconductor nanoparticles should be considered when calculating the overall PL line shape, which can be determined by integrating $g_{particle}(E,d)$ over size distribution $P(d)$:

$$\begin{aligned} G(E) &= \int K_1 f_{osc}(d) g_{particle}(E,d) P(d) d(d) \\ &= \int K_2 \frac{1}{d^{\beta}} \frac{A}{\Gamma\sqrt{2\pi}} \exp\left[-\frac{(E - E_g^{particle})^2}{2\Gamma^2} \right] P(d) d(d) \end{aligned} \tag{6.8}$$

where K_1 and K_2 are constants.

To simplify the calculation of Equation 6.8, firstly it is necessary to know a simpler form for the dependence of band gap energy $E_g^{particle}$ on the size *d*. This is obtained by fitting the calculated values of the energy upshift ΔE (shown by the hollow points in Figure 6.10) to an empirical form

$$\Delta E = E_g^{particle} - E_g^{bulk} = \frac{c}{d^x} \tag{6.9}$$

where c and x are constants. A nonlinear least squares fit (using the Microcal™ Origin 6.0 software) to Equation 6.9 gives the values of $c = 15.776$ eV·nm^x and $x = 2.004$. It is seen that $x = 2.004 \approx 2$, indicating that the Coulomb energy $E_{Coulomb}$ in Equation 6.4 is of a much smaller magnitude than the confinement energy E_{well}, and the Coulomb term is negligible.

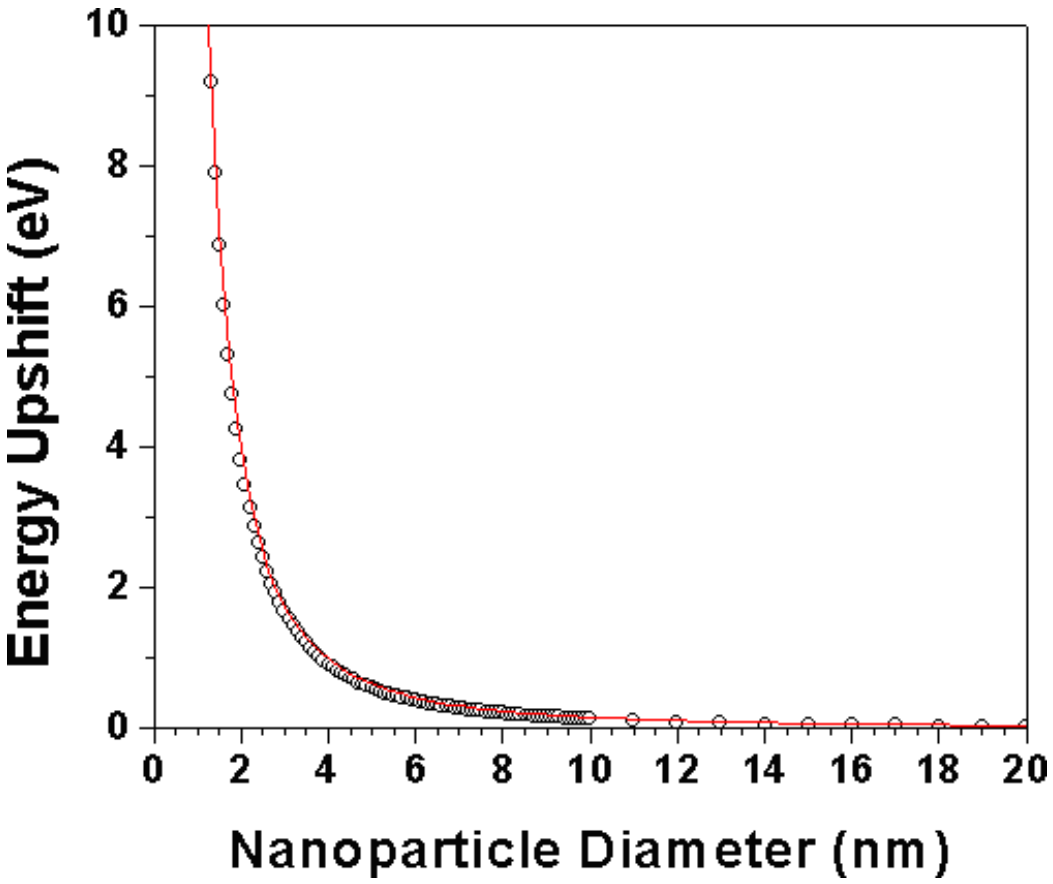


Figure 6.10 Calculated (using Equation 6.4) band gap energy upshift, ΔE, as a function of InN nanoparticle diameter *d* using the value of the heavy hole mass of InN. The solid line is the nonlinear least squares fitting to Equation 6.9.

Secondly, for a semiconductor nanoparticle, the intrinsic line width of the PL spectrum Γ arising from the vibronic coupling tends to zero ($\Gamma \to 0$). This is because the vibronic coupling is proportional to the interaction between electronic and nuclear motions of molecules, and it is large when two allowed transition states are close to each other. However, in small semiconductor nanoparticles where the quantum-size effects occur, the electron and hole wave functions experience boundary conditions that select discrete allowed levels from the conduction and valence band continuum. This lowers the vibronic coupling between allowed transition states, and hence the

line width of the PL spectrum.[244] Thus a Dirac delta function[245] is introduced to further simplify the calculation of Equation 6.8:

$$\frac{1}{\Gamma\sqrt{2\pi}}\exp\left[-\frac{(E-E_g^{bulk}-\frac{c}{d^x})^2}{2\Gamma^2}\right]\approx\delta(E-E_g^{bulk}-\frac{c}{d^x}) \tag{6.10}$$

In this thesis, although the size histogram of the InN colloidal nanoparticles is best fitted by a superposed Gaussian model containing two Gaussian peaks (Figure 6.9), only one Gaussian size distribution is used to compute the general expression for the PL line shape of nanoparticle system, this is based on the assumption that large-size (> 6 nm) InN colloidal nanoparticles do not contribute to PL emission (to be discussed later).

$$P(d)\propto\frac{1}{\sigma\sqrt{\frac{\pi}{2}}}\exp\left[-\frac{2(d-d_m)^2}{\sigma^2}\right] \tag{6.11}$$

where d_m is the most probable diameter of the nanoparticle, and σ is the standard deviation of the particle size distribution.

Inserting Equations 6.9, 6.10 and 6.11 into Equation 6.8, one obtains

$$G(E)=K_3\int\delta_{\sqrt{2}\Gamma}(E-E_g^{bulk}-\frac{c}{d^x})\frac{1}{d^\beta}\frac{1}{\sigma}\exp\left[-\frac{2(d-d_m)^2}{\sigma^2}\right]d(d) \tag{6.12}$$

where K_3 is a constant. The Dirac delta function facilitates a straightforward integration and yields

$$G(E) = K_4 \frac{1}{\sigma}(E - E_g^{bulk})^{\frac{\beta - x - 1}{x}} \exp\left\{ - \frac{2\left[\left(\frac{c}{E - E_g^{bulk}} \right)^{\frac{1}{x}} - d_m \right]^2}{\sigma^2} \right\} \quad (6.13)$$

where K_4 is a constant.

In Figure 6.11, the theoretically-predicted PL line shapes based on Equation 6.13 are depicted (dashed curves), for the InN colloidal nanoparticles grown for 10, 20 and 30 minutes in solution. The most probable diameter and the standard deviation of the distribution used for calculation are obtained from the Gaussian fit to the size histograms in Figure 6.9 in the small-size (< 6 nm) region. Because it is assumed that large-size (> 6 nm) InN colloidal nanoparticles, which are either cubic (zincblende) structured or defective, do not contribute to PL emission. Such assumption is based on the PL measurements on the size-selective InN colloidal nanoparticles carried out by the industrial collaborators [a size-selective chemical method was developed by the industrial collaborators to separate the < 20 nm nanoparticles from those larger than 20 nm. PL measurements were performed on both size-selected InN colloidal nanoparticle specimens. It is found (data not shown) that there are no changes in the PL spectrum of the < 20 nm nanoparticles, as compared with that of the same specimen without size selection; however, photoluminescence is not observed in the specimen that contains only > 20 nm InN nanoparticles].

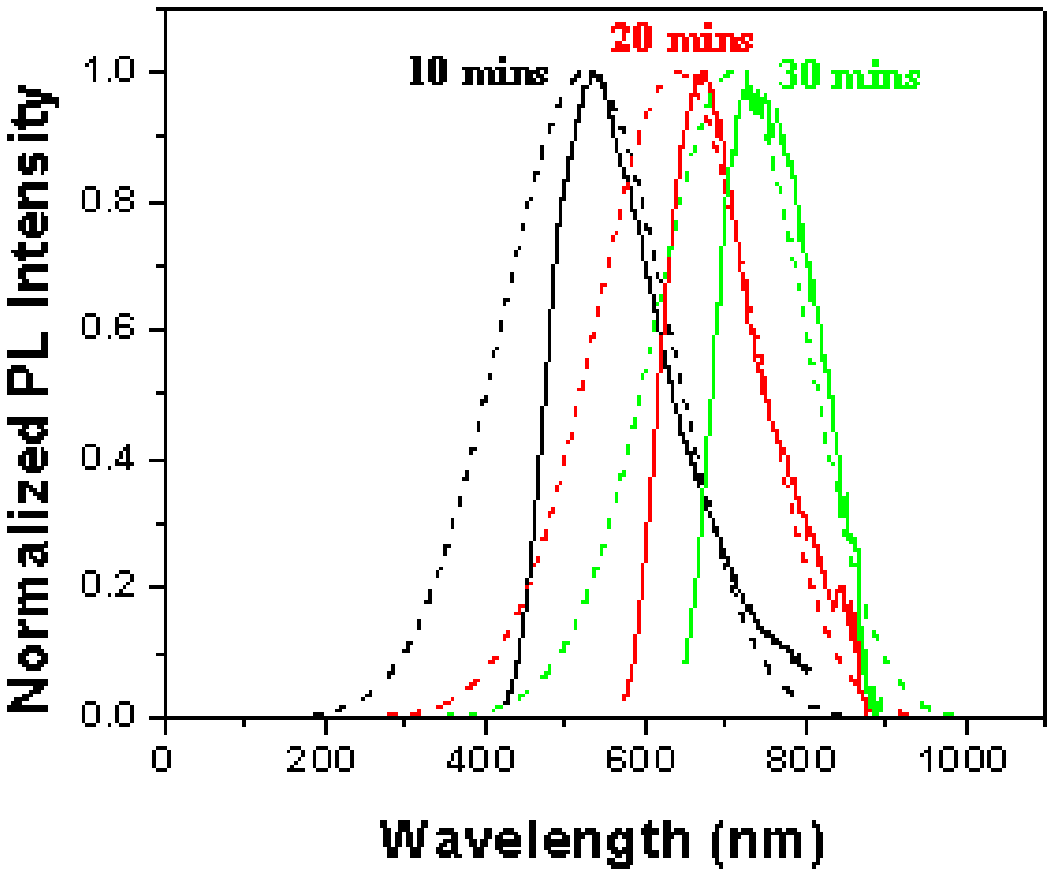


Figure 6.11 Comparison of the theoretically-predicted PL line shapes (dashed lines) with the corresponding experimental PL spectra (solid lines), for the InN colloidal nanoparticles grown for 10, 20 and 30 minutes in solution.

Figure 6.11 also compares the theoretically-predicted PL line shapes with the corresponding experimental PL spectra, for the InN colloidal nanoparticles grown for 10, 20 and 30 minutes in solution. It is seen that for each specimen, the theoretically predicted PL line shape is broader than the experimentally observed PL spectrum, and the experimental PL spectrum deviates from the theoretical prediction in the higher-energy (lower-wavelength, smaller-size) side. Some hypotheses are suggested to understand the discrepancies: firstly, even in the small-size (< 6 nm) region, the cubic (zincblende) InN colloidal nanoparticles may not contribute to the luminescence [note

that both the cubic (zincblende) and the hexagonal (wurtzite) InN colloidal nanoparticles coexist in this region]; secondly, the high surface to volume ratio of small nanoparticles suggests that the surface properties could strongly affect their optical properties. It is likely that localized surface-trap states arising from surface nonstoichiometry or unsaturated bonds could reduce the PL emission efficiency.

6.3 Chapter Summary

The formation of the InN colloidal nanoparticles synthesized from solution-phase reactions was confirmed by studying their compositions, crystalline structures and shape using various EM techniques. The crystalline structures of the InN colloidal nanoparticles are found to be particle size dependent, and the most probable size of the nanoparticles increases and the size distribution broadens with the increase of reaction time. A possible colloidal nanoparticle growth mechanism is proposed to explain such dependences. The band gap energy of the InN colloidal nanoparticles decreases as the particle size increases with prolonged reaction time owing to the quantum-size effect. A theoretical model is developed to predict the PL spectra of the InN colloidal nanoparticles, by considering both the particle size distribution and the size-dependent exciton oscillator strength.

Chapter 7

Overall Conclusions and Future Work

7.1 Introduction

Semiconductor nanostructures have become a focus of research owing to their unique electrical and optical properties in mesoscopic physics and potential applications in nanoscale functional devices such as FETs, LEDs and sensors. With the intention of contributing to the fundamental understanding of nanostructure growth mechanisms and the structure-property relationships at the nanoscale, this thesis focused on the study of the microstructural properties of two important semiconductor nanostructures: 1D axially doped SiNWs and 0D InN colloidal nanoparticles. In the following subchapters, the main scientific findings and conclusions of this thesis are summarized, and some possible future work is also proposed.

7.2 Axially Doped Silicon Nanowire Heterostructures

7.2.1 Conclusions

In this thesis, ~22 μm long axial heterostructured SiNWs consisting *n*-type (boron-doped or B-doped), *p*-type (phosphorus-doped or P-doped) and intrinsic Si (*p*-*n*-*i* SiNWs) were grown on the Si{111} substrate by a VLS approach using gold as the catalyst. The microstructural properties, including the crystalline structures, wire growth direction and surface properties, were studied using various EM techniques and Raman spectroscopy.

It is found that the crystalline structure of SiNWs can be quite different from that of bulk Si. A large majority (~98%) of the axial heterostructured SiNWs grown on an oxide-removed Si{111} substrate have the diamond cubic crystalline structure, which is the stable form of bulk Si under ambient conditions; however, a very small fraction (~2%) of the SiNWs exhibit the hexagonal (wurtzite) structures, which are metastable phases for bulk Si. Detailed EDPs and HRTEM analyses (with careful calibration of magnification) indicate the formation of both the type A and type B (different in lattice parameters) hexagonal (wurtzite) SiNWs. It is suggested that high pressures on Au catalyst and SiNW during the growth (*e.g.*, Au cluster appears at an unfavourable position on the substrate) can be a possible cause for the formation of hexagonal (wurtzite) SiNWs observed in this thesis.

Another fundamental microstructural property of axial heterostructured SiNWs, the wire growth direction, was determined using both the "shadow imaging" and the HRTEM techniques. It is found that about 75% of the ~22 μm long axial heterostructured SiNWs are kink-free and <111>-oriented, while the rest have growth-related kinks. For the most commonly observed ~109° kinked SiNWs, the wire growth directions before and after the kink are both <111>. The ~109° kink exhibits an elbow-shaped structure, where the nanowire sidewalls are blunted by several {111} and {100} short facets.

The surface properties of the axial heterostructured *p*-*n*-*i* SiNWs were also studied. The nanowire sidewalls exhibit periodic nanofaceting, which is strongly doping-dependent, *i.e.*, sidewall nanofacets occur in the boron-doped (*p*-type) region, while both the phosphorus-doped (*n*-type) and the intrinsic SiNW regions exhibit smooth surface morphology. This is because the introduction of B_2H_6 dopant gas alters the nanowire growth mechanism and behaviour by enhancing the sidewall growth and creates a faceted sidewall surface. HRTEM shows that the nanowires are axially oriented along <111>, and the crystallographic planes on which the nanofaceting of the sidewalls occurs are Si{111} and Si{100}. The nanofaceting occurs during the enhanced sidewall growth that arises with the B-doping, rather than from instabilities in the liquid droplet at the primary growth front as suggested for the previously observed nanofaceting on SiNW sidewalls.

A thermodynamic model of periodic surface faceting was developed for the high curvature surfaces of a nanowire structure. The distance between nanofacets (facet period) is predicted to be wire diameter dependent, where the facet period decreases as the wire diameter increases. This model consistently explains the experimentally observed dependence of facet size on wire diameter in the boron-impurity induced nanofaceting on SiNW sidewalls in the VLS-grown SiNWs, and quantitatively fits the experimental data with independently established values for the apex and edge energy parameters.

7.2.2 Future Work

Based on the studies carried out in this thesis, some possible future developments are proposed as follows:

(i) Ultra-thin SiNWs:

Due to the synthesis method, no VLS-grown SiNWs in this thesis have wire diameters less than 30 nm. However, such ultra-thin SiNWs will be of great interest, because (i) the electrical and optical properties of SiNWs are strongly size dependent (quantum-size effect); and (ii) small-size SiNWs should lead to a high density of SiNW-based devices on a chip. For VLS-grown SiNWs with very small diameters (< ~30 nm), the wire growth directions, cross sections and sidewall orientations are different from those of SiNWs with larger sizes (> ~30

nm, as in this thesis).[146,147] In addition, the effects of impurity doping on these microstructural properties of ultra-thin SiNWs have not been well studied.

In this thesis, the introduction of the B_2H_6 dopant gas induces nanofaceting on the nanowire sidewall surfaces during the VLS growth of <111>-oriented SiNWs with diameters larger than 30 nm. However, it is not known if such impurity-induced nanofaceting would occur on the sidewalls of very thin (< ~30 nm) SiNWs. In addition, the thermodynamic model of periodic surface nanofaceting developed for a nanowire structure (discussed in Chapter 5) does not apply to SiNWs with very small diameters, because of the different growth behaviour and crystallographic orientations exhibited by the small-diameter SiNWs. Different nanowire growth mechanisms and faceting models (should they exist) will come into play. Therefore, to further the understanding of nanowire growth mechanism and to provide important information on the control of nanowire surfaces, it is essential to study the effects of doping on the microstructural properties of ultra-thin SiNWs.

(ii) Oxidation of SiNWs:

Another interesting yet challenging future work is associated with the oxidation of SiNWs. As the ultra-large-scale integration dimension approaches the nanoscale, the interest in the fabrication of SiNWs typically surrounded by oxide layers has increased enormously due to the potential device applications and novel physical

properties.[59] Oxidation of SiNWs, which includes the native oxide (1~3 nm thick) that typically surrounds the as-grown SiNWs and the thermally-grown silicon dioxide (SiO_2), can provide a dielectric shell for SiNW-based nanoscale FETs, as well as a passive surface/sacrificial spacer during the assembly of nanowire arrays.

As observed in this thesis, when the B_2H_6 dopant gas is introduced during the VLS growth of SiNWs, Si{111} and Si{100} nanofacets occurred on the sidewalls of the <111>-oriented SiNWs, while in the SiNW regions without the sidewall nanofaceting, the sidewalls are Si{112} planes. This provides an opportunity to study the oxide growth rate of Si surfaces with different orientations at the nanoscale. Although for single crystal bulk Si under a given oxidation temperature and oxidant pressure, Si{111} planar surfaces generally oxidize more readily than Si{100},[246] it may not be true at a nanoscale facet on the SiNW sidewall. In addition, Si{111} and Si{100} nanofacets occurred in the B-doped SiNW region; here the impurity doping should play an important role in the growth of oxide on these surfaces.

Over the past few decades, massive efforts have been made to understand the oxidation process of bulk Si; however, there are still many unknowns associated with the oxidation of SiNWs at the nanoscale. In addition, the current level of knowledge on the oxidation of SiNWs is still not enough for the accurate control of the gate dielectric formation. Therefore, it is important to study the oxidizing

behaviour of SiNWs, as well as the chemistry and physics occurring at the Si/oxide interface during the oxidation of SiNWs.

(iii) Physical properties of SiNW heterostructures:

This thesis is focused on the microstructural studies of the axial heterostructured SiNWs with varying doping; however, their physical properties, including electrical, photonic, mechanical and thermal properties, have not been fully characterized. In addition, the relationship between their microstructures and physical properties has not been studied. Such axial nanowire heterostructures with varying doping are potential candidate materials for constructing nanoscale electronic circuits and LEDs.[60] Therefore, it is necessary to characterize the physical properties of such nanowire heterostructures, and to understand their structure-property relationship. This can be a possible future research direction.

7.3 Indium Nitride Colloidal Nanoparticles

7.3.1 Conclusions

In this thesis, the formation of the InN colloidal nanoparticles grown from solution-phase reactions is confirmed by examining their compositions, crystalline structures and shape using various EM techniques.

STEM images show that the nanoparticles exhibit a near-spherical shape. EDX characterization indicates that the harvested colloidal nanoparticles contain In, N, Zn and O, while the carbon film on which the nanoparticles were deposited also contains O and Zn. The presence of Zn and O can be due to the Zn-containing capping layers used for the synthesis of InN colloidal nanoparticles. The presence of O may also result from the surface oxidation of the InN nanoparticles, and the oxygen may exist as an amorphous indium oxynitride in the InN matrix.

The crystalline structure of the InN colloidal nanoparticles is found to be particle size dependent. Both the hexagonal (wurtzite, the stable form for bulk InN) and cubic (zincblende, the metastable form for bulk InN) InN colloidal nanoparticles are observed with the sizes of 4~5 nm. Cubic (zincblende) structure is observed in the InN colloidal nanoparticles larger than ~7 nm while no nanoparticles larger than ~7 nm exhibit a pure hexagonal (wurtzite) phase. Significant amount of defects, including stacking faults, twins, and crystalline structure changes between the cubic (zincblende) and the hexagonal (wurtzite) phases are observed in large-size (> 7 nm) InN colloidal nanoparticles.

The size of the InN colloidal nanoparticles was controlled by varying the reaction time of solution-phase reactions. The particle size distribution plots exhibit two Gaussian-like peaks: one shows a sharp peak in the small particle size region (< 6 nm), and another shows a broader peak in the large-size region. It indicates that a

large majority of the InN colloidal nanoparticles have sizes smaller than 6 nm. The most probable size of the InN colloidal nanoparticles increases and the size distribution broadens with the increase of reaction time. A possible colloidal nanoparticle growth mechanism is proposed, and it is assumed that the small-size (< 6 nm, the sharp peak in the size distribution plot) nanoparticles are mainly hexagonal (wurtzite) and cubic (zincblende) InN, while those with larger sizes (the broader peak) consist of both the cubic (zincblende) InN nanoparticles and defective ones.

The observed dependence of the band gap blueshift of the InN colloidal nanoparticles on the reaction time (hence the particle size) is explained by the quantum-size effect. The effects of particle size distribution on the PL emission spectra are studied by carrying out a theoretical PL line shape analysis. The theoretically-predicted PL spectra exhibit a broader line shape than the experimental ones, because some nanoparticles (the zincblende structured or defective ones) may not contribute to the luminescence.

7.3.2 Future Work

Due to the difficulties in chemical synthesis (such as the chemical instability and limitations in choosing appropriate ligands) and the low dissociation temperature of InN, InN colloidal nanoparticles are less well studied semiconductor nanostructures compared with other group III-nitride nanostructures. Further research is required in

these research areas.

(i) Compositions - oxygen in the InN colloidal nanoparticles:

For bulk InN, the stoichiometry between indium and nitrogen in InN has been a longstanding controversy in the literature.[202,203] In addition, the presence of oxygen in InN is believed to play an important role in the band gap energy of InN. This thesis shows that the harvested InN colloidal nanoparticles contain oxygen, which may come from either the organic capping layers or the surface oxidation of InN colloidal nanoparticles. However, the exact physical/chemical origins and the distribution of the oxygen in the InN colloidal nanoparticles are not known. Here quantitative compositional analysis of the InN colloidal nanoparticles and modelling on the oxygen distribution can provide important information for settling these questions.

(ii) InN-based core/shell colloidal nanoparticles:

In the materials studied in this thesis, the surface of the InN colloidal nanoparticles is coated with a layer of ligands/capping groups. However, a layer of ligands on the nanoparticle surface cannot fully fulfil the stability requirements for reliable device applications. For example, ligands may dissociate and fail to maintain a colloidal suspension, and the nanoparticles thus have a relatively short lifetime. In addition, if the surface passivation of colloidal nanoparticles by organic ligands is imperfect, optimum optical properties, such as a high

fluorescence quantum yield and the stability against photo-degradation, are difficult to achieve. Therefore, it is desirable to provide a method to maintain a colloidal suspension of nanocrystals for a very long time and to prevent the oxidation of nanocrystals.

A possible solution to these problems is to grow a layer of another appropriate material onto the colloidal nanoparticles to form a core/shell structure. Growing a shell of another semiconductor on colloidal nanoparticles can increase both the fluorescence quantum yield and the stability. In the majority of cases, the core material having a certain band gap is capped by a material with a larger band gap, the conduction band energy of the capping material being higher than that of the core material and the valence band energy of the capping material being lower than that of the core material. The main consequence of this capping is that the exciton photo-generated in the core is prevented from spreading over the entire particle, and by this it is forced to recombine while spatially confined to the core. In most cases this is accompanied by enhanced luminescence.[247]

To form a core/shell structure based on the existing InN colloidal nanoparticles, it is important to select an appropriate semiconductor, which should have a larger band gap than InN, and should be able to be grown on the surface of the InN colloidal nanoparticles through solution-phase reactions. The microstructural and optical properties of such InN-based core/shell colloidal nanoparticles are also of

great interest.

(iii) Shape control through colloidal nanocrystal growth:

The shape of the nanocrystals formed during the colloidal growth strongly affects their physical properties. In this thesis, the harvested InN colloidal nanoparticles have a 0D near-spherical shape. However, other nanostructures, such as 1D rods, 2D discs and 3D complex structures, can be obtained at a high growth rate following a kinetic shape-controlling nanocrystal growth mechanism.[98] It will lead the research of InN to a broader scope, where InN nanostructures with far more complex shapes are created through solution-phase synthesis, with greater control over size and shape. Improved experimental studies of nanocrystal growth kinetics and real-time monitoring of average size and shape, could deliver much-needed further information.

7.4 Chapter Summary

This is the final chapter of the thesis. The overall conclusions of the thesis are stated. Possible future work that should be carried out to answer questions raised by this thesis is suggested.

References

[1] G. E. Moore, Electronics, 38, 114 (1965).

[2] P. Yang, Y. Wu, and R. Fan, Int. J. Nanosci., 1, 1 (2002).

[3] H. Röder, E. Hahn, H. Brune, J.-P. Bucher, and K. Kern, Nature, 366, 141 (1993).

[4] V. V. Pokropivny and V. V. Skorokhod, Mater. Sci. Eng. C, 27, 990 (2007).

[5] C. M. Lieber, Solid Stat Commun., 107, 607 (1998).

[6] A. P. Alivisatos, Endeavour, 21, 56 (1997).

[7] C. M. Lieber, Sci. Am., 285, 58 (2001).

[8] C. Thelander, P. Agarwal, S. Brongersma, J. Eymery, L. F. Feiner, A. Forchel, M. Scheffler, W. Riess, B. J. Ohlsson, U. Gösele, and L. Samuelson, Materials Today, 9, 28 (2006).

[9] W. C. O'Mara, R. B. Herring, L. P. Hunt, Handbook of Semiconductor Silicon Technology, Noyes Publications (1990).

[10] J. Thomas, Silicon, New York: Marshall Cavendish (2001).

[11] V. Schmidt, J. V. Wittemann, S. Senz, and U. Gösele, Adv. Mater., 21, 2681 (2009).

[12] Y. Cui, Z. Zhong, D. Wang, W. U. Wang and C. M. Lieber, Nano. Lett., 3, 149 (2003).

[13] Y. Huang, X. Duan, Y. Cui, L. J. Lauhon, K. Kim, and C. M. Lieber, Science, 294, 1313 (2001).

[14] Z. Zhong, D. Wang, Y. Cui, M. W. Bockrath, and C. M. Lieber, Science, 302, 1377 (2003).

[15] Z. Li, Y. Chen, X. Li, T. I., Kamins, K. Nauka, and R. S. Williams, Nano. Lett., 4, 245 (2004).

[16] R. He, and P. Yang, Nat. Nanotechnol., 1, 42 (2006).

[17] S. M. Sze, Physics of Semiconductor Devices, 2nd ed., Wiley, New York (1981).

[18] L. J. Lauhon, M. S. Gudiksen, D. Wang, and C. M. Lieber, Nature, 420, 57 (2002).

[19] R. Bogue, Sensor Review, 25, 180 (2005).

[20] H. Z. Zhang, D. P. Yu, Y. Ding, Z. G. Bai, Q. L. Hang, and S. Q. Feng, Appl. Phys. Lett., 73, 3396 (1998).

[21] S. Fan, J. Cao, H. Dang, Q. Gu, and J. Zhao, Mater. Sci. Eng. C, 15, 295 (2001).

[22] Y. F. Zhang, Y. H. Tang, N. Wang, D. P. Yu, C. S. Lee, I. Bello, and S. T. Lee, Appl. Phys. Lett., 72, 1835 (1998).

[23] V. Sivakov, G. Andra, U. Gösele, and S. Christiansen, Phys. Stat. Sol. A, 203, 3692 (2006).

[24] G. Gundiah, F. L. Deepak, A. Govindaraj, and C. N. R. Rao, Chem. Phys. Lett., 381, 579 (2003).

[25] R. Q. Zhang, Y. Lifshitz, and S. T. Lee, Adv. Mater. 15, 635 (2003).

[26] W. S. Shi, H. Y. Peng, Y. F. Zheng, N. Wang, N. G. Shang, Z. W. Pan, C. S. Lee, and S. T. Lee, Adv. Mater., 12, 1343 (2000).

[27] C. P. Li, X. H. Sun, N. B. Wong, C. S. Lee, S. T. Lee, and B. K. Teo, Chem. Phys. Lett., 365, 22 (2002).

[28] T. Ono, H. Saitoh, and M. Esahi, Appl. Phys. Lett., 70, 1852 (1997).

[29] N. R. B. Coleman, M. A. Morris, T. R. Spalding, and J. D. Holmes, J. Am. Chem. Soc., 123, 187 (2001).

[30] Y. Wu, and P. Yang, Chem. Mater., 12, 605 (2000).

[31] C. C. Chen, C. C. Yeh, C. H. Chen, M. Y. Yu, H. L. Liu, J. J. Wu, K. H. Chen, L. C. Chen, J. Y. Peng and Y. F. Chen, J. Am. Chem. Soc., 123, 2791 (2001).

[32] D. Wang, F. Qian, C. Yang, Z. Zhong, and C. M. Lieber, Nano. Lett., 4, 871 (2004).

[33] Y. Wang, L. Zhang, C. Liang, G. Wang, and X. Peng, Chem. Phys. Lett., 357, 314 (2002).

[34] T. I. Kamins, S. Sharma, M. Saif Islam, and R. Stanley Williams, Proceedings of 2005 5th IEEE Conference on Nanotechnology, 1, 47 (2005).

[35] P. Van Zant, Microchip Fabrication: A Practical Guide to Semiconductor Processing, McGraw-Hill Professional, 377~378 (2004).

[36] Y. Xia, P. Yang, Y. Sun, Y. Wu, B. Mayers, B. Gates, Y. Yin, F. Kim, and H. Yan, Adv. Mater., 15, 353 (2003).

[37] Y. Cui, L. J. Lauhon, M. S. Gudiksen, J. Wang, and C. M. Lieber, Appl. Phys. Lett., 78, 2214 (2001).

[38] J. R. Morante, J. E. Carceller, A. Herms, P. Cartujo, and J. Barbolla, Appl. Phys.

Lett., 41, 656 (1982).

[39] Y. Wang, V. Schmidt, S. Senz, and U. Gösele, Nat. Nanotechno., 1, 186 (2006).

[40] T. I. Kamins, R. Stanley Williams, D. P. Basile, T. Hesjedal, and J. S. Harris, J. Appl. Phys., 89, 1008 (2001).

[41] A. Rai, K. Park, L. Zhou, and M. R. Zachariah, Combust. Theo. Model., 10, 843 (2006).

[42] R. S. Wagner, Whisker Technology (ed. A. P. Levitt), Wiley, ch. 2, 15~119 (1970).

[43] Y. Wu, and P. Yang, J. Am. Chem. Soc., 123, 3165 (2001).

[44] R. S. Wagner, and W. C. Ellis, Appl. Phys. Lett., 4, 89 (1964).

[45] E. I. Givargizov, J. Cryst. Growth, 31, 20 (1975).

[46] T. Y. Tan, N. Li, and U. Gösele, Appl. Phys. A, 78, 519 (2004).

[47] L. Schubert, P. Werner, N. D. Zakharov, G. Gerth, F. M. Kolb, L. Long, U. Gösele, and T. Y. Tan, Appl. Phys. Lett., 84, 4968 (2004).

[48] A. Colli, A. Fasoli, P. Beecher, P. Servati, S. Pisana, Y. Fu, A. J. Flewitt, W. I. Milne, J. Robertson, C. Ducati, S. De Franceschi, S. Hofmann, and A. C. Ferrari, J. Appl. Phys., 102, 034302 (2007).

[49] H. Wang, and G. S. Fischman, J. Appl. Phys., 76, 1557 (1994).

[50] T. I. Kamins, R. Stanley Williams, Y. Chen, Y.-L. Chang, and Y. A. Chang, Appl. Phys. Lett., 76, 562 (2000).

[51] P. Werner, N. D. Zakharov, G. Gerth, L. Schubert, and U. Gösele, Int. J. Mater. Res., 97, 1008 (2006).

[52] S. Hofmann, R. Sharma, C. T. Wirth, F. Cervantes-Sodi, C. Ducati, T. Kasama, P.

E. Dunin-Borkowski, J. Drucker, P. Pennett, and J. Robertson, Nature Mater., 7, 372 (2008).

[53] J. M. Blakely, and K. A. Jackson, J. Chm. Phys., 37, 428 (1962).

[54] V. Ruth, and J. P. Hirth, J. Chem. Phys., 41, 3139 (1964).

[55] N. Wang, Y. Cai, and R. Q. Zhang, Mater. Sci. Engin. R, 60, 1 (2008).

[56] V. Schmidt, S. Senz, and U. Gösele, Appl. Phys. A, 80, 445 (2005).

[57] R. Tadmor, Langmuir, 20, 7659 (2004).

[58] N. Li, T. Y. Tan, and U. Gösele, Appl. Phys. A, 86, 433 (2007).

[59] C. M. Lieber, and Z. L. Wang, MRS Bull., 32, 99 (2007).

[60] W. Lu, and C. M. Lieber, J. Phys. D: Appl. Phys., 39, R387 (2006).

[61] Y. Wu, R. Fan and P. Yang, Nano Lett., 2, 83 (2002).

[62] L. J. Lauhan, M. S. Gudiksen, and C. M. Lieber, Phil. Trans. R. Soc. Lond. A, 362, 1247 (2004).

[63] J. M. Redwing, K.-K. Lew, T. Bogart, L. Pan, E. C. Dickey, A. H. Carim, Y. Wang, M. Cabassi, and T. S. Mayer, Proc. SPIE-Int. Soc. Opt. Eng., 5361, 52 (2004).

[64] T. E. Clark, P. Nimmatoori, K.-K. Lew, L. Pan, J. M. Redwing, and E. C. Dickey, Nano Lett., 8, 1246 (2008).

[65] S. Hofmann, G. Csányi, A. C. Ferrari, M. C. Payne, and J. Robertson, Phys. Rev. Lett., 95, 036101 (2005).

[66] Y. Cui, X. Duan, J. Hu and C. M. Lieber, J. Phys. Chem. B, 104, 5213 (2000).

[67] Y. Cui, and C. M. Lieber, Science, 291, 851 (2001).

[68] G. W. Zhou, H. Li, H. P. Sun, D. P. Yu, Y. Q. Wang, X. J. Huang, L. Q. Chen, and Z.

Zhang, Appl. Phys. Lett., 75, 2447 (1999).

[69] G. Zheng, W. Lu, S. Jin, and C. M. Lieber, Adv. Mater., 16, 1890 (2004).

[70] S.-J. Whang, S. Lee, D.-Z. Chi, W.-F. Yang, B.-J. Cho, Y.-F. Liew, and D.-L. Kwong, Nanotechnol., 18, 275302 (2007).

[71] L. Pan, K.-K. Lew, J. M. Redwing, and E. C. Dickey, J. Cryst. Growth, 277, 428 (2005).

[72] K.-K. Lew, L. Pan, T. E. Bogart, S. M. Dilts, E. C. Dickey, J. M. Redwing, Y. Wang, M. Cabassi, T. S. Mayer, and S. W. Novak, Appl. Phys. Lett., 85, 3101 (2004).

[73] A. Yamamoto, M. Tsujino, M. Ohkubo, and A. Hashimoto, Sol. Energy Mater. Sol. Cells, 35, 53 (1994).

[74] S. N. Mohammad, and H. Morkoç, Prog. Quant. Electr., 20, 361 (1996).

[75] F. A. Ponce, and D. P. Bour, Nature, 386, 351 (1997).

[76] S. Nakamura, Science, 281, 956 (1998).

[77] T. Matsuoka, Adv. Mater., 8, 469 (1996).

[78] A. P. Alivisatos, Science, 271, 933 (1996).

[79] C. B. Murray, C. R. Kagan, and M. G. Bawendi, Annu. Rev. Mater. Sci., 30, 545 (2000).

[80] Günter Schmid (Edited), Nanoparticles – From Theory to Application, WILEY-VCH Verlag GmbH & Co. KGaA, Weinheim (2004).

[81] J. B. MacChesney, P. M. Bridenbaugh, and P. B. O'Connor, Mater. Res. Bull., 5, 783 (1970).

[82] T. Matsuoka, Superlattices Microstruct., 37, 19 (2005).

[83] J. W. Trainor, and K. Rose, J. Electron. Mater., 3, 821 (1974).

[84] Q. Guo, O. Kato, and A. Yoshida, J. Appl. Phys., 73, 7969 (1993).

[85] D. A. Neumayer, and J. G. Ekerdt, Chem. Mater., 8, 9 (1996).

[86] A. G. Bhuiyan, K. Sugita, K. Kasashima, A. Hashimoto, A. Yamamoto, and V. Y. Davydov, Appl. Phys. Lett., 83, 4788 (2003).

[87] C.-H. Shen, H.-W. Lin, H.-M. Lee, C.-L. Wu, J.-T. Hsu, and S. Gwo, Thin Solid Films, 494, 79 (2006).

[88] C. Nörenberg, R. A. Oliver, M. G. Martin, L. Allers, M. R. Castell, and G. A. D. Briggs, Phys. Stat. Sol. A, 194, 536 (2002).

[89] Y. G. Cao, M. H. Xie, Y. Liu, Y. F. Ng, H. S. Wu, and S. Y. Tong, Appl. Phys. Lett., 83, 5157 (2003).

[90] A. Yoshikawa, N. Hashimoto, N. Kikukawa, S. B. Che, and Y. Ishitani, Appl. Phys. Lett., 86, 153115 (2005).

[91] S. Ruffenach, B. Maleyre, O. Briot, and B. Gil, Phys. Stat. Sol. C, 2, 826 (2005).

[92] W. C. Ke, C. P. Fu, C. Y. Chen, L. Lee, C. S. Ku, W. C. Chou, W.-H. Chang, M. C. Lee, W. K. Chen, W. J. Lin, and Y. C. Cheng, Appl. Phys. Lett., 88, 191913 (2006).

[93] O. Briot, B. Baleyre, and S. Ruffenach, Appl. Phys. Lett., 83, 2919 (2003).

[94] C. Meissner, S. Ploch, M. Leyer, M. Pristovsek, and M. Kneissl, J. Cryst. Growth, 310, 4959 (2008).

[95] J. G. Lozano, D. González, A. M. Sánchez, D. Araújo, S. Ruffenach, O. Briot, and R. García, Phys. Stat. Sol. C, 3, 1687 (2006).

[96] Q. Guo, X. Mei, H. Ruda, T. Tanaka, M. Nishio, and H. Ogawa, Jpn. J. Appl. Phys.,

42, L508 (2003).

[97] C. R. Martin, Science, 266, 1961 (1994).

[98] Y. Yin, and A. P. Alivisatos, Nature, 437, 664 (2005).

[99] Y.-J. Bai, Z.-G. Liu, X.-G. Xu, D.-L. Cui, X.-P. Hao, X. Feng and Q.-L. Wang, J. Cryst. Growth, 241, 189 (2002).

[100] K. Sardar, F. L. Deepak, A. Govindaraj, M. M. Seikh, and C. N. R. Rao, Small, 1, 91 (2005).

[101] S. D. Dingman, N. P. Rath, P. D. Markowitz, P. C. Gibbons, and W. E. Buhro, Angew. Chem. Int. Ed., 29, 1470 (2000).

[102] M. R. Greenberg, G. A. Smolyakov, Y.-B. Jiang, T. J. Boyle, and M. Osiński, Proc. of SPIE, 6096, 35 (2006).

[103] J. Xiao, Y. Xie, R. Tang, and W. Luo, Inorg. Chem., 42, 107 (2003).

[104] P. S. Schofield, W. Zhou, P. Wood, I. D. W. Samuel, and D. J. Cole-Hamilton, J. Mater. Chem.,14, 3124 (2004).

[105] M. Knoll, and E. Ruska, Z. Physik, 78, 318 (1932).

[106] P. J. Goodhew, F. J. Humphreys, and R. Beanland, Electron Microscopy and Analysis, Taylor & Francis, 66~76 (2001).

[107] D. B. Williams, and C. B. Carter, Transmission Electron Microscopy: A Textbook for Materials Science, New York: Plenum Press (1996).

[108] W. H. Bragg, and W. L. Bragg, WL, Proc. Roy. Soc. Lond. A88, 428 (1913).

[109] P. P. Ewald, Physik. Z., 14, 465 (1913). An English translation is given in D. W. J. Cruickshank, H. J. Juretschke, and N. Kato, P. P. Ewald and his dynamical theory of

X-ray diffraction, Oxford University Press, 114~123 (1992).

[110] O. Scherzer, Z. Phys., 101, 593 (1936).

[111] D. Shi, Functional Thin Films and Functional Materials: New Concepts and Technologies, Springer (2003)

[112] O. Scherzer, J. Appl. Phys., 20, 20 (1949).

[113] http://www.maxsidorov.com/ctfexplorer.

[114] J. M. Cowley, and A. F. Moodie, Acta Cryst., 10, 609 (1957).

[115] D. E. Jesson, and S. T. Pennycook, Proc. R. Soc. A, 449, 273 (1995).

[116] J. M. Rodenburg, and E. B. Macack, Microsc. Anal., 90, 5 (2002).

[117] L. M. Murr, Electron and Ion Microscopy and Microanalysis: Principles and Applications, CRC Press, 197~199 (1991).

[118] R. Castaing, Thesis, University of Paris, ONERA Publication (1951).

[119] G. Cliff, and G. W. Lorimer, J. Microsc. 103, 203 (1975).

[120] J. Goldstein, D. E. Newbury, P. Echlin, D. C. Joy, A. D. Romig Jr., C. E. Lyman, C. Fiori, and E. Lifshin, Scanning Electron Microscopy and X-Ray Microanalysis: A Text for Biologists, Materials Scientists, and Geologists, 2nd edition, New York: Plenum Press (1992).

[121] F. A. Miller, and G. B. Kauffman, J. Chem. Educ., 66, 795 (1989).

[122] R. Loudon, Proc. R. Soc. London A, 275, 218 (1963).

[123] Y. Huang, X. Duan, Q. Wei, and C. M. Lieber, Science, 291, 630 (2001).

[124] D. Whang, S. Jin, Y. Wu, and C. M. Lieber, Nano Lett., 3, 1255 (2003).

[125] A. Kailer, Y. G. Gogotsi, and K. G. Nickel, J. Appl. Phys., 81, 3057 (1997).

[126] R. H. Wentorf, Jr., and J. S. Kasper, Science, 139, 338 (1963).

[127] J. S. Kasper, and R. H. Wentorf, Jr., Science, 197, 599 (1977).

[128] J. Bandet, B. Despax, and M. Caumont, J. Phys. D: Appl. Phys., 35, 234 (2002).

[129] C. Yeh, Z. W. Lu, S. Froyen, and A. Zunger, Phys. Rev. B, 46, 10086 (1992).

[130] H. M. Jennings, and M. H. Richman, Science, 193, 1242 (1976).

[131] A. Fontcuberta i Morral, J. Arbiol, J. D. Prades, A. Cirera, and J. R. Morante, Adv. Mater., 19, 1347 (2007).

[132] J. Arbiol, B. Kalache, P. Roca I Cabarrocas, J. R. Morante, and A. Fontcuberta i Morral, Nanotechnology, 18, 305606 (2007).

[133] C. M. Kachhava, Solid State Physics, Solid State Devices and Electronics, New Age International Publishers (2003).

[134] H. Richter, Z. P. Wang, and L. Ley, Solid State Commun., 39, 625 (1981).

[135] R. Gupta, Q. Xiong, C. K. Adu, U. J. Kim, and P. C. Eklund, Nano Lett., 3, 627 (2003).

[136] G. Weill, J. L. Mansot, G. Sagon, C. Carlone, and J. M. Besson, Semicond. Sci. Technol., 4, 280 (1989).

[137] U. Dahmen, C. J. Hetherington, P. Pirouz, and K. H. Westmacott, Scr. Metall., 23, 269 (1989).

[138] X. Liu, and D. Wang, Nano Res., 2, 575 (2009).

[139] D. C. Bell, Y. Wu, C. J. Barrelet, S. Gradečak, J. Xiang, B. P. Timko, and C. M. Lieber, Microsc. Res. Tech., 64, 373 (2004).

[140] H. Yorikawa, H. Uchida, and S. Muramatsu, J. Appl. Phys., 79, 3619 (1996).

[141] A. M. Morales, and C. M. Lieber, Science, 279, 208 (1998).

[142] E. I. Givargizov, and N. N. Sheftal, J. Cryst. Growth, 9, 326 (1971).

[143] N. Ozaki, Y. Ohno, and S. Takeda, Appl. Phys. Lett., 73, 3700 (1998).

[144] K. K. Lew, C. Reuther, A. H. Carim, J. M. Redwing, and B. R. Martin, J. Vac. Sci. Technol. B, 20, 389 (2002).

[145] S. Sharma, and M. K. Sunkara, Nanotechnology, 15, 130 (2004).

[146] R. Q. Zhang, Y. Lifshiz, D. D. D. Ma, Y. L. Zhao, Th. Frauenheim, S. T. Lee, and S. Y. Tong, J. Chem. Phys., 123, 144703 (2005).

[147] Y. Wu, Y. Cui, L. Huynh, C. J. Barrelet, D. C. Bell, and C. M. Lieber, Nano Lett., 4, 433 (2004).

[148] V. Schmidt, S. Senz, and U. Gösele, Nano Lett., 5, 931 (2005).

[149] G. S. Doerk, N. Ferralis, C. Carraro, and R. Maboudian, J. Mater. Chem., 18, 5309 (2008).

[150] H. Schmid, M. T. Björk, J. Knoch, H. Riel, W. Wiess, P. Rice, and t. Topuria, J. Appl. Phys., 103, 024304 (2008).

[151] J. Westwater, D. P. Gosain, S. Tomiya, S. Usui, and H. Ruda, J. Vac. Sci. Technol. B, 15, 554 (1997).

[152] R. S. Wagner, and C. J. Doherty, J. Electrochem. Soc., 115, 93 (1968).

[153] B. Tian, P. Xie, T. J. Kempa, D. C. Bell, and C. M. Lieber, Nat. Nanotechnol., 4, 824 (2009).

[154] A. Lugstein, M. Steinmair, Y. J. Hyun, G. Hauer, P. Pongratz, and E. Bertagnolli, Nano Lett., 8, 2310 (2008).

[155] Y.-J. Hyun, A. Lugstein, M. Steinmair, E. Bertagnolli, and P. Pongratz, Nanotechnology, 20, 125606 (2009).

[156] Y. Ding and Z. L. Wang, J. Phys. Chem. B, 108, 12280 (2004).

[157] P. Madras, E. Dailey, and J. Drucker, Nano Lett., 9, 3826 (2009).

[158] E. I. Givargizov, J. Cryst. Growth, 20, 217 (1973).

[159] V. A. Nebol'sin, A. A. Shchetinin, A. N. Korneeva, A. I. Dunaev, A. A. Dolgachev, T. I. Sushko, and A. F. Tatarenkov, Inorg. Mater., 42, 339 (2006).

[160] J. B. Hannon, S. Kodambaka, F. M. Ross, and R. M. Tromp, Nature, 440, 69 (2006).

[161] F. M. Ross, J. Tersoff, and M. C. Reuter, Phys. Rev. Lett., 95, 146104 (2005).

[162] M. L. Hitchman, and K. Fr. Jensen, Chemical Vapour Deposition: Principle and Application, London: Academic Press (1993).

[163] J. Perrin, Y. Takeda, N. Hirano, Y. Takeuchi and A. Matsuda, Surf. Sci., 210, 114 (1989).

[164] S. Hu, J. Kim, P. Tarakeshwar, and K. S. Kim, J. Phys. Chem. A, 106, 6817 (2002).

[165] B. Mehta, and M. Tao, J. Electrochem. Soc. 152, G309 (2005).

[166] P. Roca i Cabarrocas, S. Kumar, and B. Drevillon, J. Appl. Phys. 66, 3286 (1989).

[167] C. Y. Meng, B. L. Shih, and S. C. Lee, J. Nanopart. Res. 7, 615 (2005).

[168] M. L. Yu, and B. S. Meyerson, J. Vac. Sci. Technol. A, 2, 446 (1984).

[169] J. Johansson, L. S. Karlsson, C. P. T. Svensson, T. Mårtensson, B. A. Wacaser, K. Deppert, L. Samuelson, and W. Seifert, Nature Mater., 5, 574 (2006).

[170] C. Wiethoff, F. M. Ross, M. Copel, M Horn-von Hoegen, and F.-J. Meyer zu Heringdorf, Nano Lett., 8, 3065 (2008).

[171] P. Caroff, K. A. Dick, J. Johansson, M. E. Messing, K. Deppert, and L. Samuelson, Nat. Nanotechnol., 4, 50 (2009).

[172] M. Law, J. Goldberger, and P. Yang, Annu. Rev. Mater. Res., 34, 83 (2004).

[173] J. E. Allen, E. R. Hemesath, D. E. Perea, J. L. Lensch-Falk, Z. Y. Li, F. Yin, M. H. Gass, P. Wang, A. L. Bleloch, R. E. Palmer, and L. L. Lauhon, Nat. Nanotechnol., 3, 168 (2008).

[174] L. Seehofer, S. Huhs, G. Falkenberg, and R. L. Johnson, Surf. Sci., 329, 157 (1995).

[175] J. W. Dickinson, J. C. Moore, and A. A. Baski, Surf. Sci., 561, 193 (2004).

[176] H. Minoda, T. Shimakura, K. Yagi, F.-J. Meyer zu Heringdorf, and M. Horn von Hoegen, Surf. Sci., 432, 69 (1999).

[177] A. Howie, J. Microsc., 17, 11 (1979).

[178] E. D. Williams, and N. C. Bartelt, Ultramicroscopy, 31, 36 (1989).

[179] C. H. Grein, J. Cryst. Growth, 180, 54 (1997).

[180] Y. Yang, and E. D. Williams, Surf. Sci., 215, 102 (1989).

[181] E.-S. Cho, J.-W. Park, H. Hur, N.-H. Kim, J.-Y. Baik, C.-H. Jeon, C.-C. Hwang, K.-S. An, and C.-Y. Park, Jpn. J. Appl. Phys., 43, 1312 (2004).

[182] A. A. Baski, and L. J. Whitman, J. Vac. Sci. Technol. A, 13, 1469 (1995).

[183] W. W. Mullins, Phil. Mag., 6, 1313 (1961).

[184] M. Flytzani-Stephanopoulos, and L. D. Schmidt, Prog. Surf. Sci., 9, 83 (1979).

[185] E. D. Williams, and N. C. Bartelt, Science, 251, 393 (1991).

[186] V. I. Marchenko, and A. Ya. Parshin, Zh. Eksp. Teor. Fiz., 79, 257 (1980) [Sov. Phys. JETP 52, 129 (1980)].

[187] S. Rousset, V. Repain, G. Baudot, H. Ellmer, Y. Garreau, V. Etgens, J. M. Berroir, B. Croset, M. Sotto, P. Zeppenfeld, J. Ferré, J. P. Jamet, C. Chappert, and J. Lecoeur, Mater. Sci. Eng. B, 96, 169 (2002).

[188] V. A. Shchukin, and D. Bimberg, Rev. Mod. Phys.,71, 1125 (1999).

[189] O. L. Alerhand, D. Vanderbilt, R. D. Meade, and J. D. Joannopoulos, Phys. Rev. Lett., 61, 1973 (1988).

[190] J. Stewart, and N. Golderfield, Phys. Rev. A, 46, 6505 (1992).

[191] D. R. França, and A. Blouin, Meas. Sci. Technol., 15, 859 (2004).

[192] J. B. Hannon, N. C. Bartelt, B. S. Swartzentruber, J. C. Hamilton, and G. L. Kellogg, Phys. Rev. Lett., 79, 4226 (1997).

[193] N. C. Bartelt, and R. M. Tromp, Phys. Rev. B, 54, 11731 (1996).

[194] V. Schmidt, S. Senz, and U. Gösele, Phys. Rev. B, 75, 045335 (2007).

[195] K. Kim, W. R. L. Lambrecht, and B. Segall, Phys. Rev. B, 53, 16310 (1996).

[196] M. Ueno, M. Yoshida, O. Shimomura, and K. Takemura, Phys. Rev. B, 49, 14 (1994).

[197] Q. Xia, H. Xia, and A. L. Ruoff, Mod. Phys. Lett. B, 8, 345 (1994).

[198] A. Muňoz, and K. Kunc, J. Phys.: Condens. Matter., 5, 6015 (1993).

[199] P. Bhattacharya, T. K. Sharma, S. Singh, A. Ingale, and L. M. Kukreja, J. Cryst. Growth, 236, 5 (2002).

[200] S. Strite, D. Chandrasekhar, D. J. Smith, J. Sariel, H. Chen, N. Teraguchi, and H. Morkoç, J. Cryst. Growth, 127, 204 (1993).

[201] A. P. Lima, A. Tabata, J. R. Leite, S. Kaiser, D. Schikora, B. Schöttker, T. Frey, D. J. As, and K. Lischka, J. Cryst. Growth, 201/202, 396 (1999).

[202] T. V. Shubina, S. V. Ivanov, V. N. Jmerik, D. D. Solnyshkov, V. A. Vekshin, P. S. Kop'ev, A. Vasson, J. Leymarie, A. Kavokin, H. Amano, K. Shimono, A. Kasic, and B. Monemar, Phys. Rev. Lett., 92, 117407 (2004).

[203] K. S. A. Butcher, M. Wintrebert-Fouquet, P. P.-T. Chen, T. L. Tansley, H. Dou, S. K. Shrestha, H. Timmers, M. Kuball, K. E. Pince, and J. E. Bradby, J. Appl. Phys., 95, 6124 (2004).

[204] K. S. A. Butcher, and T. L. Tansley, Superlattices Microstruct., 38, 1 (2005).

[205] K. S. A. Butcher, M. Wintrebert-Fouquet, P. P.-T. Chen, K. E. Prince, H. Timmers, S. K. S. Shrestha, T. V. Shubina, S. V. Ivanov, R. Wuhrer, M. R. Phillips, and B. Monemar, Phys. Stat. Sol. (c), 2, 2263 (2005).

[206] B. R. Natarajan, A. H. Eltoukhy, J. E. Greene, and T. L. Barr, Thin Solid Films, 69, 217 (1980).

[207] C. P. Foley, and J. Lyngdal, J. Vav. Sci. Technol. A, 5, 1708 (1987).

[208] E. Kurimoto, M. Hangyo, H. Harima, M. Yoshimoto, T. Yamaguchi, T. Araki, Y. Nanishi, and K. Kisoda, Appl. Phys. Lett., 84, 212 (2004).

[209] X. Xu, P. Specht, R. Armitage, J. C. Ho, E. R. Weber, and C. Kisielowski, Appl. Phys. Lett., 87, 092102 (2005).

[210] D. Alexandrov, K. Scott, A. Butcher, and M. Wintrebert-Fouquet, J. Vac. Sci.

Technol. A, 22, 854 (2004).

[211] S.-Y. Kwon, Z. Ren, Q. Sun, J. Han, Y.-W. Kim, E, Yoon, B. H. Kong, H. K. Cho, I.-J. Kim, and H. Cheong, Appl. Phys. Lett., 91, 234102 (2007).

[212] D. González, J. G. Lozano, M. Herrera, N. D. Browning, S. Ruffenach, O. Briot, and R. García, J. Appl. Phys., 105, 013527 (2009).

[213] K. Osamura, S. Naka, and Y. Murakami, J. Appl. Phys., 46, 3432 (1975).

[214] N. Puychevrier, and M. Menoret, Thin Solid Films, 36, 141 (1976).

[215] T. L. Tansley, and C. P. Foley, J. Appl. Phys., 59, 3241 (1986).

[216] T. Araki, Y. Saito, T. Yamaguchi, M. Kurouchi, Y. Nanishi, and H. Naoi, J. Vac. Sci. Technol. B, 22, 2139 (2004).

[217] V. Yu. Davydov, A. A. Klochikhin, R. P. Seisyan, V. V. Emtsev, S. V. Ivanov, F. Bechstedt, J. Furthmüller, H. Harima, A. V. Mudryi, J. Aderhold, O. Semchinova, and J. Graul, Phys. Stat. Sol. (b), 229, R1 (2002).

[218] T. Matsuoka, H. Okamoto, M. Nakao, H. Harima, and E. Kurimoto, Appl. Phys. Lett., 81, 1246 (2002).

[219] A. G. Bhuiyan, A. Hashimoto, and A. Yamamoto, J. Appl. Phys., 94, 2779 (2003).

[220] K. L. Westra, R. P. W. Lawson, and M. J. Brett, J. Vac. Sci. Technol. A, 6, 1730 (1988).

[221] L. E. Brus, J. A. W. Harkless, and F. H. Stillinger, J. Am. Chem. Soc., 118, 4834 (1996).

[222] Y. Q. Wang, R. Smirani, and G. G. Ross, Nano Lett., 4, 2041 (2004).

[223] A. P. Alivisatos, Ber. Bunsenges Phys. Chem., 101, 1573 (1997).

[224] Y.-W. Jun, J.-S. Choi, and J. Cheon, Angew. Chem. Int. Ed. 45, 3414 (2006).

[225] V. F. Puntes, D. Zanchet, C. K. Erdonmez, and A. P. Alivisatos, J. Am. Chem. Soc., 124, 12874 (2002).

[226] X. Peng, L. Manna, W. Yang, J. Wickham, E. Scher, A. Kadavanich, and A. P. Alivisatos, Nature, 404, 59 (2000).

[227] V. F. Puntes, K. M. Krishnan, and A. P. Alivisatos, Science, 291, 2115 (2001).

[228] Z. L. Wang, J. Phys. Chem. B, 104, 1153 (2000).

[229] M. A. El-Sayed, Acc. Chem. Res., 37, 326 (2004).

[230] D. Raghunandan, M. D. Bedre, S. Basavaraja, B. Sawle, S. Y. Manjunath, and A. Venkataraman, Coll. Surf. B: Biointer, 79, 235 (2010).

[231] I. Gunjishima, T. Inoue, and A. Okamoto, Langmuir, 24, 2407 (2008).

[232] B. Daoudi, M. Sehil, A. Boukraa, and H. Abid, Int. J. Nanoelectronics and Materials, 1, 65 (2008).

[233] C.-C. Chen, A. B. Herhold, C. S. Johnson, and A. P. Alivisatos, Science, 276, 398 (1997).

[234] L. Ratke, and P. W. Voorhees, Growth and Coarsening: Ostwald Ripening in Material Processing, Springer, 117~118, (2002).

[235] R. Lee Penn, and J. F. Banfield, Science, 281, 969 (1998).

[236] A. P. Alivisatos, J. Phys. Chem., 100, 13226 (1996).

[237] L. E. Brus, J. Phys. Chem., 90, 2555 (1986).

[238] Y.-N. Xu, and W. Y. Ching, Phys. Rev. B, 48, 4335 (1993).

[239] Y. Kayanuma, Solid State Commun., 59, 405 (1986).

[240] A. Zubrilov, Properties of Advanced Semiconductor Materials GaN, AlN, InN, BN, SiC, SiGe . Eds. Levinshtein M.E., Rumyantsev S.L., Shur M.S., John Wiley & Sons, Inc., New York, 49~66 (2001).

[241] T. R. Ravindran, Akhilesh K. Arora, B. Balamurugan, and B. R. Mehta, Nanostruct. Mater., 11, 603 (1999).

[242] Y. Wang, and N. Herron, J. Phys. Chem., 95, 525 (1991).

[243] Y. Kayanuma, Phys. Rev. B, 38, 9797 (1988).

[244] T. Rajh, J. M. Nedeljkovic, L. X. Chen, O. Poluektov, and M. C. Thurnauer, J. Phys. Chem. B, 103, 3515 (1999).

[245] P. Dirac, Principles of Quantum Mechanics (4th ed.), Oxford at the Clarendon Press (1958).

[246] Y. J. van der Meulen, J. Electrochem. Soc., 119, 530 (1972).

[247] B. O. Dabbousi, J. Rodriguez-Viejo, F. V. Mikulec, J. R. Heine, H. Mattoussi, R. Ober, K. Fr. Jensen, and M. G. Bawendi, J. Phys. Chem. B, 101, 9463 (1997).